UiT The Arctic University of Norway

Faculty of Science and Technology

Department of Physics and Technology

Wind resource assessment and siting for the expansion of Fakken wind park

Martine Bjugg

EOM-3901 Master thesis in Energy, Climate and Environment 30 SP, June 2023

Abstract

Norway is anticipated to experience an energy deficit in the coming years, and one solution to address this issue is the implementation of new renewable energy sources. To mitigate the projected energy deficit, increased energy production is required. With its considerable wind potential, the country offers ample opportunities for wind energy development. Consequently, there is a growing demand for accurate methods to identify suitable areas for establishing new wind farms.

The study examines the wind conditions at Vannøya in Northern Norway and evaluates the performance of WRF and WAsP models in accurately estimating wind conditions and energy production at the existing Fakken 1 wind park.

The study found that the WRF model's resolution was insufficient to capture terrain features that influence the wind conditions, and the model tended to underestimate the high wind speeds. Initially, the WRF model provided the closest estimation to the observed production at Fakken 1, with a 9% deviation on average. However, when considering the production losses that the models cannot capture, the WAsP model provided more accurate production estimates and better captured the variations in production within the wind park.

For the proposed expansion, Fakken 2, the WAsP models estimated a yearly production of 173 GWh, while the WRF model estimated a production of 155 GWh. Additionally, the study proposed improvements in turbine positions for Fakken 2, with the potential for increased production.

The WAsP model features and computational speed made it more suitable for wind resource assessment. LiDAR proved valuable in preliminary evaluations but unreliable as a sole measurement tool.

Overall, the WAsP model was deemed more reliable and efficient for wind resource assessment and siting for the Fakken wind power plant.

Acknowledgment

First of all, thank you to my supervisor Yngve Birkelund, for all the great guidance and discussions throughout this master thesis. Thank you to Troms Kraft for allowing me to write this thesis and for providing me with relevant data. Thank you to the group at the university of Bergen for loaning the LiDARs, and for all the help.

Thank you to all my fellow co-students for making the last five years possibly the best five years of my life, it would not have been the same without you guys. I’m grateful for all the good memories we have together.

And thanks to my family for supporting me, specially thanks to my father for all the help with reading and discussing my thesis.

Table of Contents

1 Introduction

1.1 Background

The energy market is currently facing a challenging situation, primarily driven by factors such as Russia's invasion of Ukraine and high gas and electricity prices. The energy demand continues to rise, further intensified by global warming and the urgent need to transition to renewable energy sources to combat climate change. Agreements like the Paris Agreement have accelerated the shift from traditional oil and gas production as less favorable options for energy production to more renewable options.

In Norway, energy consumption has increased by 14,6% between 1990 and 2020, spanning a period of 30 years. In contrast, energy production has seen a 26,5% increase over the same period (SSB, 2023). The country's annual energy consumption is around 140 TWh, while the average energy production is approximately 155 TWh, resulting in a surplus of 15 TWh (Statnett, 2022). However, projections indicate that consumption is expected to rise to 164 TWh by 2027, primarily driven by factors such as oil and gas usage, battery production, and various industries. Energy production is expected to increase at a slower pace. During this period, Norway's energy consumption is predicted to increase by 24 TWh, while energy production is anticipated to rise by only 6 TWh (Statnett, 2022). This indicates a growing energy deficit and a greater need for energy resources in the future.

Wind energy is emerging as one of the fastest-growing sources of energy worldwide (Statkraft, 16.05.23). The global wind energy potential is estimated to be around$4{,}04 \times 10^{22} J$ per year (Letcher, 2017), roughly 70 times the global energy consumption recorded in 2019 (Ritchie et al., 2020). With efficient wind turbines and good wind resources, wind power has become one of the most environmentally friendly methods of commercial energy production available today.

In recent years, the cost of wind power has significantly reduced, making it a more economical option than building new gas or coal power plants in parts of the world. Technological advancements have led to more efficient and robust wind turbines that generate higher power output, require less maintenance, and have longer lifespans (Statkraft, 16.05.23).

Several studies have concluded that wind energy is the energy source with the lowest life cycle pollution, meaning it produces the least amount of CO_2 emissions during the lifetime of a power plant (Asdrubali et al., 2015; Guezuraga et al., 2012) when compared to other energy sources. Additionally, wind energy has the second shortest energy payback time among all the available energy sources, second only to hydropower (Guezuraga et al., 2012).

Norway has substantial wind power potential, as some of Europe's highest average wind speeds are found here. Along the coastal areas, the average wind speed is estimated to be around 7 – 9 m/s, while inland regions experience an average wind speed of about 3 – 5 m/s (Byrkjedal & Åkervik, 2009).

Norway’s abundant wind resources offer an excellent opportunity to harness clean energy. However, Norway's complex terrain of hills and mountains presents challenges when identifying suitable locations for wind parks and accurately assessing their potential. In addition, the increased difficulties of predicting wind power production in such complex terrain may further complicate the integration of wind power into the existing power grid.

1.2 Former research

Multiple studies have been done on the wind flow in complex terrain (Jackson et al., 2013; Markowski & Richardson, 2011) and the wind flows over Fakken wind park. Solbakken et al. (2021) investigated the surface winds over Fakken using WRF. The paper found that the surrounding terrain plays a prominent role in influencing the wind resources at the wind park. The influence of the coastal orthography was found to create complex flow patterns in the area under specific stability and wind conditions. (Solbakken et al., 2021).

A method that has proven to give a good first approximation of the wind energy resource is Numerical Weather Prediction (NWP) (Wallace & Hobbs, 2006b). An NWP model is a computer program that solves the equations describing the atmospheric processes and how the atmosphere changes with time.

The model divides the atmosphere into square areas, with a grid point at each square's center. At each grid point, the model solves the equations for the weather parameters associated with each atmospheric variable, and the value from the model is the average value of the square. With higher-resolution models, the grid points are spaced closer, which results in greater accuracy. However, these models require more powerful and faster computers to run (Wallace & Hobbs, 2006b).

The availability of high-resolution terrain datasets limits the terrain representation in the NWP model. When these datasets are coarse, they cannot provide finer terrain details for high-resolution models. Additionally, due to grid point averaging, the elevations of the highest mountain peaks can be underestimated, and fjords often need to be represented or are represented with less elevation difference. Resulting in certain phenomena due to topography, like convection and downslope wind, will only partially capture by the model (Wallace & Hobbs, 2006b). In previous studies, it has been found that higher resolution gives better results in complex terrain (Carvalho, Rocha, & Gómez-Gesteira, 2012; Carvalho, Rocha, Gómez-Gesteira, et al., 2012; Fernández-González et al., 2018; Samuelsen, 2007; Solbakken et al., 2021; Valkonen et al., 2020). However, compared to reel measurements, NWP models offer some advantages such as low cost, high horizontal and vertical resolution over a large area, and the ability to provide long-term data time series quickly (Wallace & Hobbs, 2006b).

Despite its advantages, the NWP model has certain drawbacks. The models serve only as an approximation of the actual state of the atmosphere. The magnitude of the deviation between the simulated atmosphere and the actual atmosphere varies depending on the model setup, including the selection of parametrization schemes for unresolved physical processes, the representation of terrain and vegetation, the configuration of the model's domain size, location, and spatial resolution, numerical options and initial and boundary conditions (Awan et al., 2011; Solbakken et al., 2021; Wallace & Hobbs, 2006b).

The weather research and forecasting (WRF) model is an NWP model. Several studies have evaluated the performance of WRF with a particular focus on the model's ability to reproduce the wind speed (Draxl et al., 2014; El-Samra et al., 2018; Giannaros et al., 2017; Jiménez & Dudhia, 2013). It is found that the WRF model tends to overestimate the low wind speed and underestimate the high wind speeds. The WRF model is reported to have a good agreement between model simulations and wind speed measurements for areas characterized by complex terrain (Carvalho et al., 2014; Fernández-González et al., 2018).

The Wind Atlas Analysis and Application Program (WAsP) model is a linearized flow model. It's well-known and has been extensively used within the wind energy sector for site assessment in the past 30 years. The WAsP model is the most commonly used for micro-scale flow in wind resource analysis (Berge et al., 2006). Due to the WAsP model being simple and computationally efficient, it can be applied to large areas (Dörenkämper et al., 2020). Numerous studies have shown that the accuracy of wind predictions is influenced by the ruggedness of the terrain and the quality of the topographical input data (A.J. Bowen, 1996; Mortensen & Petersen, 1997; Mortensen, 2006). It was found that WAsP can produce accurate results outside its operating limits. However, this is contingent upon the reference site and the predicted site having small ruggedness indices differences and that the topographical input data are adequate and reliable (Mortensen & Petersen, 1997).

Bilal et al. (2016) investigated using the WRF model coupled with the microscale computational fluid dynamics-based model WindSim. The research indicated that the coupling of these two models did not yield a significant improvement compared to the standalone use WRF model over the complex terrain (Bilal et al., 2016).

In their study, Carvalho et al. (2013) investigated using both WRF and WAsP for wind resource evaluation. The research indicated that using WRF as input in WAsP gave favorable results, with results closely aligned with the measured values at the site. It found that the use of mesoscale output in microscale models could be considered as a valid alternative to in-situ data mainly for preliminary wind resource assessments, although the application of mesoscale and microscale coupling in areas with complex topography should be made with extreme caution (Carvalho et al., 2013).

Wind measurements using LiDAR wind profilers are becoming increasingly common in wind turbine site assessments. LiDAR's special features, such as low spatial resolution in the line of sight (LoS) direction and the measurement of the LoS component of the wind vector, differentiate them. However, despite these differences, LiDAR-measured wind speed agrees well with standard anemometry (Schneemann et al., 2014).

1.3 The aim of this study

Fakken wind park, located north in Troms, is an important green, renewable energy source. With its 18 turbines, it currently produces approximately 139 GWh of electricity annually, which is enough to power about 7500 households (*Fakken vindkraftverk*, 20.05.23). Given the increasing energy demand, there are plans for an expansion of the wind park named Fakken 2. The proposed expansion will be situated northwest of the current park with 11 new and larger turbines. This expansion aims to increase energy production and alleviate the anticipated energy deficit. However, due to the complex terrain in the area, assessing the wind resources is challenging.

This thesis's primary objective is to comprehensively assess the wind resources at the new site. Central to this assessment is the evaluation of different models employed for estimating wind resources, focusing on their accuracy and potential for improvement. Additionally, the thesis aims to evaluate an alternative method that can provide valuable insights into the site conditions without the need for measurement mast, thus saving time and costs. By identifying and utilizing an effective evaluation approach, wind resource assessment becomes more efficient. This information is crucial for power companies to determine whether investing in specific areas is viable and to estimate the expected energy production. It is particularly valuable in complex terrain, where mapping wind resources is inherently difficult. Finding a suitable model for such areas is important to ensure accurate assessments and facilitate informed decision-making.

In summary, this thesis seeks to assess wind resources at the new site and evaluate the performance of different models used for estimation.

1.4 Structure of the study

This thesis is divided into the following chapters.

Chapter 2 – Theoretical background about this thesis. This chapter gives the necessary information on the theory related to modeling in complex terrain. It provides information about wind, wind resource assessment, and energy production estimates. Parts of this chapter are copied from my project paper written in 2022.

Chapter 3 – This chapter contains the site's location and the methodology. It describes how the wind resource assessment and energy production were performed. It gives a description of the models used in the study and how they were used. Parts of this chapter are copied from my project paper written in 2022.

Chapter 4 – This chapter gives the results from the wind assessment done by the models and discusses the different results.

Chapter 5 – This chapter summarizes the results, gives concluding remarks, and discussion about future work.

2 Theory

2.1 Wind in the atmosphere

The earth is heated up by solar radiation. The incoming solar radiation is highest around the equator and decreases with latitude. This results in an uneven heating of the earth's surface and a difference in surface temperature. The horizontal temperature difference leads to a horizontal pressure difference which creates a force called the *pressure gradient force* that causes the air to move and hence the wind to blow from higher pressure towards lower pressure (Ahrens & Henson, 2019).

The horizontal movement of air is affected by the pressure gradient force, Coriolis force, and friction. The pressure gradient force causes the wind to blow, while the Coriolis force and friction affect the wind's direction. The magnitude of the pressure gradient force is related to the pressure gradient:

$$Pressure\ Gradient = \frac{\Delta p}{d} \tag{1}$$

Where Δp is the difference in pressure and d is the distance. If the air is only affected by the pressure-gradient force, the wind will always blow directly from high atmospheric pressure towards low atmospheric pressure. However, that's not the case, since the moment the air starts to move, its path is affected by the Coriolis force. The Coriolis force describes an apparent force due to the earth's rotation. Due to the Coriolis force the wind is deflected to the right of its intended path in the northern hemisphere and to the left in the southern hemisphere (Ahrens & Henson, 2019; Persson, 1998).

The amount of deflection due to the Coriolis force depends on the rotation of the earth, the speed of the object, and the latitude.

$$Coriolis\ Force = 2m\,\Omega\,V\sin\phi \tag{2}$$

Here m is the object's mass, Ω is the earth's angular speed of the earth, which is constant, V is the object's speed, and ϕ is the latitude. From the equation, it is apparent that the Coriolis force increases when the object's speed increases and when the latitude increases, and object gets closer to the poles. The wind speed in not affected by the Coriolis force only the wind direction, since it acts at perpendicular angles to the wind (Ahrens & Henson, 2019).

The Coriolis force is present in all movement at the Earth's surface, but its magnitude is proportional to the velocity of the motion. Meaning that the impact of the Coriolis force is usually minimal when examining small areas. In our daily lives, the Coriolis force is typically so small compared to other forces, like friction, that it is negligible (Ahrens & Henson, 2019).

At a certain velocity, the wind stops accelerating due to a balance between the pressure gradient force and the Coriolis force. As a result, the wind flows in a straight path, parallel to the isobars, while maintaining a constant speed. This type of flow is called geostrophic wind (Jeffreys, 1926). The isobars are, in this case, evenly spaced and straight between a high and low pressure. However, this is a theoretical situation and rarely happens in the atmosphere. The isobars are rarely straight or evenly spaced, and the wind speed varies as it flows along. So, the geostrophic wind is only an approximation of actual wind, but the approximation is close enough to help understand the behavior of the wind aloft (Ahrens & Henson, 2019).

Near the Earth's surface, within the boundary layer, friction plays a role in affecting the movement of the air. The strength of the friction force depends on the roughness and properties of the surface, which causes a decrease in wind speed (Ahrens & Henson, 2019).

Atmospheric stability

Atmospheric stability can be described as a state of equilibrium where air masses in an unstable state favors movement both upward and downward. In contrast, air masses in stable states resists such motion. Analyzing the lapse rate can determine if the atmosphere is stable or unstable. Lapse rate refers to the rate at which the air temperature changes as the altitude increases (Ahrens & Henson, 2019).

Moist adiabatic rate is the temperature change rate in a saturated air parcel as it rises or descends. When the lapse rate is less than the moist adiabatic rate, the atmosphere is considered stable. The moist adiabatic rate can vary regarding cooling or warming, but a common value is 6°C per 1000 meter (Ahrens & Henson, 2019). The dry adiabatic lapse rate is the rate of change in temperature following an air parcel of dry air that's being ascended or descended adiabatically in the atmosphere (Wallace & Hobbs, 2006a). The atmosphere is considered unstable when the lapse rate is greater than the dry adiabatic rate. The dry adiabatic cooling or warming rate is constant and is about 10°C per 1000 meter (Ahrens & Henson, 2019). Conditional instability occurs when the lapse rate is between the moist adiabatic rate and the dry adiabatic rate. The atmosphere is ordinary in a state of conditional instability (Ahrens & Henson, 2019).

The level of instability depends on the magnitude of the difference between the lapse rate of the air mass and the surrounding environment. Unstable conditions result in strong vertical mixing, which causes turbulence and a slight variation in the wind speed with altitude (Bilal, 2016; Gasch & Twele, 2012).

Atmospheric motions

The air's movement can be described by three main components: the vertical component (w), the zonal component (u), and the meridional component (v). The vertical component describes the upward and downward motion of the atmosphere, the zonal component describes fluid flow patterns from west to east along the latitudinal lines, and the meridional component describes fluid movement from south to north along the longitudinal lines (Wallace & Hobbs, 2006b).

The horizontal wind speed, **V**, of the air movement, can be described using the zonal and the meridional components:

$$\boldsymbol{V} = u\boldsymbol{i} + v\boldsymbol{j} \tag{3}$$

Where **i** and **j** are unit vectors. The zonal and the meridional components can be used to calculate the horizontal velocity and the wind direction. The horizontal wind speed can be described by:

$$V = |\boldsymbol{V}| = \sqrt{u^2 + v^2} \tag{4}$$

The wind direction can be described by:

$$\angle V = \left(arctan2(u, v) * \frac{45}{\arctan(1)} \right) + 180 \tag{5}$$

The output is in degrees, where north is defined as 0 degrees and south as 180 degrees.

2.2 Wind phenomena in complex terrain

The wind's direction is influenced by mainly two factors: The rotation of the earth and the topography of the land. As wind passes through valleys and fjords and between mountains and hills, the path is deflected (Ahrens & Henson, 2019). Several types of obstacles can deflect the wind, leading to the emergence of distinct wind phenomena. Locations with flat, elevated terrain, mountains, gaps, and coastal areas are often ideal for harnessing onshore wind power (Letcher, 2017).

The topography in the area around Fakken has the potential to create complex flow patterns, under specific stability and wind circumstances. These patterns may involve phenomena such as gap winds and mountain waves (Solbakken et al., 2021).

Gap winds are a wind phenomenon that occurs in fjords, valleys, or mountain ranges. It happens when wind flows through a gap in the terrain (Ahrens & Henson, 2019). As air passes through a gap in the terrain, it is compressed, and upon emerging on the other side, it expands. Forming a local high pressure at the entrance and a local low pressure at the gap's exit (Scorer, 1952). This pressure difference between the entrance and the gap's exit causes the air to accelerate through it. Resulting in the strongest wind at the exit of the gap. The bigger the pressure difference is the stronger the gap wind (Jackson & Steyn, 1994; Markowski, 2010).

Gap winds are usually strongest in the winter when the cold air is trapped near the surface due to atmospheric stability and a strong inversion layer below the crest of the mountains so that trapped cold air can only escape through the gap. This mostly happens in steep fjords and valleys with a strong elevation gradient (Ahrens & Henson, 2019).

2.3 Wind Energy

Wind energy depends on three factors: The volume of air in consideration, the velocity of the air, and the mass of air (Letcher, 2017). The magnitude of the wind is defined by the velocity of the air in motion, which is related to the amount of energy contained in the wind, i.e., kinetic energy. The kinetic energy through a specific area, A, is determined by:

$$E_k = \frac{1}{2} mV^2 \tag{6}$$

Where V is the horizontal wind velocity, $m = \rho Ax$ is the mass of the air parcel, ρ is the air density, A is the swept area of the turbine blades, and x is the thickness of the air parcel (Letcher, 2017).

Power in the wind

The term "wind power" refers to the rate at which kinetic energy flows. More specifically, it represents the amount of kinetic energy flowing through an area of interest per unit of time (Letcher, 2017). Wind power can be expressed mathematically by finding the derivative of the kinetic energy with respect to time.

By substituting for the mass and taking the derivative we can obtain the equation for wind power:

$$P_w = \frac{dE_k}{dt} = \frac{1}{2} A\rho V^2 \frac{dx}{dt} \tag{7}$$

$$P_w = \frac{1}{2} \rho AV^3 \tag{8}$$

Equation (8) shows a nonlinear relationship between wind speed and wind power. A doubling in the windspeed results in an eightfold increase in wind power. Therefore, wind speed is the primary factor to consider when evaluating wind energy.

Normally wind power is divided by the area of interest; we then obtain the kinetic energy flux, known as the wind power density (WPD). The wind energy flux is wind energy flow rate per unit area and is given by:

$$WPD = \frac{P_w}{A} = \frac{1}{2} \rho V^3 \tag{9}$$

Wind power density is used to compare resources independent of wind turbine size.

Power from wind turbines

Humans have been utilizing the power in the wind since around 4000 BC when the first sailing boats were used for navigation on rivers and lakes. Since then, there have been several large advancements within the technologies, but the fundamental principle remains the same. To capture wind energy in its current modern sense, it is necessary to convert it into electrical energy (Letcher, 2017). A wind turbine converts the kinetic energy in the wind into mechanical energy, which turns the generator that produces electricity. Wind turbines can be utilized both onshore and offshore. Although wind turbines are available in a broad range of sizes nowadays, they are made up of several main components, including rotor blades, nacelle, and tower (Andrews & Jelley, 2017).

Using wind turbines to extract wind energy is based on the same principle that gives airplane wings lift. One way to describe this, is to consider the creation of low pressure on the upper side of the blade that causes the rotor to turn. This is known as the lift. The force of this lift is much stronger than the force of the wind against the front side of the blade, which is called the drag. It is a combination of the lift and drag that causes the rotor to turn. This makes the generator turn and electricity is made (Letcher, 2017). The power generated is proportional to the area swept out by the blades making the power a function of the square of blade length so the bigger the blade the more power can be extracted. Hence we want to make the turbines larger (Letcher, 2017).

A wind turbine extracts energy by reducing the speed of passing winds. If a turbine were to be 100% efficient, all wind would have to stop completely after contact with the turbine. This means that not all the power in the wind can be captured and converted into electric power. The fraction of the power in the wind that can be captured by the turbine is referred to as the power coefficient, C_p (Letcher, 2017). The power coefficient is the ratio of power extracted by the turbine to the total power of the wind, given by:

$$C_p = \frac{P_t}{P_w} \tag{10}$$

Where P_t is the power of the turbine. This can be rewritten as:

$$P_t = \frac{1}{2}\rho A V^3\, C_p = P_w C_p \tag{11}$$

The power production is affected by the turbine variables, the swept area, the capacity coefficient, and atmospheric variables. The theoretical upper limit in the maximum possible power coefficient is $C_p = \frac{16}{27}$, approximately 59% (Huleihil & Mazor, 2012). In practice, however, the power coefficient will always be lower due to aerodynamic and mechanical losses that are neglected in the theoretical calculations describing the Betz limit (Letcher, 2017).

Power curve

A power curve is a mathematical function which describes the relationship between the wind speed and the power output of a wind turbine. The curve shows the non-linear relationship and demonstrates how the power output varies with the wind speed. The cut-in speed, which is the minimum wind speed required for the turbine to generate electricity, is the starting point of the curve. As the wind speed increases, the power output also increases, reaching a maximum value, which is the rated power. Rated power is achieved at the maximum allowable rotor speed. When the rated power is achieved, a brake is used to slow down the rotor and bringing the rotor to a stop to prevent damage to the turbines. This cut-out wind speed marks the end of the curve. Overall, the power curve is a important component in wind energy assessment and is used to estimate the energy production of a wind turbine over a range of wind speeds.

The Vestas V90 3MW turbine is currently in use at Fakken wind park, and its power curve is illustrated in Figure 1. This turbine has a cut-in speed of 4 m/s, a rated power of 3MW, which is achieved at a wind speed of 16 m/s, and a cut-off wind speed of 25 m/s.

In the new area, Fakken 2, the Vestas V150 6MW turbine will be utilized. This turbine has a cut-in speed of 4 m/s, a rated power of 6 MW, and a cut-off speed of 25 m/s.

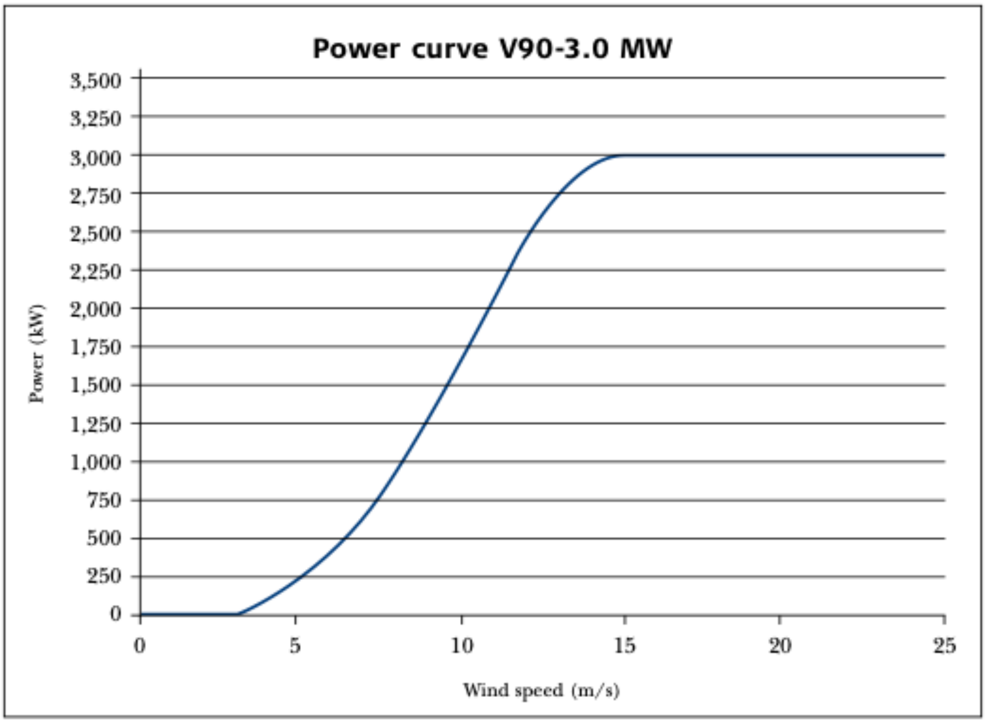

Figure 1: Power curve for the Vestas V90 3 MW turbine (Vestas, 26.05.23).

The figure shows the performance of a wind turbine. It shows how the turbine doesn’t generate any power before the cut-in wind speed, and it also shows the cut-off wind speed, at which the turbine is brought to a stop to avoid damage. The power curve estimates the expected power output for a particular wind turbine at a given wind speed and is an important step for wind energy analysis.

Wind Park

In an ideal case the power output from a wind turbine would be equal to the power curve using the wind speed in the area (Barthelmie & Jensen, 2010). However, that's not the case. Several factors reduce the theoretical power output from a wind park, such as wake losses, icing, maintenance downtime, repair downtime and others (*Capacity Factor of Wind Turbine: What Influences Electricity Generation & What You Should Know About It*, n.d.). When evaluating estimated power production from a model, these must be considered. The power output from a wind park is usually estimated to be 10 – 20% below the theoretical estimated power production (Letcher, 2017).

Wake loss

Wake losses in wind parks is a well-known phenomenon. However, it is still challenging to predict power losses because of variable wind speed, direction, turbulence, and atmospheric stability (Barthelmie & Jensen, 2010).

The wake effect will influence the power production in wind parks where the turbines are arranged in several rows. When the wind hits the turbine kinetic energy is extracted, resulting in less energy in the wind behind the turbine. The wind speed is reduced, and the freestream of the air interrupted. The wake will spread out, and the freestream is gradually restored. If the next row of turbines is closed the wind will not have recovered yet and will influence the power output at that turbine. The wake effects the wind speed, as well as the turbulence. Increased turbulence can lead to an increase in dynamic mechanical load on the turbines and reduce the power output (González-Longatt et al., 2012).

In a wind farm it is inevitable to lose power output due to turbine wakes. Within a wind park where the turbines are often closely spaced, wind speed do not recover to its freestream value after encountering the first row of turbines. Thus, subsequent wind turbines will experience lower wind speed due to the loss of kinetic energy extracted (Barthelmie & Jensen, 2010).

Icing

One of the difficulties of establishing a wind park in northern Norway is icing on the turbines. Ice can accumulate in rotor blades during icing events, resulting in a reduction in aerodynamic efficiency and rotation of the turbine, leading to power losses. During a light icing event the ice can accumulate enough to surface roughness to reduce the aerodynamic efficiency. However, during a more severe icing event, the rotation of the turbine may drop to zero, resulting in a stop in production. Another thing that can occur is that the turbine stops rotating due to heavy vibrations and an uneven ice cover. These vibrations can result in detachment of big ice chunks, which can intensify and, if not stopped lead to the collapse of a wind turbine. In addition, in some situations, the turbine can expel large chunks of ice, resulting in the turbine having to be shut down to protect the other turbines in the park and nearby residents (Hochart et al., 2008).

Wind rose

A wind rose is a good tool for evaluating wind resources in a wind park or a new area. A wind rose depicts the occurrence of winds within various directional sectors, with each sector featuring color-coded categories that indicate the frequency of different wind speeds for that direction. Wind roses are created for a specific site and over a time period and typically consists of a circle divided into sectors, usually between 8 – 16 sectors, one for each direction. While there are many variations in the construction of a wind rose, most include information about wind speed ranges, and some may even indicate other meteorological conditions along with wind direction (Varma et al., 2013).

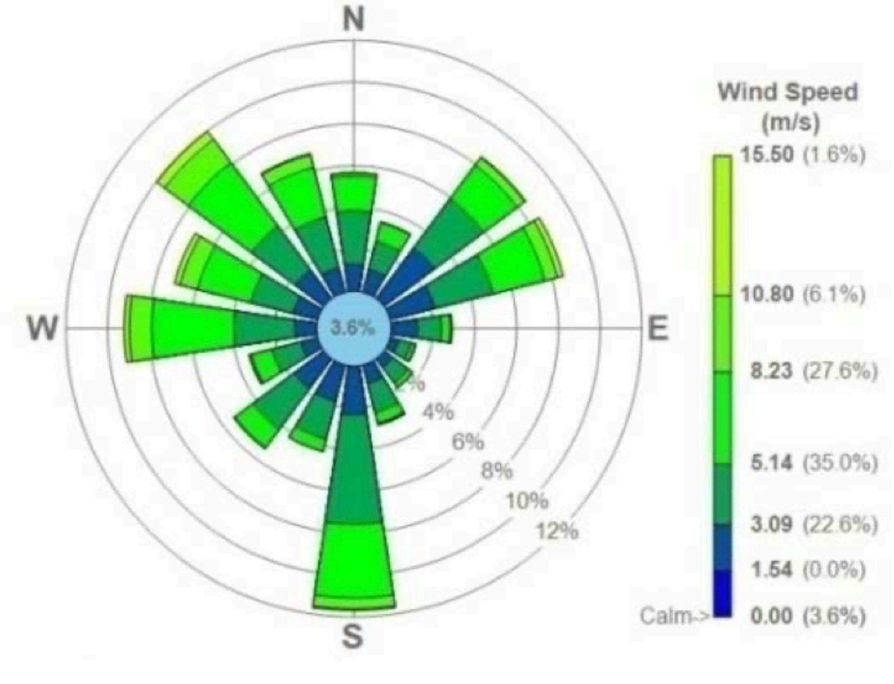

Figure 2: An example of a wind rose (Chavan et al., 2017).

The wind rose serves as a good resource as it indicates the predominant wind direction at a given location. This information is useful in planning the layout of wind turbines in a wind park, as it can help optimize the energy output of wind turbines by determining the best placement and orientation of each turbine. One of the significant factors contributing to power production losses is wake loss. Wind roses can assist in giving an idea of the extent to which wake losses might impact turbine performance. To mitigate substantial wake losses, looking at wind occurrences from all directions and strategically positioning turbines to align with the direction of least wind occurrence is necessary.

In addition, by analyzing the wind direction and wind speed data in the wind rose over a period it can provide information about long-term wind patterns at the selected location, which is essential for accurately predicting the wind power production. Overall, a wind rose can provide vital information for planning and designing a wind park.

2.4 Light Detection and Ranging

Light detection and ranging (LiDAR) is a method of remote sensing which offers the possibility of determining the wind speed and the wind direction at considerable heights using a ground-based instrument (Risan et al., 2018) The fundamental principle of LiDAR technology is based on measuring the Doppler shift of radiation scattered by natural aerosols carried by the wind. The LiDAR sends out a narrow beam of light that reflects off particles and measures the wind speed and wind direction by measuring movement. These particles can be natural aerosols such as dust, water droplets, pollution, pollen or salt crystals (Smith et al., 2006).

The LiDAR instrument has been shown to have significant potential for wind field measurement in the wind energy industry (Smith et al., 2006) but is limited by the spatial averaging along the LiDAR beam (Risan et al., 2018). It is a good instrument to validate a computational flow model in highly complex terrain (Risan et al., 2018). However, one of the main limitations of the LiDAR technology is that a horizontally homogeneous velocity field is assumed when deriving the three-dimensional wind field, which is not a valid assumption in complex terrain. Several studies regarding the performance of LiDARs in complex terrain have been conducted (Gómez et al.; Risan et al., 2018; Vogstad et al., 2013), and one have found that the deviation between ten-minute averaged LiDAR and cup anemometer measurements were significantly larger when the wind direction was such that the complex terrain features were most prominent (Vogstad et al., 2013). They found that the uncertainty for the ten-minute averaged velocities from all LiDARs were in the order of 2,5% when applying the appropriate numerical corrections, which is comparable to the uncertainty of the cup anemometer. (Risan et al., 18; Vogstad et al., 2013)

2.5 Evaluating the models

To evaluate the accuracy of the models compared to the observed values, statistical metrics are used. These metrics show how close the models are to estimating the actual values. These evaluations utilize two time series: the observed values y_i and the simulated values $\hat{y}_i$, where $i = 1, 2, \dots, N$ represents the data points.

The following statistical measuring methods compare the deviation between the models and the observed values.

Root Mean Square Error (RMSE) is a standard statistical method used for model performance and often used in model evaluation studies. The RMSE is a good method to estimate the variance and dispersion between the models and the observed value (Solbakken & Birkelund, 2018). RMSE has the benefit of penalizing large errors more, so can be more appropriate in some cases.

$$RMSE = \sqrt{\frac{1}{N}\sum_{i=1}^{N}(\hat{y}_i - y_i)^2} \qquad (12)$$

Here $\hat{y}_i - y_i$ is the estimation error, and N is the number of observations. The RMSE places greater emphasis on instances with more significant deviation due to the square operation.

Bias gives the deviation between the observation mean and the estimated mean.

$$Bias = \frac{1}{N}\sum_{i=1}^{N}(\hat{y}_i - y_i) \qquad (13)$$

Mean Absolute Error (MAE) is the deviation between corresponding observation and estimation.

$$MAE = \frac{1}{N}\sum_{i=1}^{N}|(\hat{y}_i - y_i)| \qquad (14)$$

Mean Absolute Percentage Error (MAPE) measures how far off the estimates are on average (Khair et al., 2017).

$$MAPE = \frac{1}{N}\sum_{i=1}^{N}\left|\frac{\hat{y}_i - y_i}{y_i}\right| * 100\% \qquad (15)$$

The RMSE, MAE, and bias expresses the average model estimation error. They range from 0 to infinity, and the RMSE and MAE are indifferent to the direction of the errors (Solbakken & Birkelund, 2018).

3 Method

3.1 Data

The on-site measurement of wind speed and wind direction for the entire year of 2017 with a 10 min temporal resolution are provided by Troms Kraft. The data is collected at a measurement mast on the site at a height of 80 meters above ground level (a.g.l.).

The fifth version of the atmospheric reanalysis dataset from the European Center for Medium-Range Weather Forecasting (ECMWF), called ERA5, is a global climate data set from 1940 to present date. ERA5 is a comprehensive dataset that offers hourly estimates of many atmospheric, land and oceanic variables. With a coverage spanning the entire Earth on a 30 km grid, ERA5 resolves the atmosphere using 137 levels from the surface and up to a height of 80 km. ERA5 also incorporates uncertainty data for all variables at reduced spatial and temporal resolutions. The dataset merges extensive historical observations using advanced modeling and data assimilation techniques to generate global estimates. (Hersbach et al., 2020)

The newest version of the global wind atlas, GWA 3.0, uses a downscaling process to generate microscale wind climate data from large-scale climate data. The large-scale ERA5 data from ECMWF is utilized for the simulation period 2008 – 2017 as input data. The original data, with 30 km resolution, are used to force the WRF mesoscale model with a grid placing of 3 km. The resulting wind climates are generalized through a generalization process on the data to match the spacing of mesoscale data used in their creation, yielding a set of microscale wind climates (*Global Wind Atlas*, 2019).

Following the generalization process, the set of wind climates is applied in the DTU Wind Energy microscale modeling system, covering the entire globe, except the North and South Poles and far offshore ocean areas. The modeling process involves conducting WAsP calculations to estimate local wind climates for every 250m at five different heights: 10m, 50m, 100m, 150m and 200m. On a 250m grid, there is a local wind climate for every node. In addition, the GWA 3.0 has incorporated refined elevation and landcover data in the microscale modeling process, further elevating the accuracy of the results (*Methodology*, 2019).

3.2 Site

The area of interest in this thesis is Fakken wind park located on the eastern side of Vannøya in Karlsøy municipality in the North of Norway. Its Arctic climate and coastal conditions characterize the site. During the winter season, there is a contrast in temperatures between the frigid air over land and the warm air over the ocean due to the North Atlantic Current. This results in a pressure difference from east to west, with higher pressure over the land and lower pressure over the ocean. During the summer season, the temperature and pressure gradients are often inverted, causing the main wind direction to come from the northeast (NE), while the main wind direction during the winter is southeast (SE) (Svendsen & Skjoldal, 1995).

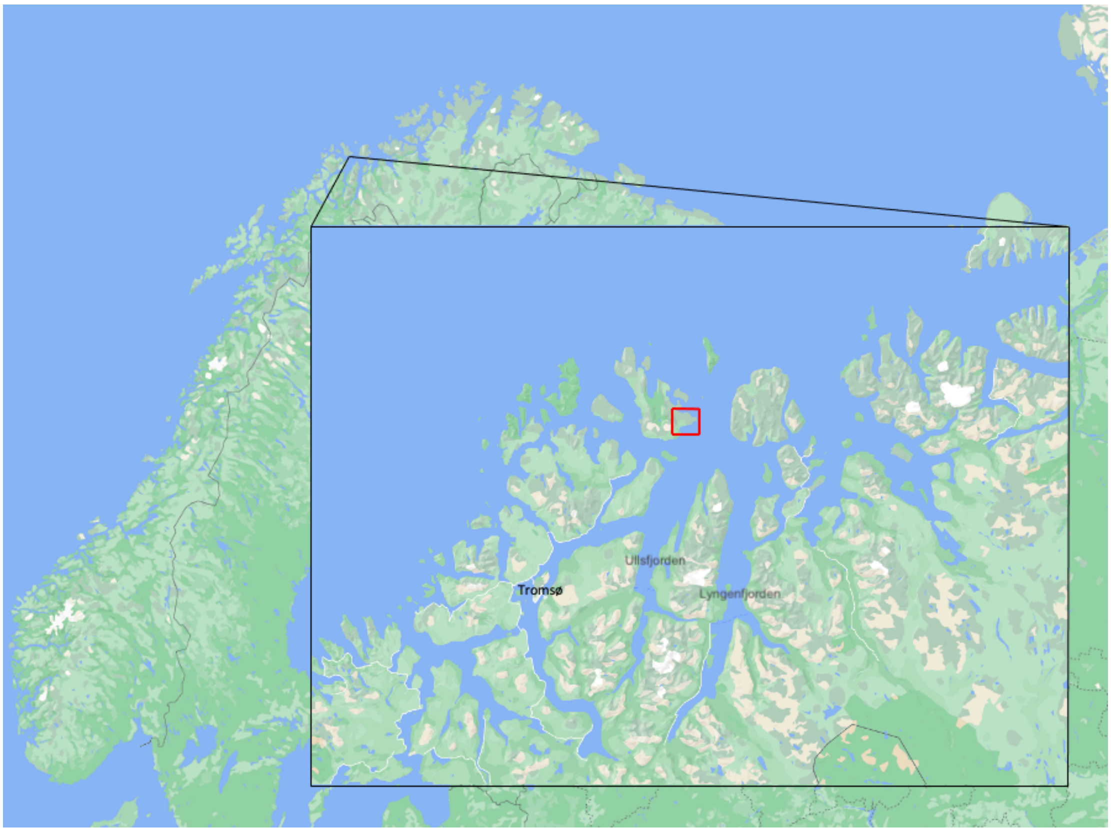

Figure 3: Map over the area, showing the location of the wind park. Fakken is marked with the red square.

Figure 3 displays the surrounding terrain that influences the wind resources at the wind park. The wind park has relatively flat terrain and is located 40 – 200 meters above sea level. The island has diverse topography, with multiple mountain ranges. The island faces the open ocean to the north, while to the south it is encircled by landmasses characterized by large fjords and high mountains. Two large fjords, Ullsfjorden and Lyngenfjorden, are directly south of the island. This complex and diverse terrain surrounding the island has a substantial impact on the area's wind resources, and wind phenomena like gap winds can occur (Solbakken et al., 2021).

Figure 4 shows the terrain height in the area. The figure depicts the various heights in the region, including mountain peaks exceeding 1300 meters on the nearby mainland, shown on the figure as the white areas, while the red areas are areas with an elevation between 500 and 1000 meters. The figure highlights the significant elevation differences on the island and the surrounding area, displaying the complex and varying topography.

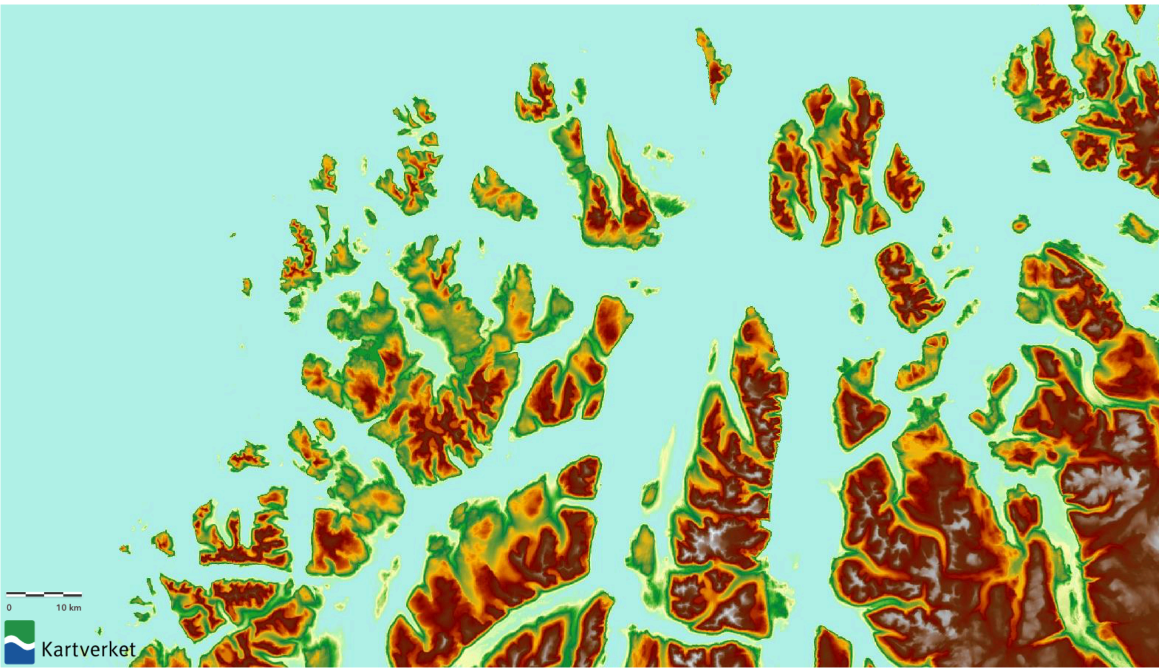

Figure 4: The terrain height around Vannøya

Fakken wind park is a well-established wind park. It has a total capacity of 54 MW, with 18 turbines, each with 3MW rated power and a hub height of 80 meters a.g.l. (*Fakken vindkraftverk*, 20.05.23). They are in two rows as shown in Figure 5. The turbines are numbered from west to east, with the southern row first.

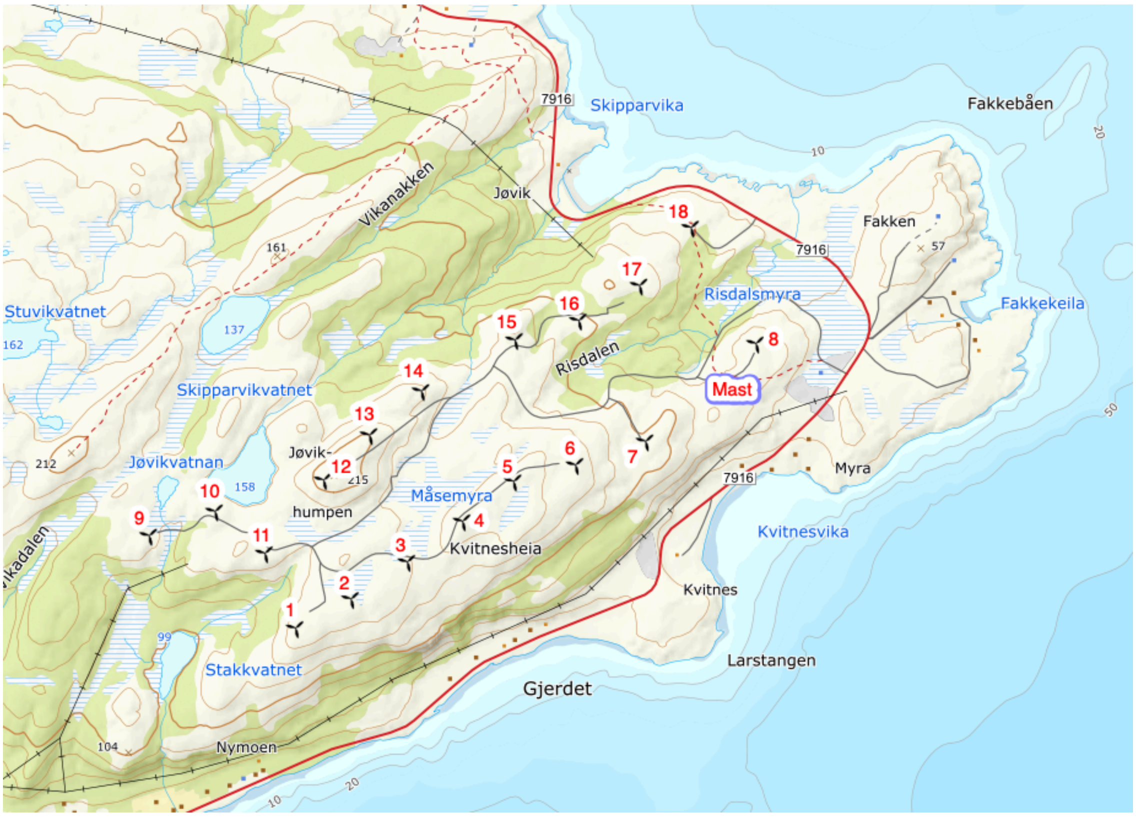

Figure 5: Placement of the 18 turbines in Fakken 1

The new area intended to expand the wind park is located north-west of the existing wind park. The new site has a total capacity of 66 MW, with 11 turbines, each with 6 MW rated power and a hub height of 112 meters a.g.l.

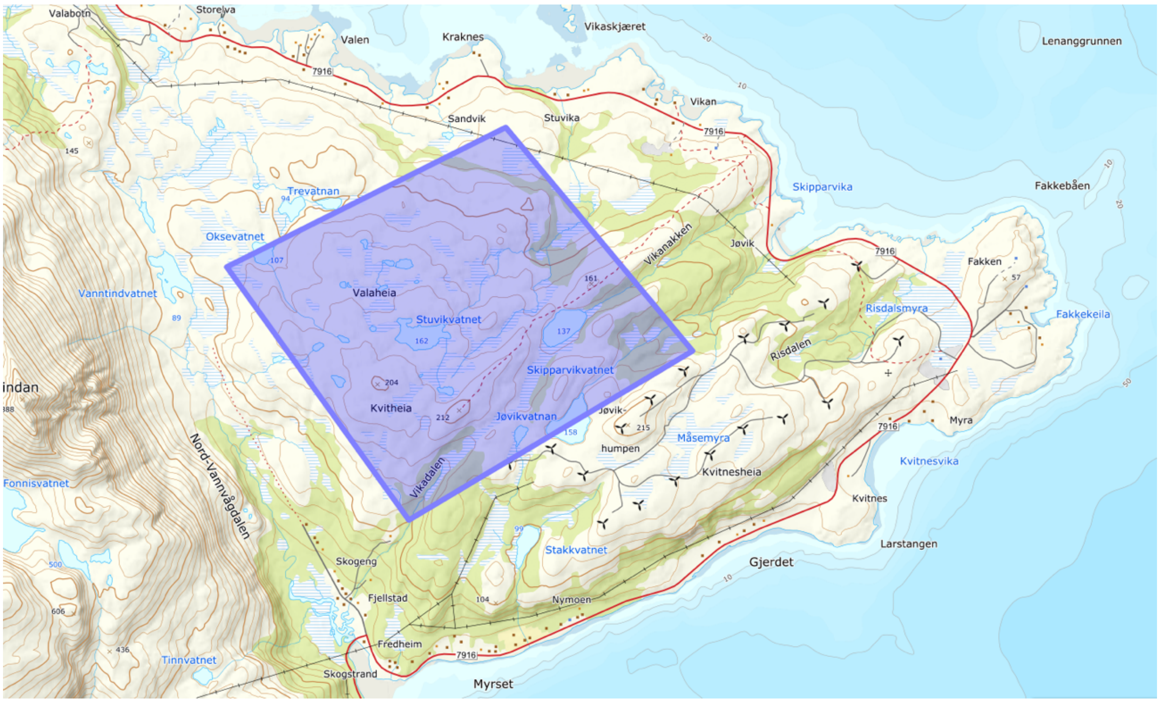

Figure 6: The intended area for Fakken 2

The turbines in Fakken 2 are categorized by letters not numbers, from A – K, and figure 8 shows the preliminary position of the turbines. Their exact location has not yet been determined; this thesis will look at some suggested placements of the turbines. Troms kraft has been suggested where the 11 new turbines should stand.

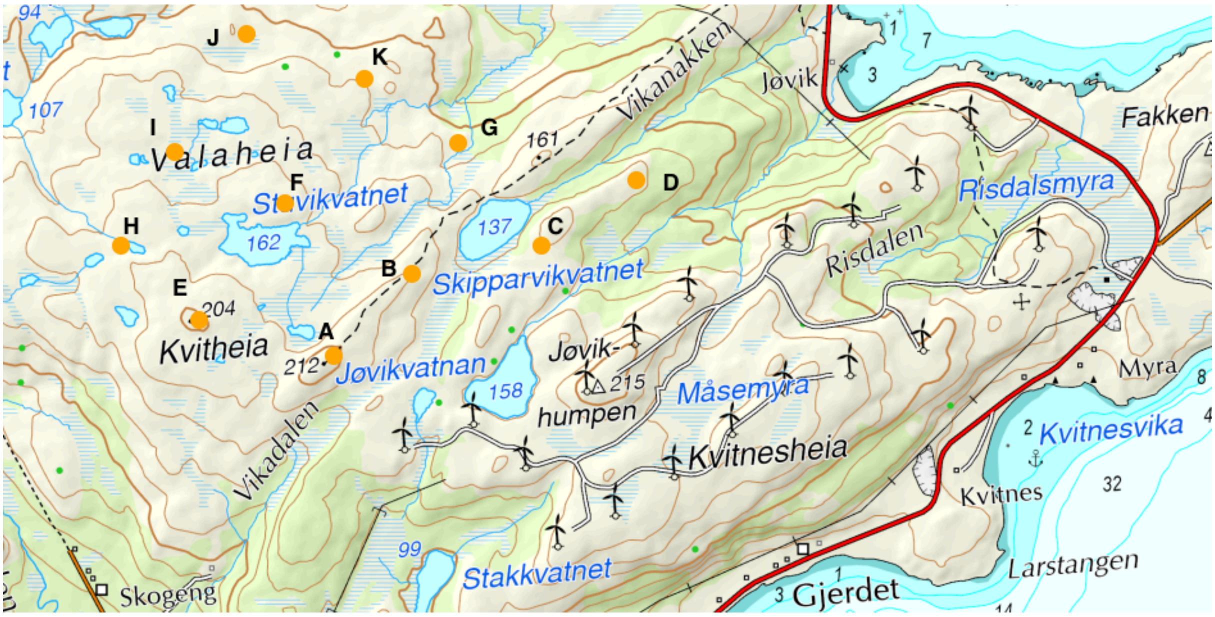

Figure 7: Placement of the new turbines in Fakken 2

3.3 The Weather Research and Forecasting model.

The Weather Research and Forecasting (WRF) model is applied for this thesis. The WRF model is a three-dimensional, nonhydrostatic mesoscale model developed by the National Center for atmospheric Research (NCAR). The model is used to research on atmospheric processes and numerical weather prediction (NWP). Numerical weather prediction models were initially developed for weather forecasting applications but have also emerged as a useful tool for the wind power sector as they can provide users with high resolution wind climatology over large areas (Jacobsen, 2005; Carvalho et al., 2012b; Mughal et al., 2017; Carvalho et al., 2014).

This thesis uses the WRF model to map and assess the wind resources at Fakken wind park. The WRF model allows users to optimize the configuration for a specific area or weather event. This allows the user to fine-tune to accurately simulate wind conditions, which is crucial with wind-related applications to limit how the model deviates from the real atmosphere, as even minor discrepancies in wind speed can significantly impact wind energy estimations (Solbakken et al., 2021). Three WRF models with 1 km horizontal resolution have been simulated over the wind park. The wind resource assessment was based on 2017 and returned hourly output throughout the year.

WRF Preprocessing System

WRF Preprocessing System (WPS) consists of a suite of three programs that collectively prepare input data for real-data simulations in the WRF model. Each program performs specific stages of data preparation; geogrid defines model domains and interpolates static geographic data to the grids; ungrib extracts meteorological fields from GRIB-formatted files; and metgrid horizontally interpolates the meteorological fields extracted by ungrib to the model grids defined by geogrid. Vertical interpolation of meteorological fields to WRF eta levels is performed within the real program (*Users Guide v4.3, Chapter 3*, 25.04.23).

All three WPS programs read parameters from a standard namelist file, called *namelist.wps*, which contains separate namelist records for each program and a shared namelist record defining parameters used by multiple WPS programs.

Geogrid

Geogrid plays a key role in preparing the input data for the WRF model by providing interpolated terrestrial data sets crucial for accurate and reliable simulations (*Users Guide v4.3, Chapter 3*, 25.04.23). As part of WRF Preprocessing System, Geogrid defines simulation domains and interpolates various terrestrial data sets onto the model grids. The simulation domains are determined by user-specified information in the geogrid namelist record of the WPS namelist. The geogrid program performs a multitude of interpolations, including latitude, longitude, and map scale factors at every grid point, as well as default interpolations for soil categories, land use categories, terrain height, annual soil temperature, monthly vegetation fraction, monthly albedo, maximum snow albedo, and slope category to the model grids. To accomplish this, global data sets for each field are provided through the Geographical Static Data Downloads Page. These data sets are time-invariant, and therefore only need to be downloaded once as they remain constant through the simulation.

Ungrib

The ungrib program is responsible for reading the GRIB files, extracting the data, and converting the data to a simple format called intermediate format. The GRIB files usually contain time-varying meteorological fields from another reginal or global model; in this thesis the input data is from ERA5. GRIB files typically contain more fields than what is required for initializing WRF. Both versions of the GRIB format utilize codes to identify the variables and levels within the GRIB file, making it necessary for ungrib to extract and convert only the relevant data into the intermediate format (*Users Guide v4.3, Chapter 3*, 25.04.23).

Metgrid

The metgrid program horizontally interpolates the meteorological data in the intermediate format, which is extracted in the ungrib program, onto the simulation domain defined by the geogrid program.

The interpolated output data from the metgrid program is then used as input by the WRF real program. The specific range of dates to be interpolated by metgrid is defined in the “share” namelist record of the WPS namelist file, and these dates must be specified individually for each simulation domain. Since the work of the metgrid program, like the ungrib program, is time-independent, the metgrid needs to be run every time a new simulation is initialized. To provide control over the interpolation of each meteorological field, the METGRID.TBL file is utilized. The METGRID.TBL file provides one section for each field, allowing for the specification of assorted options such as the interpolation methods, masking field for masked interpolations, and the grid staggering to which a field is interpolated. This enables customization, fine-tuning, and the interpolation process to specific requirements and preferences (*Users Guide v4.3, Chapter 3*, 25.04.23).

The Advanced Research WRF model

The Advanced Research WRF (ARW) model is a comprehensive numerical model that is fully compressible and nonhydrostatic, although it can run in hydrostatic mode during run-time. Its vertical coordinate can be chosen as either a terrain-following (TF) or hybrid vertical coordinate (HVC) based on hydrostatic pressure. The model employs Runge-Kutta 2nd and 3rd-order time integration methods, as well as 2nd to 6th order advection schemes in both horizontal and vertical directions. The grid is staggering follows the Arakawa C-grid configuration. For acoustic and gravity-wave modes, a time-split small-step approach is utilized. Furthermore, the model dynamics ensures conservation of scalar variables (*Users Guide v4.3, Chapter 5*, 20.04.23).

Topography, land-water distribution, and land use data have been interpolated onto the model grid to characterize the terrestrial landscapes. The data is based on the 20-category Moderate Resolution Imaging Spectroradiometer (MODIS) land use data and the Global Multi-resolution Terrain Elevation Data 2010 (GMTED 2010), both with a resolution of 30 arc-seconds. The physical processes in the WRF model are configurated with the Thompson microphysics scheme (Thompson et al., 2008), the rapid radiative transfer model for global applications (RRTMG) shortwave and longwave radiation schemes (Mlawer et al., 1997), the Monin – Obukhov (Janjic Eta) similarity scheme (Janjić, 1994; Jiménez et al., 2012), the Noah land surface model scheme (Tewari et al., 2004), the Mellor – Yamada Nakanishi Niino (MYNN) 2.5 level planetary boundary scheme (Nakanishi & Niino, 2009; Olson, 2019), the Tiedtke cumulus scheme(Tiedtke, 1989; Zhang et al., 2011), and the urban canopy model surface scheme (Chen et al., 2011).

The WRF model code contains an initialization program (*real.exe*), a numerical integration program (*wrf.exe*), a program to do one-way nesting for domains run separately (*ndown.exe*), and a program for tropical storm bogus (tc.exe) (*Users Guide v4.3, Chapter 5*, 20.04.23).

Domain

In this thesis, the WRF model is configured to include three one-way nested domains with a parent grid ratio of 1:3. The three domains, D01, D02, and D03 are configurated with a horizontal resolution of respectively, 9 km, 3 km, and 1 km. The vertical structure of all domains consists of 38 terrain-following sigma levels with an upper boundary at 50 hPa. This configuration provides a comprehensive perspective of the overall weather conditions and offers a more refined and detailed analysis of the area surrounding the wind park.

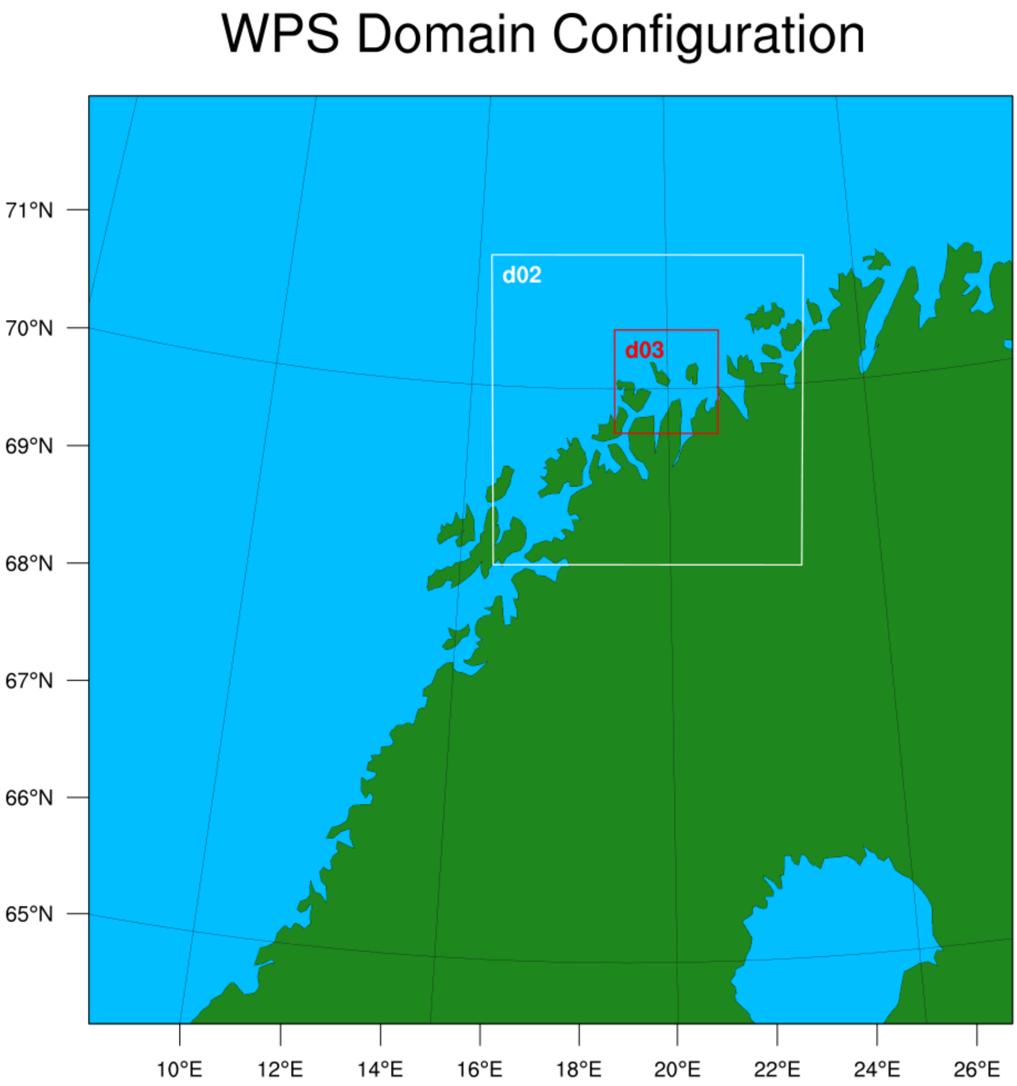

Figure 8: The domain configuration in WRF

The figure above shows the domain configuration, where the Vannøya is in the center of D03. The large mountains in Lyngen and the nearby fjords, like Ullsfjorden and Lyngenfjorden, are also included in the domain since they are expected to have an impact on the local weather system around Fakken wind park.

Wind turbine scheme

In this thesis, three WRF model simulations were conducted over the same area with identical domain configurations. The first simulation is without any wind turbines included, for short denoted WRF Vannøya. The second simulation includes the 18 wind turbines of the current Fakken wind park, designated as Fakken 1. In the third simulation, WRF Fakken 2, the proposed placements of the turbines are included together with the existing. The positions of these turbines were determined based on recommendations from an external company.

To activate the parameterization, the *windfarm_opt* needs to be set to 1 in the physics part of the namelist. The WRF model is then expected to find a file named windturbines.txt, where each file line specifies one turbine, its location, and its turbine type. The location of each turbine is specified using latitude and longitude—the type of turbine points to the file that contains the turbine specifications (Fitch et al., 2012). With the turbine type set to 1, WRF is expected to find the file *wind-turbine-1.tbl*, and when the turbine type is set to 2 WRF expects to find the file wind-turbine-2.tbl. The tables contain the height in meters of the turbine hub, the diameter in meters of the rotor, the standing thrust coefficient, the turbine's nominal power, and the turbine's power curve.

Post processing

The output files generated from the WRF simulation are stored in NetCDF format, which contains different variables and can be accessed by computers that utilize various methods for storing integers, floating-point-numbers, and characters. This data can be analyzed using, for example, NCL, Python, or MATLAB. This thesis employed NCL scripts to merge files, reduce file size, and extract relevant variables. Additionally, Python was utilized for calculating and generating plots and figures. As a part of the extraction process, the relevant variables are interpolated to a height of 80 meters for Fakken 1 and 112 meters for Fakken 2, which is the hub height of the existing turbines on Fakken and the newly intended turbines.

Estimating the wind energy

The estimation process for wind energy production involves several steps. Firstly, the wind speed is extracted at the hub height of the turbines, which is 80 meters (a.g.l.) for the turbines at Fakken 1 and 112 meters a.g.l. for the turbines at Fakken 2, for all turbine locations. This is achieved through vertical interpolation from horizontally interpolated wind data. This results in a unique wind speed series that captures the wind speed variations within the wind park. Next, the wind energy production calculation is carried out in Python, using the same approach for all three simulations. The u and v components are extracted from the WRF file at the hub height, and then equation 3 is employed to calculate the horizontal wind speed. The power curve for the Vestas V90 3MW turbine is applied to the time series for the turbine locations in Fakken 1, and the power curve for the Vestas V150 6 MW turbine is applied to the time series for the turbine locations in Fakken 2. These curves contain power production values for wind speed values at every increase of 1 m/s and ensure an even more accurate value by interpolating the wind speed with the power curve. Finally, the power productions from all the turbines are summarized to obtain the overall power production of the wind park.

3.4 Wind Atlas Analysis and Application Program

The Wind Atlas Analysis and Application Program (WAsP) version 12.7 was utilized for this thesis. WAsP is a comprehensive Windows software designed for predicting wind climates, wind resources and energy yields from turbines and wind parks. The WAsP software is widely used in the wind energy industry. It is utilized for sites all over the world, for all kinds of terrain (Bechmann, 2017), and features several models to describe wind flow over different terrains and near sheltering obstacles. The software conducts vertical and horizontal extrapolation of wind climate statistics (Heathfield et al., 2014).

WAsP was developed on the bases of the Wind Atlas Methodology, which corrects observed wind climate statistics for local effects from orography, roughness, and obstacles to generate standardized wind atlas (Pereira et al., 2010). WAsP employs a linear model of the Navier-Stokes equations and uses simplified equation solutions where nonlinear effects are not considered. Thus, obtaining fast but less precise results for average flows. This can lead to WAsP overestimating the capacity factor and wake loss (Ramos et al., 2017).

The WAsP methodology consists of five main calculation blocks: Analysis of raw wind data, generation of wind atlas data, wind climate estimation, estimation of wind power potential, and calculation of wind farm production (Heathfield et al., 2014).

To gain a comprehensive understanding of the potential production at Fakken, the simulation in WAsP was performed for two scenarios that incorporated different input data. The first scenario considered the 18 existing wind turbines at the wind park, denoted as WAsP Fakken 1. The second scenario included the 18 existing turbines and the 11 new turbines planned for the expansion area, Fakken 2, denoted as WAsP Fakken 2. Two generalized wind climates have been applied to both scenarios to obtain an accurate and realistic picture of the production. This approach was implemented to determine which input data provides the results closest to the actual production.

Input data

The two-input data used for the simulations are the time series from the measurement mast at Fakken for 2017 and the data collected from the Global Wind Atlas.

The WAsP Climate Analyst tool processes the wind data from the measurement mast. The program analyses time series of meteorological data (Heatfield, 2007; Heathfield et al., 2014). The time series from the measurement mast has wind speeds and wind direction data with a 10-minute interval for 2017. The time series is analyzed, and the results are summarized to describe aspects of the climate. These summaries are presented as wind roses and wind speed histograms divided into sectors. To optimize computational efficiency, the wind speed histograms are fitted with Weibull distributions (Pereira et al., 2010).

The GWA3 is already processed, collected from Global Wind, and inputted directly into the WAsP 12 program as a generalized wind climate.

Generating a map

To generate a map that can be used for the simulation, the WAsP Map Editor tool was used. The map editor is a utility tool for inspecting, editing, and creating vector maps for WAsP, and must have a terrain description for wind flow modeling in WAsP (Heathfield et al., 2014; Mortensen et al., 2021). A vector map describes the area's topography surrounding calculation sites such as meteorological stations, reference sites, or turbine sites (Heathfield et al., 2014;

Mortensen et al., 2021). The map for this simulation is created by importing elevation and roughness files from the GWA warehouse database to the WAsP Map Editor and converting them to the WAsP map format.

The maps domain is specified in latitude and longitude, with the location of the map center at the measurement mast at 70.09°N and 20.09°E. The maps extension is selected in the S-N and E-W directions, with a 50 km distance in both directions and with the UTM zone 34 WGS 1984 projection. Once the map is converted from grid to vector format and transformed into the target map, it becomes a vector file that is used as input in WAsP 12 (Mortensen et al., 2021).

The terrain of the area heavily influences the accuracy of the WAsP model. Linear models, like WAsP, assume attached flows and may overestimate flow speeds over rugged terrain. Despite being developed for flat terrain, the model has proven reliable in predicting climatological conditions over slow, smooth hills of small to moderate dimensions with sufficiently gentle slopes that ensure attached flows (Pereira et al., 2010). WAsP has been successfully applied even in complex terrain, although the ruggedness index concept has been implemented to enhance the model resource assessment capabilities in such terrain. Over the past decade, the ruggedness index (RIX) has been widely used in studies, particularly in cases where the terrain exceeds the operational envelope of the WAsP model. The fraction of the surrounding terrain steeper than a specified critical slope decides the RIX for a given site. It serves as a rough indicator of the degree of flow separation and therefore, the extent to which the terrain violates WAsP's requirement for mostly attached flows in gentle and smooth surroundings. In WAsP, ruggedness index calculations are performed for all predictor and predicted sites, and a RIX value of zero or a few percent at most is ideal (Mortensen, 2006).

Generalized wind climate

To create a generalized wind climate, the measured data is transformed to fit a standard Weibull frequency (A.J. Bowen, 1996). The resulting climate is the distribution of wind speeds and directions for the reference site, in this case, the measurement mast, with all local obstacles, surface roughness and orographic effects removed or standardized. This makes the generalized wind climate site independent and can be used to evaluate the wind resources at other sites. The generalized wind climate is then considered universal within a region defined by the extent of the wind regime at the reference site. To estimate the wind speeds and energy at the predicted site, WAsP uses the generalized wind climate from the measured data at the reference site and considers the local obstacles, surface roughness, and orographic effects at the predicted site ((A.J. Bowen, 1996; Mortensen, 2006).

The two different input data are used to generate two generalized wind climates. WAsP then performs inverse calculations, like those used to create the wind climate, using terrain descriptions surrounding the predicted site. This enables the model to predict the expected climate at the predicted site.

Estimating the energy production

To estimate the wind energy potential, WAsP calculates the total energy content of the mean wind. However, turbines must be placed into the terrain before the calculation can be done. In the WAsP Fakken 1 simulation the 18 turbines have a universal hub height of 80 meters a.g.l. In the WAsP Fakken 2 simulation, the turbines at Fakken 2 have a universal hub height of 112 meters a.g.l.

By providing the program with the power curve of the turbines, which includes the power and thrust coefficient, the program can calculate the wake losses for each turbine in the park and estimate the net annual energy production of each turbine and the entire park, which is the gross production minus the wake losses (Mortensen et al., 2021). The specific turbines used on Fakken are the Vestas V90 3 MW and the Vestas V150 6 MW. The power curve for the V90 was included in the WAsP sample data, while the power curve for the V150 was created using the WAsP Turbine Editor tool by doubling the V90 power curve.

The wake model in WAsP uses straightforward parameterization of wake expansion, where the velocity deficit at a given distance depends on the thrust coefficient, turbine rotor diameter, and the wake decay coefficient. The wake decay coefficient (k) describes the rate of wake expansion and is an abstraction of roughness and stability influences on turbulence and wake dissipation. The recommended value for k is 0,075 for land (Barthelmie & Jensen, 2010).

Although the wake model in WAsP tends to under-predict wake losses in the center of the array, this is compensated for by predicting lower than observed efficiencies at the edge of the array, which could be interpreted as a lack of prediction of speed-up effects or an over-prediction of wake losses at the corners and edges of the wind park (Barthelmie & Jensen, 2010).

Resource grid

A resource grid creates a wind resource map over Fakken 1 and Fakken 2. A wind resource grid describes the variation of wind resources across the site. It allows for managing a rectangular set of points for which summary predicted wind climate data are computed. The points are arranged into rows and columns with regular spacing to visualize the areas wind resources or wind climate pattern (*Wind Resource Mapping - WAsP*, 28.04.23).

Each point in the grid resembles a simpler version of a regular turbine site, with all points sharing the same height, a.g.l. If a wind turbine generator is associated with the grid, this specification applies to all points in the grid. For each point WAsP calculates the elevations, mean wind speed, mean power density, the annual energy production, the Weibull-A value, the Weibull-k value, the ruggedness index RIX and the performance indicator ΔRIX (*Wind Resource Mapping - WAsP*, 28.04.23).For this simulation, a resource grid with a hub height of 80 meters a.g.l has been placed over Fakken 1 with the Vestas V90 turbine generator associated with the grid. A resource grid with a hub height of 112 meters a.g.l. has been paced over Fakken 2, with the Vestas V150 wind turbine generator associated with the grid.

3.5 LiDAR

A 2D Windscanner consisting of two scanning pulsed long-range doppler LiDARs Windcube100s (WLS100s) manufactured by the French company Leosphere was used for this thesis. The 2D scanners can steer the laser beams of the systems into the desired direction in integer angle steps. The range of each LiDAR in Line of Sight (LoS) direction in the user configuration is up to three kilometers, depending on the atmospheric conditions.

In this configuration, the LiDARs switch between three different scans for an hour. One vertically, one scanning over the area, and one fixed scan. For this thesis, we are only interested in the fixed scans. The LiDARs do not move while measuring. The LiDARs scanners were pointed in the direction of the position of the new measurement mast. The LiDAR bearing was determined by measuring the distances on maps and calculating the angles manually. The setup for LiDAR 1 and LiDAR 2 are shown in Figure 9 and Figure 10.

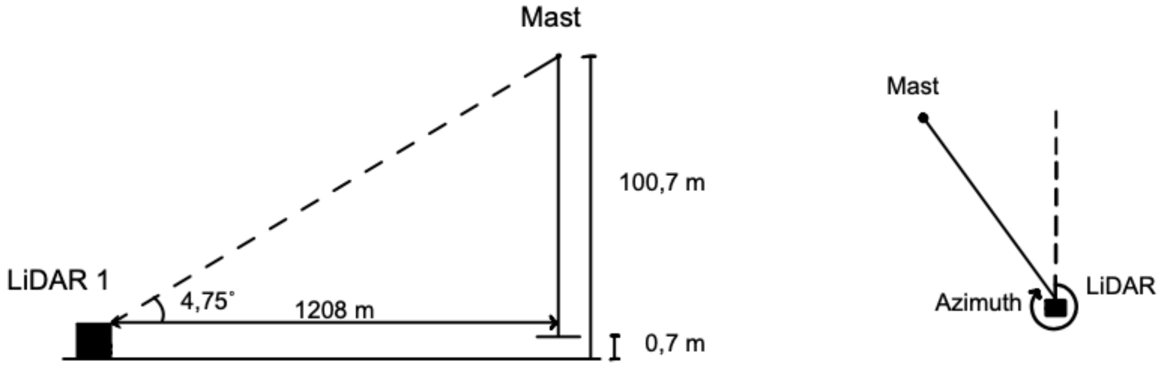

Figure 9: Setup for LiDAR 1

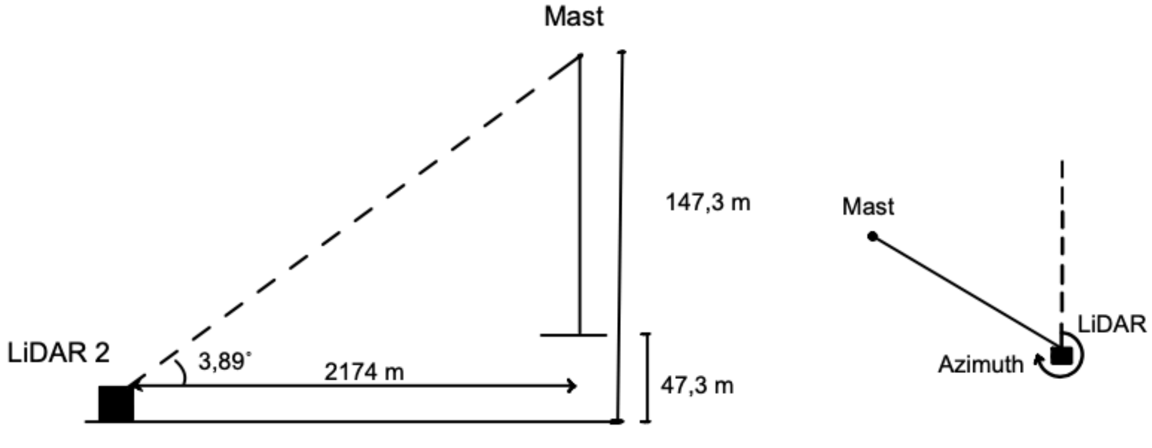

Figure 10: Setup for LiDAR 2

The two LiDARs are placed in the wind park, shown in Figure 11, facing the new area of Fakken 2. LiDAR 1 is near turbine 10, while LiDAR 2 is near turbine 15, and several large wind turbines close by the instruments may affect the LiDARs.

The distance from LiDAR 1 to the mast is 1208 meters, and from LiDAR 2 to the mast, it is 2147 meters. They are located 1520 meters from each other. The instrument was leveled and oriented towards the north using hard targets near the LiDAR; the hard targets used were close by hills since the close by turbines could not be used due to the movement of the blades.

Figure 11: Placement of the two LiDAR and the intended measurement mast.

The measurement started in the middle of December 2022 and lasted until June 2023. The line-of-sight velocities were collected throughout this period. Due to technical problems and changes in the configuration, this work will use data from the 10 February to 27 March. The data is analyzed with focus on average wind speed and direction.

To estimate the horizontal wind speed at the location of the measurement mast the horizontal component, v_h, from each LiDAR is calculated first. The horizontal component is calculated using the scanner's elevation angle, β, and the line-of-sight velocities v_{LoS} collected from the LiDARs at the range of the measurement mast (Schneemann et al., 2014).

$$v_h = \frac{v_{LoS}}{\cos(\beta)} \tag{16}$$

In this calculation, the assumption of no vertical wind speed is used. The vertical component w contributes to the LoS velocity with the sine of the elevation angle. So, for elevation angles of the LiDARs of less than 10 degrees the vertical fluctuations cause low fluctuations in the LoS and so in the calculated horizontal components (Schneemann et al., 2014). The elevation angles in this case are $\beta_1 = 4{,}75°$and $\beta_2 = 3{,}89°$ for LiDAR 1 and LiDAR 2, respectively.

The next step is to calculate the horizontal wind components. The components, u and v, are calculated from the horizontally projected radial speeds of both LiDAR's using the solution of the linear system (Schneemann et al., 2014):

$$\begin{bmatrix} v_{h1} \\ v_{h2} \end{bmatrix} = \begin{bmatrix} \sin(\gamma_1) & \cos(\gamma_1) \\ \sin(\gamma_2) & \cos(\gamma_2) \end{bmatrix} \cdot \begin{bmatrix} u \\ v \end{bmatrix} \tag{17}$$

Yielding

$$u = \frac{v_{h1}\cos(\gamma_2) - v_{h2}\cos(\gamma_1)}{\sin(\gamma_1 - \gamma_2)} \; and \; v = \frac{v_{h2}\sin(\gamma_1) - v_{h1}\sin(\gamma_2)}{\sin(\gamma_1 - \gamma_2)} \tag{18}$$

Here $\gamma_1 = 324°$ and $\gamma_2 = 280°$ are the azimuth angle of LiDAR 1 and LiDAR 2, respectively. The horizontal wind speed and the direction are then calculated using Equation 4 and equation 5, respectively.

4 Results & discussion

4.1 Wind direction

When accessing a wind park, the wind direction plays a crucial role. Wind roses are used to visualize the occurrence of wind from different directions. The wind rose in Figure 12 displays the distribution of wind directions based on the observed values from the measurement mast at Fakken. This wind rose pertains to the entirety of the year 2017. The observed values reveal a high occurrence of wind coming predominantly from south to southeast directions.

Furthermore, this direction exhibits a high frequency of wind speed surpassing 14 m/s. This observation holds significant importance as the turbines at Fakken achieve their rated power at 16 m/s. Therefore, considering the dominant wind direction indicated by the wind rose, there is anticipated to be a substantial production of energy.

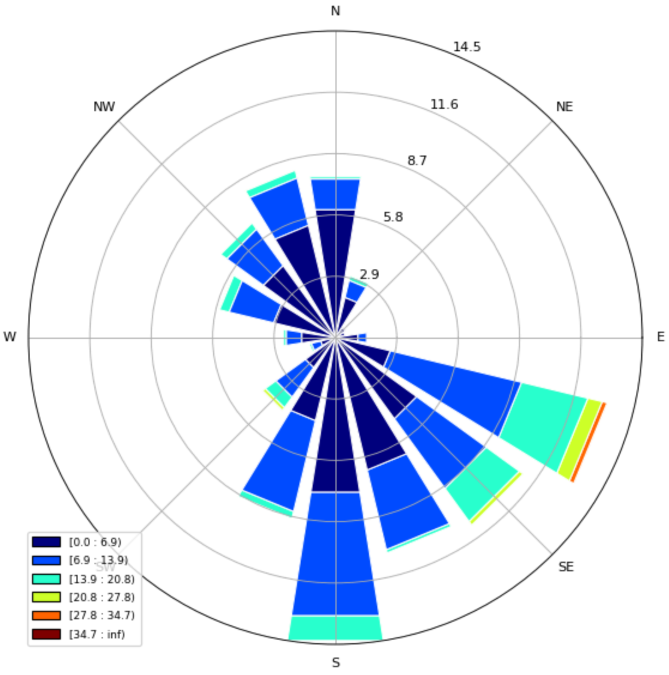

Figure 12: Wind rose from observed data for 2017 at measurement mast.

The wind direction in WRF

The wind rose depicted in Figure 13 represents the results of the 1-year WRF Fakken 1 simulation utilizing a horizontal resolution of 1 km. The wind rose is from the location of the measurement mast at Fakken and illustrates the wind distribution throughout the year 2017. The predominant wind direction, in WRF, is from the southwest. However, the figure also shows a significant occurrence of wind originating from the southeast. Additionally, the figure exhibits a high frequency of wind speed, surpassing 12 m/s from those directions. Upon examination and comparing the wind rose derived from the simulation with the wind rose derived from the observed data, a few noteworthy differences emerge. Firstly, the wind rose is slightly rotated in a clockwise direction compared to the observed data. This suggests a discrepancy in the simulated wind direction.

Furthermore, the frequency of wind occurrences depicted in the simulation appears to be slightly lower in comparison with the observed data. This difference in frequency suggests that the simulated wind patterns do not precisely replicate the real-world wind conditions. These small disparities can have implications for assessing the performance and energy production of the wind turbines at Fakken.

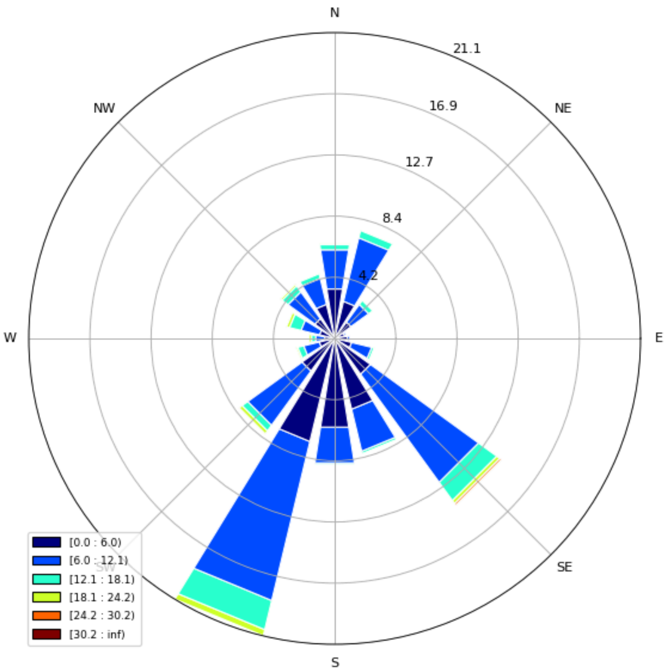

Figure 13: Wind rose from WRF simulation with turbines at Fakken 1, at the location of the measurement mast.

The observed slight rotation in wind direction and lower wind frequency in the simulation may be attributed to the influence of terrain. One possibility is that the model fails to capture certain features that can alter wind direction and intensify wind speeds. The slight rotation of the wind rose suggests that the WRF model does not adequately account for the nearby mountains near the wind park or underestimates its height. Consequently, the simulated wind direction deviates slightly from the observed wind rose. If the WRF model had adequately accounted for the mountains, the estimated wind direction might have been deflected and coming from a more southward direction. This might result in a wind rose more closely aligned to the observed wind rose. However, it remains uncertain what the WRF model precisely registers in terms of the nearby terrain. In summary, the discrepancies in wind direction and frequency between the simulation and observed data may be attributed to the model's limitations in accurately capturing the influence of local terrain features, particularly the nearby mountains.

Figure 14 illustrates the challenges the WRF model faces in capturing terrain features. The model employs a horizontal resolution of 1 km. As a result, specific characteristics of the terrain may be misrepresented or not fully captured, as evident from the disparities between the figures. The black square in the center denotes the location of the wind park.

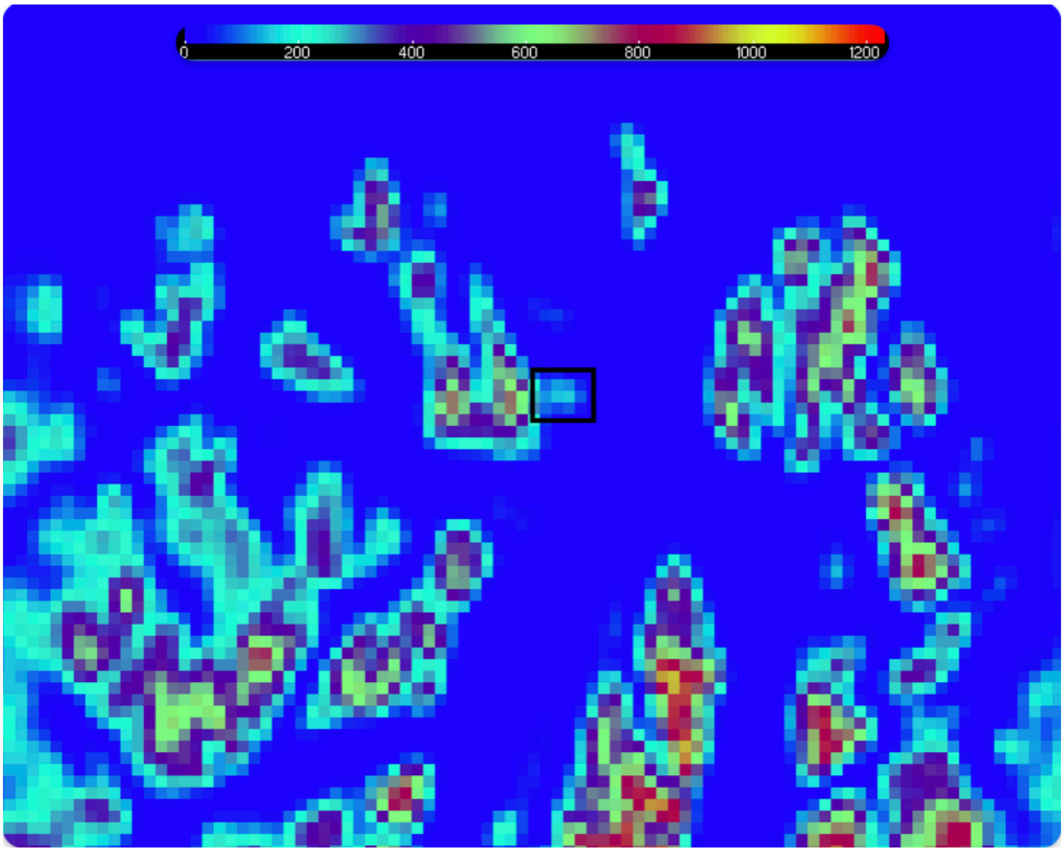

Figure 14: The terrain height in the WRF model with 1 km horizontal resolution.

To further explore the WRF model's limitations regarding terrain representation, a closer look at the terrain height in WRF in the vicinity of Fakken was conducted. This terrain is smoothed out to demonstrate the height and does not produce an accurate representation of the model terrain, only the terrain height in the model for the specific area. This examination aimed to determine the extent to which the simulation neglected important terrain features. Figure 15 provides a visual representation of the terrain height at Vannøya, as well as the location of Fakken. The plot to the left provides a closer view of the model's resolution of the mountain, while the plot on the right gives a closer look at the model's terrain height in the area where Fakken is located. The figure comprehensively assesses the level of features captured by the model in terms of terrain characteristics.

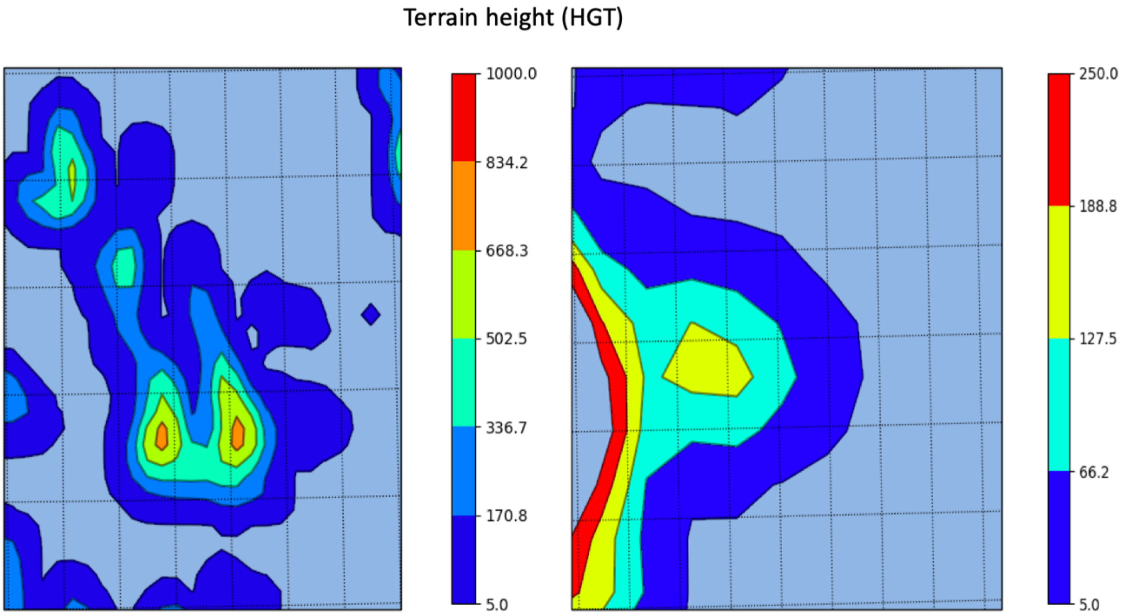

Figure 15: Terrain height from WRF simulation. The picture to the left shows the terrain height on the island Fakken is located on, and the image to the right shows the terrain height on the hills where Fakken is located.

The highest point on the island, the mountain peak to the left, on Vannøya reaches an elevation of over 1000 meters above sea level, while the second highest peak, the one to the right, reaches over 900 meters. Both peaks are shown in Figure 16, demonstrated with a red dot. However, Figure 15 indicates that the WRF model fails to capture this height accurately, estimating the peaks to be slightly over 800 meters at the highest. Although the model acknowledges the presence of the mountain and, thereby its influence on wind flow, the discrepancy in height estimation suggests that the wind flow may differ from the actual conditions.

Figure 16: The Terrain near Fakken, with black dots indicating the small hills and red dots indicating the high peaks.

Another notable oversight in the terrain height of the WRF model is the absence of several small hills located south of the peak to the right, shown in Figure 16 with black dots. One of the hills reaches over 400 meters above sea level, yet the WRF model depicts the terrain in that area to be around 200 meters. This discrepancy in terrain height can directly impact the wind flow directed towards Fakken.

Upon examining the terrain over Fakken itself, the plot on the right in Figure 15, it becomes apparent that the WRF model does not capture the presence of small hills and valleys. Instead, it portrays a single high point with the terrain gradually increasing towards it. This omission of terrain features could affect the wind flow, which indicates a limitation in the WRF model's accuracy in estimation the variation in production at the different turbines.

Comparing the simulated terrain to the actual terrain reveals significant disparities, offering insight into why the WRF model lacks precision. This gives an understanding of the observed disparities between the wind roses derived from the simulation and the wind rose derived from the observed data and the discrepancies in wind frequency.

Fakken 2

Figure 17 shows a wind rose derived from a 1-year WRF Fakken 2 simulation, utilizing a horizontal resolution of 1 km. The wind rose is from the position of turbine F, which is located close to the intended measurement mast at Fakken 2. The wind rose indicates a high occurrence of wind coming from the south direction. The wind rose indicates a high occurrence of wind speed between 6 -12 m/s from the dominant direction, while the wind coming more from the west indicates a higher wind speed but a lower frequency of occurrence.

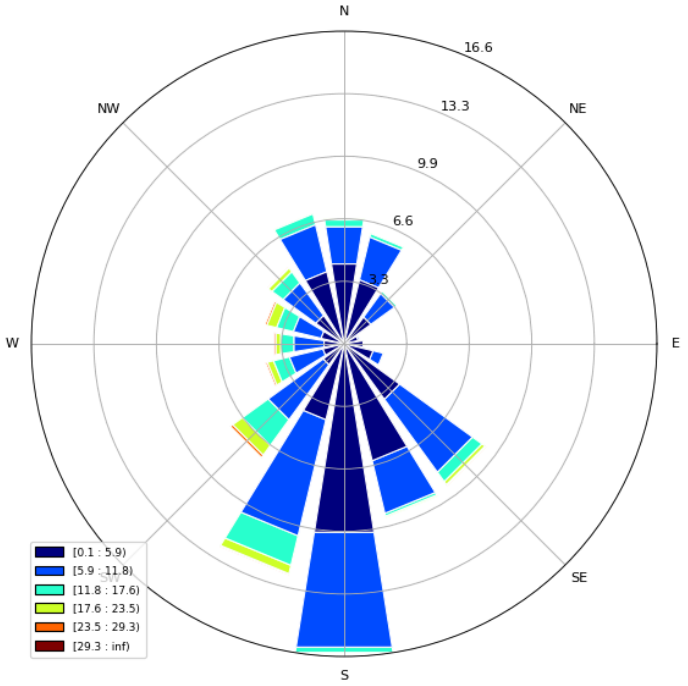

Figure 17: Wind rose from WRF simulation, at turbine F in Fakken 2

The wind roses provide valuable insights into the predominant wind direction, which is crucial when assessing optimal turbine placement. It is also important to ascertain if the model detects the mountains nearby by and to what degree, as understanding the wind direction is key to maximizing turbine performance and minimizing production losses.

To gain further insights into the wind conditions, a second wind rose is generated at the position of turbine D at the northeast edge of the wind park. The additional wind rose provides a more comprehensive view of the predominant wind patterns in the area. The wind rose in Figure 18 shows a significant occurrence of wind originating from the south-southwest direction, with a high wind speed frequency above 12 m/s. Both the wind rose in Figure 17 and Figure 18 indicates an occurrence of wind coming from the west. These attributions interfere with the presence of the nearby mountains, considering the new area is close to the nearby mountain, suggesting again that the hills are not accurately presented in the WRF simulation.

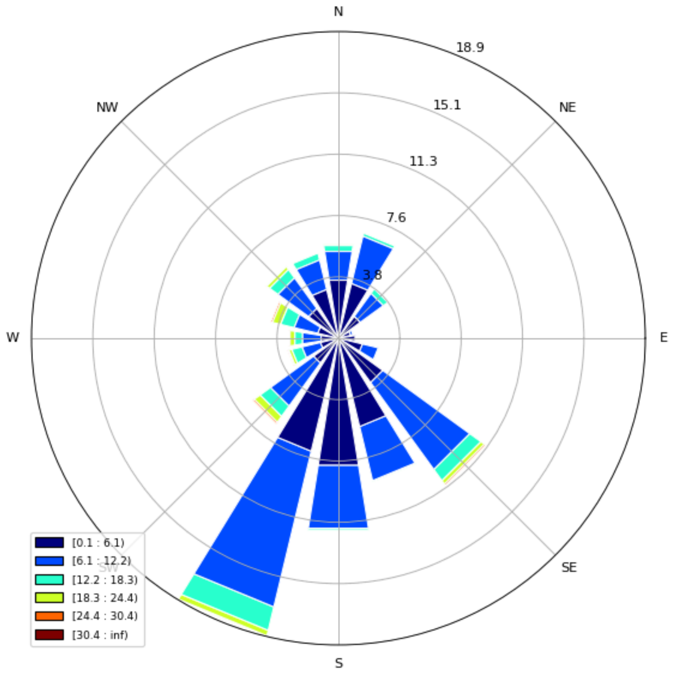

Figure 18: Wind rose from WRF simulation at turbine D, Fakken 2

An analysis of the three wind roses from WRF reveals that the turbine or measurement mast located further east in the two parks predict a wind direction from the southwest, narrowly missing the mountain and being deflected by it. On the other hand, the wind rose from the turbine located more to the west in the parks displayed a dominant wind direction from the south to southeast.

Both wind roses from the turbines at Fakken 2 depict a predominant wind direction from a southerly direction. However, there are occasional instances of wind coming from northerly direction. Wind from this direction has implications for both Fakken 2 and Fakken 1. It’s a known fact that the presence of turbines in the terrain alters the wind flow, meaning that when the wind comes from the north, lower wind speed will be observed at Fakken 1. Consequently, Fakken 1 becomes susceptible to wake losses generated by the turbines at Fakken 2.

It is essential to acknowledge that the wind roses derived from the WRF simulation are not entirely precise. While they offer insights, it is important to keep in mind the limitations of the WRF simulation in accurately capturing the actual wind conditions. Therefore, it is crucial to exercise caution when utilizing these wind roses to assess wind direction.

When evaluating the expansion of the wind park, it is essential to consider the consequences of the wind coming in from the north. The wake losses caused by the turbines at Fakken 2 will impact the performance and energy production of Fakken 1. Therefore, an assessment of the layout of Fakken 2, including the positioning and spacing of the turbines, is necessary to mitigate these wake losses and optimize overall energy production. By considering these factors, the wind park can be designed to be more efficient and maximize its potential output.

Wind Direction in WAsP

The wind rose generated by the WAsP model adopts a different format that illustrates the frequency of wind directions but does not include the magnitude of the wind speed. Despite the absence of wind speed information, the wind rose can still provide valuable insights into the predominant wind direction.

Figure 19 depicts the wind rose derived from the WAsP simulation with the observed data. The figure shows a high occurrence of wind coming from southeast. Additionally, there is a significant occurrence of wind coming from the south. The wind rose is based on the observed wind data from the measurement mast, meaning that this wind rose is expected to show a resemblance to the wind rose from the measurement mast.

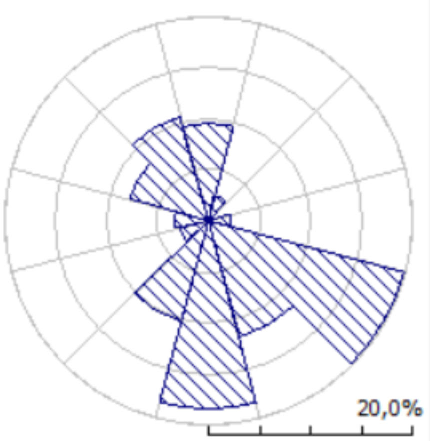

Figure 19: Wind rose from WAsP for observed data for 2017.

Figure 20 depicts the wind rose from the WAsP simulation with the Generalized Wind Atlas (GWA). The figure illustrates two primary wind directions, one from southeast and another from southwest. Additionally, there is a significant frequency of wind coming from the south.

The contrasting wind roses between the simulation with GWA and the simulation with observed data could be attributed to a low resolution on the terrain on the input data for the simulation with the GWA. The GWA has a course resolution, resulting in a different representation of the wind patterns.

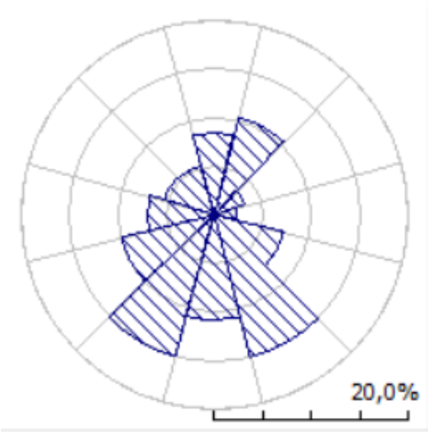

Figure 20: Wind rose from WAsP with GWA.

Despite the initial expectation that the wind roses would display more similarity, Figure 19 and Figure 20 show notable differences between the two simulations. While both wind roses indicate a high occurrence of wind coming from a southerly direction, there are not many other similarities. There is a slight indication that the wind rose in Figure 20 could be rotated clockwise, but they still display different frequencies. These dissimilarities suggest that the simulation with the observed data will perform better than the simulation with GWA. The simulation with observed data is expected to provide a more accurate representation of the wind patterns over the area.

Both the WRF and WAsP GWA wind roses have wind that is slightly rotated compared to the observed data. This could be due to the models being unable to correctly recreate the wind direction, due to smoothing of the terrain. Or it could be due to the measurement not being perfectly calibrated regarding wind direction. Some of the wind roses from the turbines are evaluated to evaluate if that is the case. The wind roses from the turbines nearby correspond to the wind rose from the measurement mast. This means that the instrument is likely not wrongly calibrated for wind direction, and the reason the wind roses from the models are rotated is due to the models.

4.2 Observed data vs WRF simulated data

To assess the accuracy of the WRF model's wind speed estimates a comparison is made with the observed wind speed data. The data spans the entirety of 2017 and is plotted together for analysis. An evaluation of the degree of agreement between the observed wind speed and the WRF simulated wind speed is obtained by examining these two times series. The comparison gives valuable insight into the performance and reliability of the WRF model.

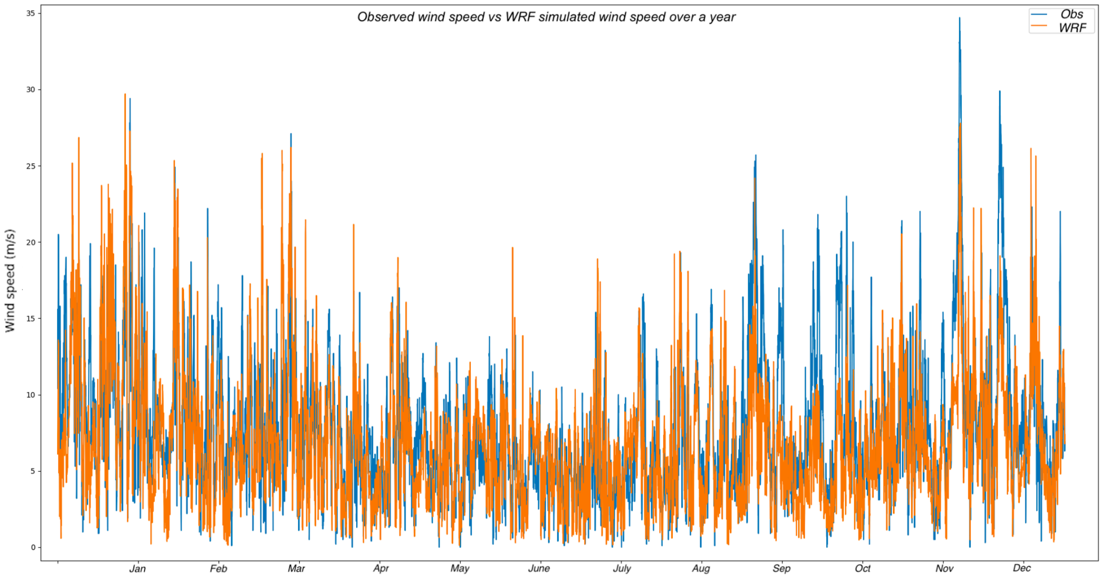

Figure 21: The observed wind speed (blue) vs. the simulated wind speed (orange) in WRF

Figure 21 provides the visual representation of the degree of agreement between the simulated and observed wind speed values. The observed wind speed is in the blue line, while the simulated wind speed from WRF is the orange line. Although there are some deviations, this is common in numerical modeling due to uncertainties in initial conditions, simplification in the physical equation used to describe the atmospheric conditions, and the weather unpredictability.

At first look, the model is expected to yield good results as the deviations are not severe. However, upon closer examination of the figure, some deviations are observed during August, September, and October. The WRF model tends to underestimate high wind speeds (Carvalho et al., 2014), which might explain these discrepancies. Alternatively, other factors, such as a specific weather phenomenon or local geographic features that the model does not fully capture could contribute to these discrepancies. Therefore, more analysis is needed to understand the deviations observed during these months.

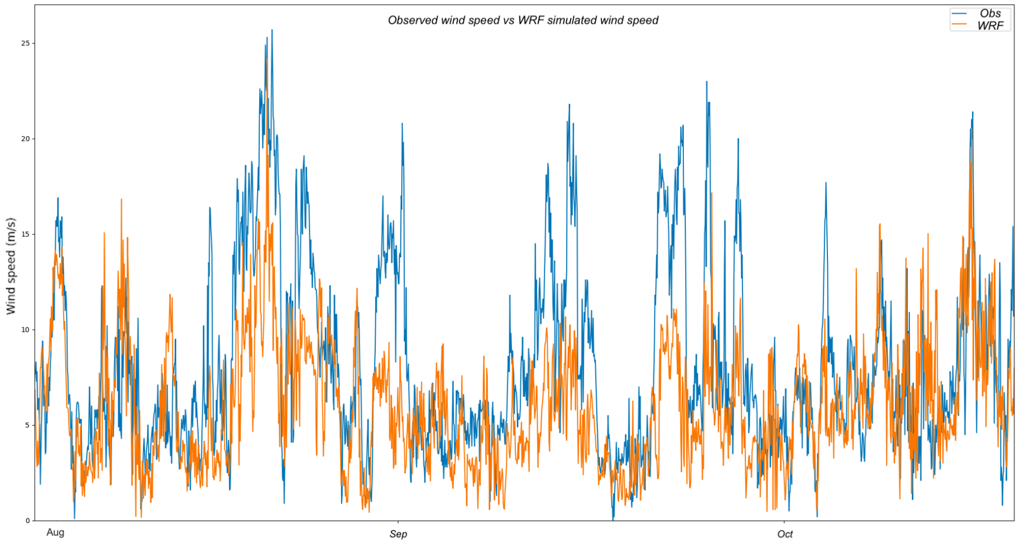

Figure 22: A closer look at the observed wind speed vs the simulated wind speed in WRF.

The figure shows discrepancies between the observed wind speed and simulated values. The figure shows that the model tends to underestimate wind speeds at high wind incidents, with the simulated values constantly lower than the observed values. During this period, the simulated wind speed is rarely over 15 m/s, while the observed wind speed is frequently over 15 m/s.

The underestimating could be due to the model's resolution. Running a low resolution on the model, simplifies the topography effects of the area and smooths out the model terrain. As a result, fine details in the terrain and local geography are not captured, which can impact wind speeds and create discrepancies between the observed and simulated values.

The underestimation of wind speeds has significant implications for energy production estimates. The turbines at Fakken 1 produce a rated power, 3 MW when the wind speed exceeds 16 m/s. For example, at 12 m/s it only produces around 2500 kW, indicating that even a tiny underestimate of only 3 m/s could result in underestimating 500 kW per hour. An underestimation of wind speed results in an underestimation of energy production. This is a significant concern since obtaining accurate estimates for new wind park areas is crucial in evaluating whether it is worthwhile to establish a wind park in that location. This underscores the importance of ensuring that wind speed estimates are as accurate as possible.

Table 1: Comparison between the WRF estimated wind speed and the observed wind speed.

Model	RMSE	MAE
WRF Fakken 1	13,2	2,7

The statistical methods in the table show the deviation between the WRF estimated wind speed and the observed wind speed. The table shows a very high RMSE value. The RMSE has the benefit of penalizing significant errors more, shown here by the very high value. The MEA value is also high but not as high as the RMSE value. This confirms that the modeled wind speed values deviate from the observed wind speed, and that the deviation is significant on several occasions.

4.3 Energy production models

To evaluate which model yields the most accurate energy production estimations, a comparison is conducted for Fakken 1. The observed energy production data from each turbine at Fakken 1 is compared with the simulation from the two models, WAsP and WRF. For each model two simulations are considered, resulting in four sets of simulated energy production data. This analysis can determine which model matches the actual observed energy production at each turbine. The model with the least deviation is the better for energy prediction estimation.

The two simulations from the WAsP Fakken 1 simulation considered here are the one with Global Wind Atlas (GWA) as input data and the other with data observed data from 2017. The two simulations from the WRF model considered are WRF Vannøya, without any turbines in the terrain, and WRF Fakken 1, with turbines on Fakken 1.

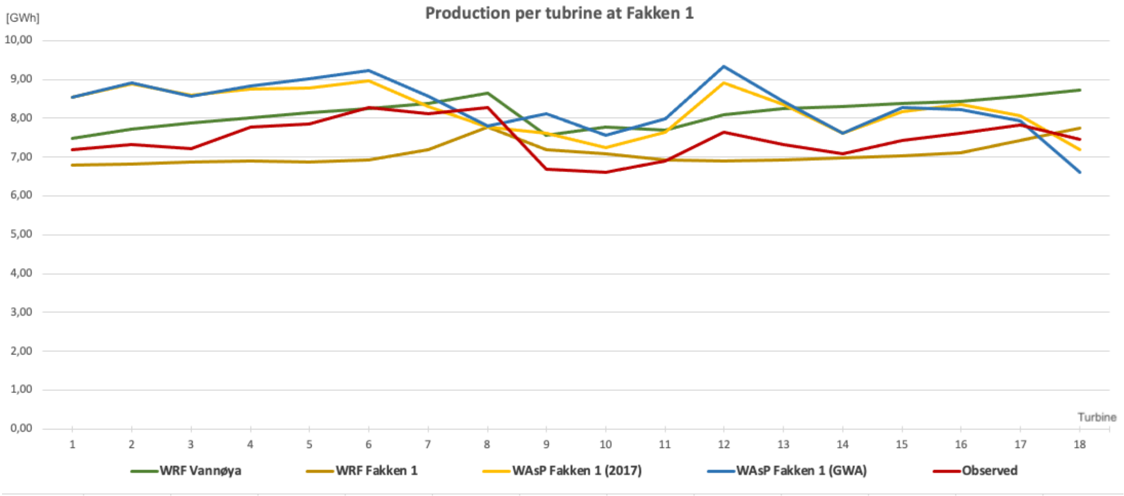

Figure 23: Yearly energy production per turbine on Fakken 1

The estimated energy production from WRF and WAsP using different setups are shown in Figure 23 and the observed production for each wind turbine in 2017. The plot demonstrates a good agreement between the models.

The energy production simulations from WAsP show higher production for most of the turbines, particularly for the first 7 turbines, and then again for turbines 9 and 12, with the WAsP simulation using GWA providing the highest values. Comparing WAsP with measured production, Figure 23 shows that WAsP simulations estimate higher output than the observed production except for at turbine 8. Notably, the second row of turbines in the WAsP simulations exhibits a decrease in production, likely due to wake loss.

On the other hand, the WRF Fakken 1 simulation consistently predicts lower production, except for turbines 9 and 10, where the observed production is lower. The WRF Vannøya simulation, without any turbines in the terrain, which allows for a more unobstructed wind flow and zero wake losses, is expected to yield higher energy production. While the WRF Vannøya does produce higher output than the WRF Fakken 1 simulation and the observed production, it still shows lower energy production than the WAsP simulations, especially for the first row of turbines. This discrepancy can be attributed to WRF's tendency to underestimate wind speed, resulting in an underestimation of energy production.

The plot shows that the simulation picks up some of the same trends in production. Both WAsP simulations and the observed production show higher energy production at turbine 12 than the other turbines close by. Turbine 12 is situated on a favorable wind-exposed hill at the highest point in Fakken 1. The WRF model is not able to detect a higher production at this specified turbine. As described in Figure 14, the WRF model has a too-low horizontal resolution to show local terrain variations, and this is also the reason for underestimating the production at turbine 12. Conversely, most simulations indicate a decrease in output at turbine 18, except for the WRF simulation without turbines, which aligns with expectations, since it does not consider wake losses.

The lines representing the WAsP simulation and the observed production exhibit more production variability between the turbines than the WRF simulations. This could be due to the minimal terrain features registered by the WRF model, resulting in the turbines experiencing the same wind flow.

It is worth noting that the WRF simulations are performed at a horizontal resolution of 1 km, with interpolation executed to enhance accuracy within the grid cells. Since the entire wind park is almost within a 1 km range, this factor influences the results obtained from the WRF model, resulting in smoother lines.

In both the WAsP simulations the overestimation is anticipated, since the WAsP model typically underestimates the wake loss effect. Additionally, for the first WAsP simulation, the Global Wind Atlas summarizes wind data over multiple years, meaning some discrepancies may be expected between the simulated and observed energy production.

It is important to note that the observed production encompasses various losses encountered over a year, including those caused by maintenance shutdowns, adverse weather conditions such as high winds or icing, and other operational factors. The models do not incorporate these specific losses into their calculations. They consider wake losses and high winds to a certain degree. Consequently, if a turbine remains shut down for a week due to maintenance, this information would only be reflected in the observed production values and not captured by the models.

The total estimated wind park production for each model is summed up in the table below. The total observed production is 134 GWh. Among the four simulations the WRF Fakken 1 simulation comes closest to estimating the total production. However, it still underestimates the production. Since the model simulations do not consider the losses incurred during a year of production, the difference between the estimated and actual production would likely be more prominent.

Table 2: Total yearly production

Models	Total yearly production (GWh)
WRF Vannøya	146,0
WRF Fakken 1	127,0
WAsP Fakken 1 2017	147,0
WAsP Fakken 1 GWA	149,0

Overall, the comparison of these simulations highlights the differences in energy production estimations between the WRF model and the WAsP model, as well as the variations compared to the observed production. The WAsP simulations consistently yield higher estimates, while the WRF simulations tend to predict lower production.

The estimation error in turbine production is evaluated by calculating the estimation error between the model's estimated value and the observed value at each turbine using the equation in chapter 2.5. The table below shows the estimation errors in energy production per turbine for the different models.

Table 3: Statistical evaluation of the models production estimates.

Models	RMSE turbine production	MAE turbine production	MAPE turbine production	Bias turbine production
WRF Vannøya	0,75	0,65	9,0 %	0,65
WRF Fakken 1	0,62	0,54	7,0 %	-0,39
WAsP Fakken 1 (2017)	0,91	0,82	11,1 %	0,74
WAsP Fakken 1 (GWA)	1,06	0,98	13,3 %	0,83

The table above demonstrates how close the models are at estimating the energy production. It indicates that the WRF Fakken 1 simulation is the one that is closest to the observed values. The statistical methods used are negatively oriented scores, meaning that the lower values indicate better accuracy. Based on the table, the WRF Fakken 1 simulation consistently achieves the lowest values across all the statistical methods, indicating a better performance in estimating the production at each turbine. The mean absolute percentage error estimated that the model estimation is 9% off the average. On the other hand, the WASP Fakken 2 with GWA simulation exhibits the highest values for all the statistical methods, suggesting that it deviates the most from the observed production.

However, as mentioned over a year, the wind park faces various challenges that result in temporary shutdowns of individual turbines. These factors have an impact on the overall energy production. Unfortunately, quantifying the exact magnitude of the losses can be challenging, as they vary from year to year. Troms Kraft has provided that for the year 2017 the reduction due to production losses was approximately 5 %, not considering wake losses. By considering the production losses, it’s possible to understand the model’s accuracy in estimating energy production. The models do not consider these losses when evaluating the energy production. By subtracting 5% of the model's estimated production, it's possible to see how close they align with the actual energy production. It’s important to note that the 5% reduction only applies to this year and varies yearly.

Table 4: Yearly production with production losses.

Models	Total yearly production (GWh)	Production with 5% losses (GWh)
WRF Vannøya	146,0	138,7
WRF Fakken 1	127,0	120,7
WAsP Fakken 1 2017	147,0	139,7
WAsP Fakken 1 GWA	149,0	141,6

In the table above the total estimated production for Fakken 1 is shown. Additionally, the production with a 5% loss is shown. The table shows that with the 5% loss, the WRF Vannøya simulation is the closest to the actual production, 134 GWh. However, the WAsP Fakken 1 simulation with data from 2017 only predicts 1 GWh more than the WRF Vannøya simulation. Since the WAsP simulation includes the turbines and considers wake losses, it’s likely the best model to use to evaluate the energy production.

4.4 Production in WRF

A comparison of three WRF simulations conducted over the year 2017, with a horizontal resolution of 1 km, is displayed in Figure 24. The blue line shows the WRF Vannøya results, where the energy production is calculated from the wind speed, as explained in Chapter 3.3. The orange line shows The WRF Fakken 1 results, which considers the impact of obstacles on wind flow and accounting for wake losses. The green line results from the WRF Fakken 2 simulation, which considers wake losses from turbines at Fakken 2 and their influence on the energy production at Fakken 1.

Figure 24 illustrates the variation in energy production among the different simulations highlighting the differences in having turbines in the terrain. Moreover, the graph also depicts the influence of Fakken 2 on the energy production at Fakken 1. By examining the energy production at each turbine throughout the year, the figure provides insights into the impact of turbine placement, terrain, and wake losses on the overall energy production in the WRF simulation.

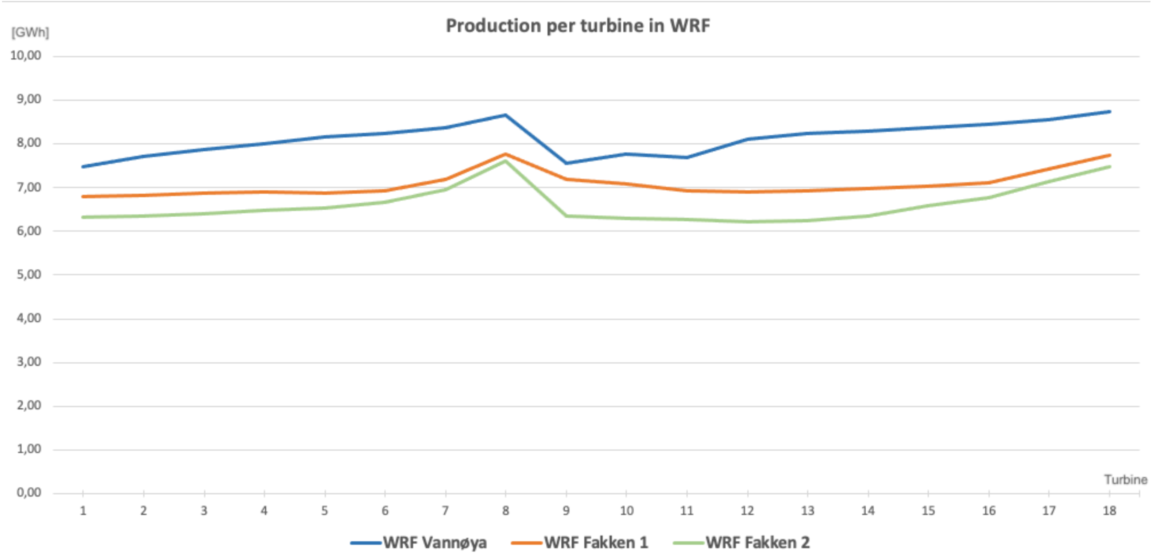

Figure 24: Production in WRF for Fakken 1

The graph displays smooth lines with minimal fluctuations. The overall trends of the lines are similar, with an increase in production observed at turbine 8, located furthest to the east. Considering the WRF simulation has a resolution of 1 km, it is expected that there would not be substantial differences in production between the turbines, meaning that the smooth curve in this context is reasonable.

As expected, the WRF Fakken 2 simulation predicts the lowest energy production, while the WRF Vannøya simulation yields the highest energy production. Interestingly, the impact of wake losses on the second row of turbines is not very pronounced, with a slight decrease in production observed but insignificant. However, production increases along the second row of turbines toward the east, influenced by the dominant wind direction.

All the simulations capture the decrease in production at turbine 9. this decrease could be due to wake losses and its position, with the wind flow potentially being influenced by the terrain and the mountain deflecting the wind. Overall, the simulations demonstrate consistent trends in production, with the main difference being the presence of turbines in the terrain. The effect of the new wind park on the old one is evident but not considerable.

Interestingly, the WRF Vannøya simulation exhibits similarities to the simulations with turbines. Since this simulation does not consider wake losses, the differences in production between turbines are attributed to terrain factors rather than wake losses. The production in the WRF Vannøya simulation increases at turbines 12 and 13, while at the other two, the production decreases slightly at these turbines—a clear indication of wake losses. The turbines from 12 to turbine 17 should experience the most significant impact from wake losses, as they are directly in the path of the wind coming from the first row of turbines under the prevailing wind direction, which is confirmed by the figure.

The WRF Vannøya simulation also highlights the influence of the dominant wind direction on production, indicating increased output for turbines the easterly in the park. The wind from the fjords is most significant over the ocean outside Fakken, and the turbines closest to that area experience the highest magnitudes. Conversely, the turbines located furthest west are shielded by the mountain on the island.

The introduction of Fakken 2 into the wind park is expected to impact the overall energy production of Fakken 1. The WRF Fakken 2 simulation estimates a decrease in the yearly production to 119 GWh. This estimate is noticeably lower than the initial estimate of 127,5 GWh for the wind park without Fakken 2. The WRF Fakken 2 simulation highlights the influence of the additional turbines on the wind flow and the subsequent reduction in energy production.

4.5 Production in WAsP

Figure 25 shows the WAsP simulated energy production per turbine. The simulation using observed values is expected to outperform the simulation with GWA. However, Figure 25 shows a remarkable similarity between the two models in predicting energy production for each turbine. The lines closely follow each other with few noticeable discrepancies. The similarity suggests that the GWA provides a reliable estimation of energy production. The figure highlights the effectiveness of the GWA in capturing the overall wind conditions and their impact on production.

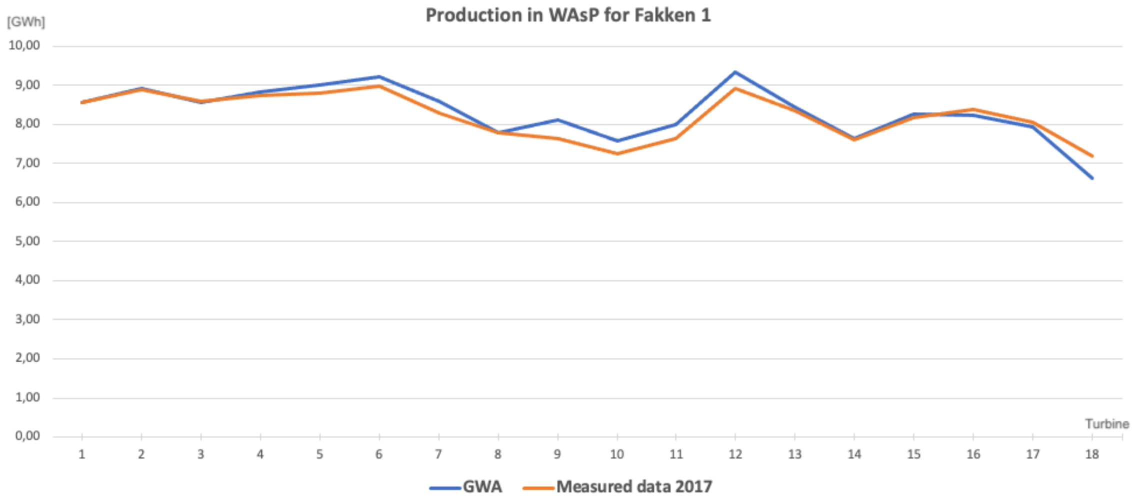

Figure 25: WAsP simulations.

The WAsP simulations provide insight into the difference between observed measurements and the Global Wind Atlas as input data. Surprisingly, both simulations yield similar results. The simulation using the observed data is expected to perform better since it is specific to the investigated year. While the GWA is more generalized and encompasses wind data from multiple years.

The observed data is fitted to the model, and the input data is processed to be applied over the area. It is calculated to provide the different turbine locations from the measurement mast. This calculation considers the influence of terrain.

However, it is worth noting that the GWA simulation does exhibit a slight deviation in their prediction; it tends to estimate a slightly higher production compared to the simulation with observed data. This could be attributed to inherent differences between the two approaches, such as variations in the data treatment and factors influencing the wind flow at each turbine location.

Regarding wake losses, the figure does not show an apparent effect of wake losses affecting the second row of turbines. There is a slight decrease in production for the second-row turbines, except for turbine 12. Still, the reduction is not as substantial as expected if wake losses were adequately accounted for. This aligns with the tendency of the WAsP model to underestimate wake losses, leading to an overestimation of production. This discrepancy could be due to simplifications in the wake loss calculations or limitations in accurately representing the complex interactions between the turbines and the wind flow.

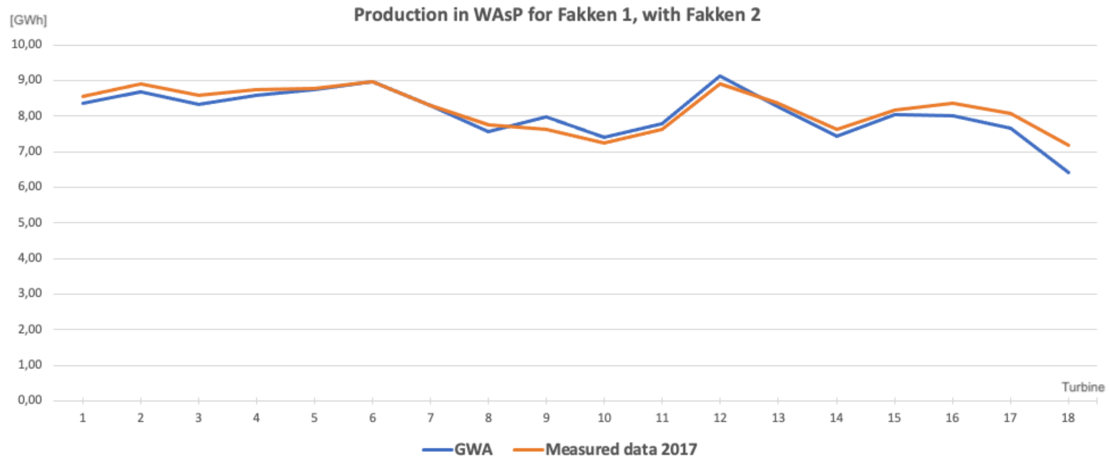

Figure 26: WAsP simulations with Fakken 1 and Fakken 2

Figure 26 shows the WAsP Fakken 2 simulated production per turbine. The plot is similar to the plot in Figure 25, which is to be expected. The data shows a marginal decrease in production at each turbine; the total reduction in energy production according to the simulations with observed data, is around 1 GWh. However, the GWA simulation shows a slightly more significant decrease in production per turbine. Visually the lines are now closer to each other, indicating a decrease in production across all turbines for the simulation with GWA. Despite the reduction, the trends remain the same, with lower values.

This indicates that the WAsP simulation with GWA captured more wake losses, resulting in a greater reduction in energy production compared to the simulation with observed data. The closer alignment of the lines further highlights the impact of wake losses on overall energy production.

Overall, while the WAsP simulations provide valuable insights into energy production estimates, it is crucial to consider their limitations, particularly in accurately predicting wake losses.

Compared to the observed production

WAsP GWA is indicating the annual production in GWh. To further evaluate the performance of the GWA, a comparison is made with the average production of the wind park over the last few years. Although the wind park was established in 2012, it did not have a full year of production until 2013. The data obtained from NVE for 2013 to 2021 is presented in the table below.

Table 5: Average production on Fakken. Data collected from NVE

Year	Production
2013	128
2014	124
2015	140
2016	124
2017	133
2018	128
2019	133
2020	152
2021	140
Average	**134**

Since the GWA represents averaged wind data over the past years, it is expected to align closely with the observed average production. The WAsP Fakken 1 simulation with GWA estimates the annual production to be around 149 GWh, which is higher than the average observed production, which is approximately 134 GWh. Conversely, the WAsP Fakken 1 simulation with observed data for 2017 estimated production of approximately 147 GWh. Both simulations indicate a much higher production compared to the average production.

4.6 Production on Fakken 2

Figure 27 shows the estimated energy production per turbine in Fakken 2 based on the proposed turbine locations. The blue line shows the results from the WRF Fakken 2 model. The orange line shows the results from the WaSP Fakken 2 model with GWA, and the green line shows the results from the WAsP Fakken 2 model with the observed data from 2017. Juxtaposing these models allows for the assessment and comparing their estimations for production on Fakken 2.

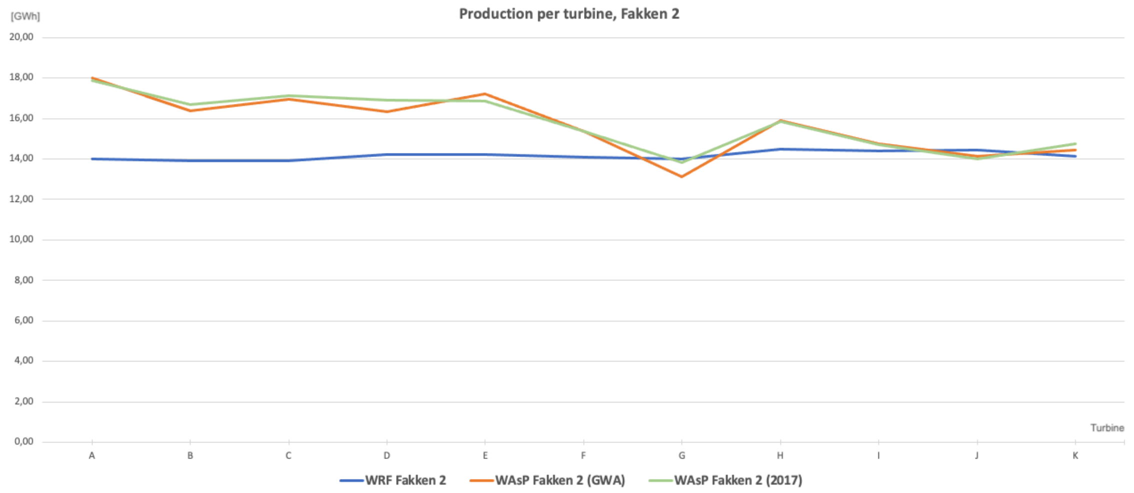

Figure 27: Energy production on Fakken 2 per turbine

The WRF simulation estimates an annual production of approximately 14 GWh for each turbine, while the WAsP simulations predict a higher yearly production. The WRF model estimates a total production of 155 GWh, while the WAsP simulations estimate a total production of around 173 GWh.

Table 6: Yearly production on Fakken 2.

Models	Total yearly production (GWh)
WRF Fakken 2	156,0
WAsP Fakken 2 (GWA)	172,0
WAsP Fakken 2 (2017)	173,8

Although there are discrepancies between the models, determining which turbine will generate the most or least power is challenging. Since these assessments pertain to a new area, no measured data for comparison is available. However, by comparing the data for Fakken 1, we can gain some insight into how the model's estimations align with actual values. From the comparison with the observed data, we saw that the WAsP model gave a more accurate assessment after the production losses that are experienced throughout a year were added. With a 5% production loss added the models now estimate lower total production, shown in the table below.

Table 7: Yearly production on Fakken 2 with production losses.

Models	Total yearly production (GWh)	Production with 5% loss (GWh)
WRF Fakken 2	156,0	148,2
WAsP Fakken 2 (GWA)	172,0	163,4
WAsP Fakken 2 (2017)	173,8	165,1

It is worth noting that the new intended turbines at Fakken 2 are twice as powerful as those at Fakken 1, suggesting significantly higher production even with fewer turbines.

In terms of the model estimates, the WAsP simulations show similar values, as expected, and exhibit consistent trends, indicating which turbines are expected to yield higher production and which are not. However, the WRF model demonstrates a more uniform distribution of estimated production without significant fluctuations. The model suggests that the turbines will generate similar energy production, with no turbine standing out as significantly more productive than the others.

One interesting observation is the impact of wake losses from Fakken 1 on the production of Fakken 2. If Fakken 2 were established in an area with the same wind conditions but with no turbines in front of it, production would be even higher. However, considering the wind roses, which indicate that the dominant wind direction is from a southerly direction, the wind flow passes through Fakken 1 before reaching the turbines on Fakken 2. This results in reduced wind speed and turbulence.

Placement of turbines

The figure below depicts the resource grids positioned over Fakken 1 and Fakken 2 in the WAsP model, corresponding to the hub height of the turbines in each area. These resource grids provide information on the average wind speed.

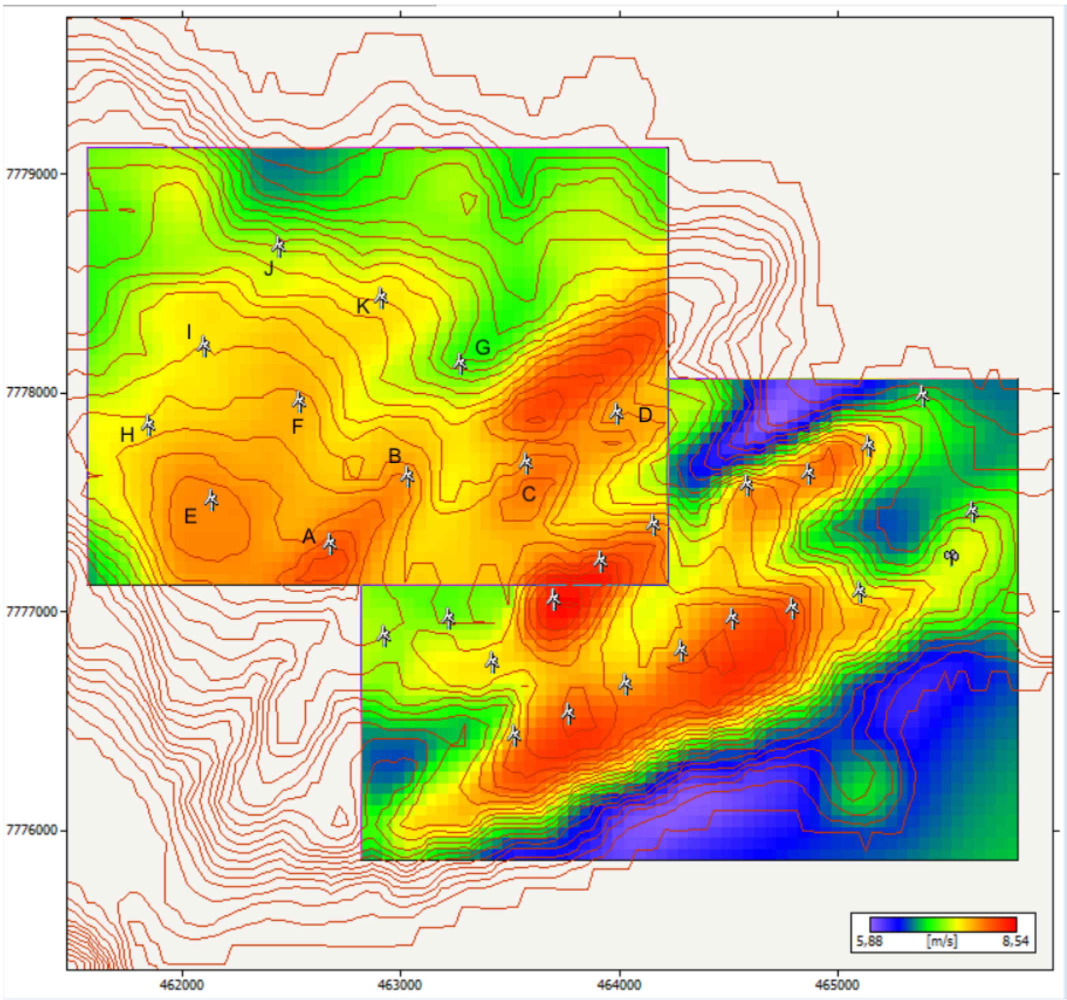

Figure 28: Resource grid with mean wind speed over Fakken 1 and Fakken 2

Figure 28 displays the resource grid applied to Fakken 2, illustrating the mean wind speed across the area. The regions in red indicate the highest mean wind speeds. These places are advantageous for turbine placement, indicating high potential for high energy production.

The utilization of WAsP for this evaluation is advantageous due to its resource grid feature, which gives a great look at beneficial places to place a turbine. And after the placement of a turbine, it only takes minutes for the model to calculate its production. In contrast, conducting similar assessments with WRF would require several hours to obtain the desired results.

The resource grid incorporates the intended wind turbine generator into its calculations, allowing for a more accurate estimation of potential turbine performance at various positions. The generator incorporating the resource grid can show the advantageous places for energy production, with a resource grid showing the AEP over the area.

By leveraging the resource grid, we can optimize the turbine locations based on its recommendations. After adjusting the turbine positions accordingly, we recalculated the energy production to assess if any improvements have been achieved. Considering the spacing between the turbines and the impact of wake losses on the wind flow during this process is crucial.

The WAsP model offers a useful tool for evaluating wake losses in the area. However, it is important to acknowledge that the model underestimates wake losses, so this factor should be considered when interpreting the results.

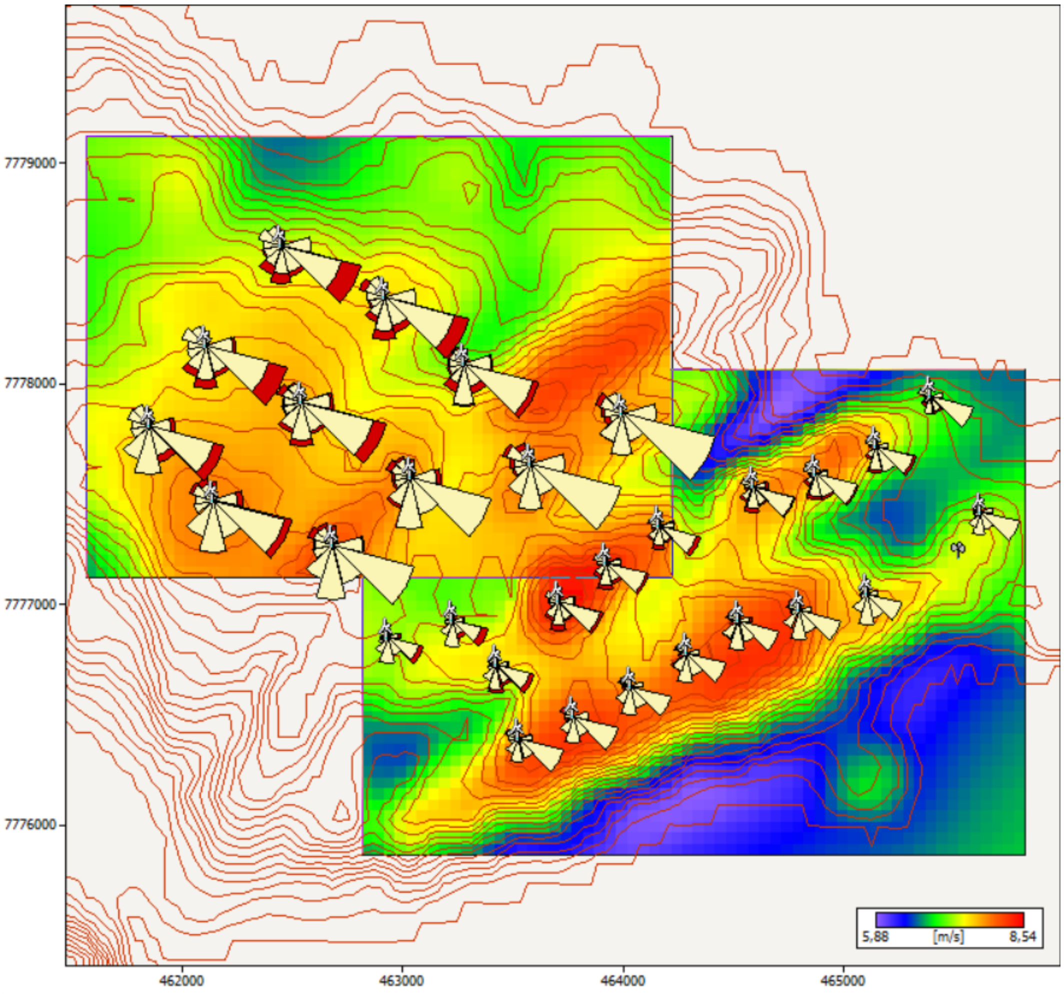

Figure 29: Resource grid with wind roses showing AEP gross & wake losses

Figure 29 depicts two resource grids and wind roses showing the AEP gross and wake losses.

Figure 29 indicates that there are some wake losses present, but they are not significantly pronounced. This suggests that Fakken 2 will be affected by Fakken 1, but the impact is not substantial. Several factors may contribute to this, including the different heights of the turbines on Fakken 1 and on Fakken 2, the complex area terrain in the area, or most significantly the model underestimates wake losses.

Interestingly, the figure reveals that the front row of turbines on Fakken 2 does not experience wake losses from Fakken 1. Instead, they primarily encounter wake losses from turbines located behind them. This could be attributed to the turbine heights or the characteristics of the terrain.

Additionally, the models provide insights into the presence of wake losses in Fakken 1. Fakken 1 already experienced some wake losses on its second row of turbines, but with the addition of Fakken 2, it is expected to experience more wake effects. This is due to the shifting wind direction throughout the year, as indicated by the wind roses. There is an occurrence of wind coming from the north. This wind flow initially passes through Fakken 2 before reaching Fakken 1. Resulting in reduced wind speed on Fakken 1 when the wind comes from the north. This shows the expected decrease in energy production at Fakken 1, although the reduction is not significant.

Considering the anticipated decrease in energy production from wind coming from the north, the estimation from WAsP is surprising. Several factors could contribute to this disparity, such as the complex terrain, differences in turbine heights, underestimation of wake losses, or the wind from the north not substantially impacting the turbines.

New turbine positions

In order to maximize the energy production at Fakken 2, a closer look at each turbines estimated production is conducted. The main idea was identifying the turbines with the lowest estimated production and moving to a better placement. The aim is to place the turbines in areas with higher mean wind speeds, indicated by the red areas on the resource grid. Additionally, the positions are optimized to minimize the wake losses.

The new layout of the turbines with the corresponding wake losses is shown in the figure below. The figure demonstrates small wake losses, with the back row turbines experiencing the most wake losses. The location of the new positions to the turbines is given in Appendix A.

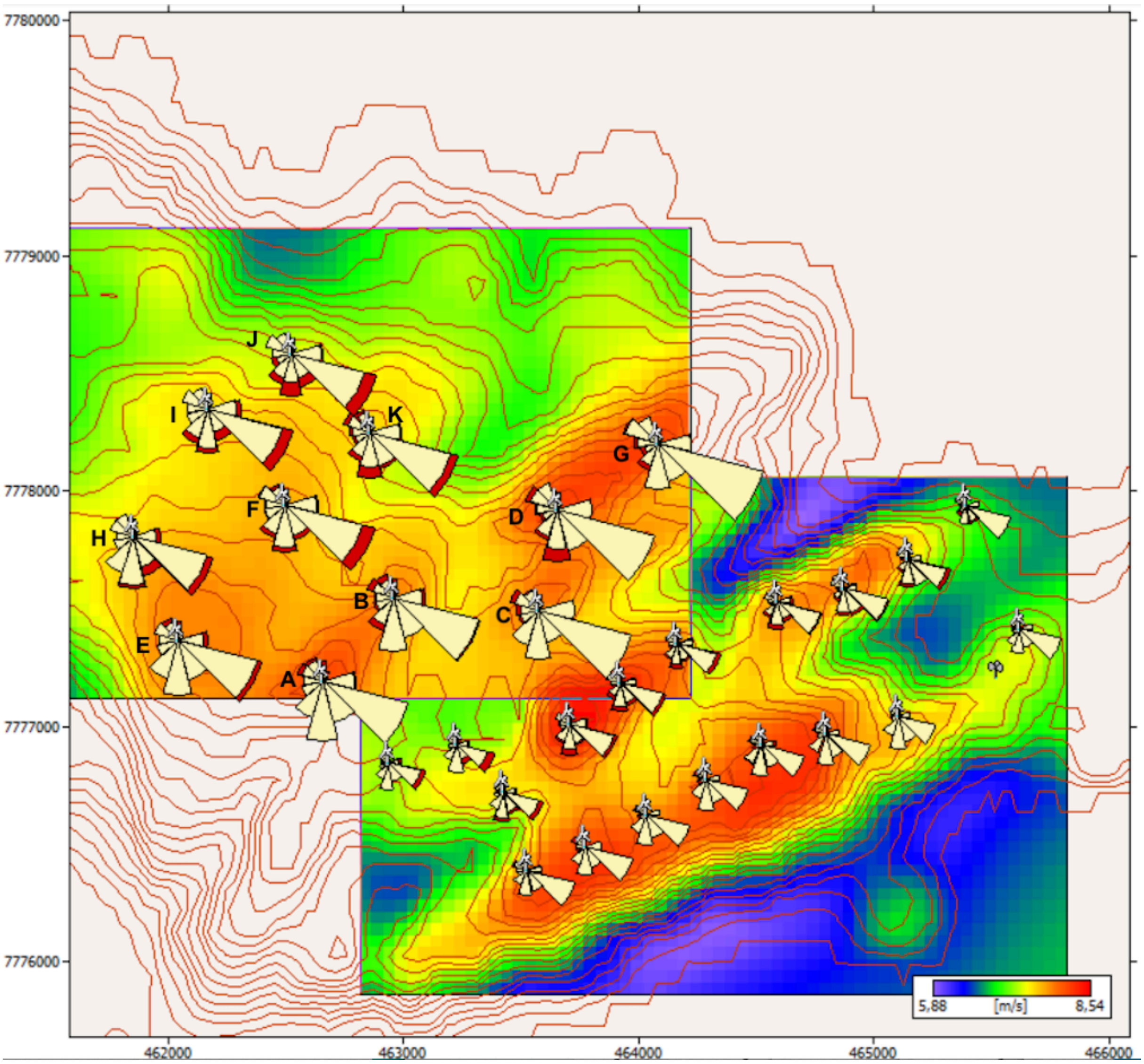

Figure 30: New turbine positions, with wind roses showing the AEP gross and wake losses.

These adjustments are not massive but rather minor alterations to position the turbines in more advantageous spots. All the turbines have been moved, but some only slightly to enhance their position by moving them away from a slope they were on and moved to a higher point. The original proposed turbine locations already yielded considerable energy. However, with fine-tuning, the production output can be improved. Two turbines are now positioned atop a favorable wind-exposed hill, turbine D and G, benefiting from good wind conditions. These two turbines were the ones that had the most drastic change in placement.

Table 8: Yearly production on Fakken 2 with new positions.

Simulation	Total yearly production (GWh)
WAsP Fakken 2 (2017)	173,9
WAsP Fakken 2 (2017)*	180,7

The WAsP simulation with observed data for 2017 estimated that the total energy production for Fakken 2 is around 173,9 GWh. However, with the new enhanced turbine positions, noted as WAsP Fakken 2 (2017) * in the table above, the total estimated energy production has increased to 180,7 GWh. This represents a notable increase of 7 GWh, equivalent to the energy output that could be generated by adding a turbine at Fakken 1.

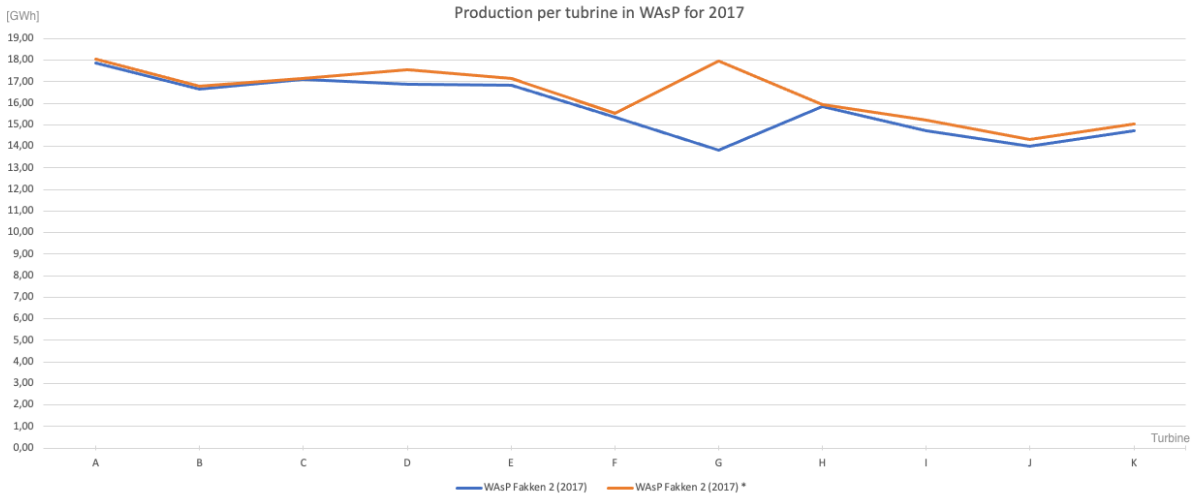

Figure 31: Production per turbine in WAsP with new turbine positions.

In Figure 31, the blue line represents production per turbine for the original positions and the orange line for the new ones. The figure shows that production has increased for all the turbines, even if only slightly for some. The most significant difference can be observed for turbine G, which is situated furthest to the east in Figure 30. This turbine has been relocated to the wind-exposed hill, as opposed to its previous position behind the hill at a lower elevation. This adjustment resulted in a significant increase in energy production. Before the adjustment, the estimated turbine production was 13,8 GWh, and after, the estimated production increased to 17,95 GWh.

4.7 Results from LiDAR

The wind rose from the LiDAR is shown in Figure 32. The wind rose shows a high occurrence of wind coming from the south to the southwest and a high occurrence of wind coming from the north. It demonstrates wind speed up to 19 m/s, but the highest occurrences of wind speeds are between 11 m/s and 15 m/s.

It's important to note that the LiDAR is not expected to give accurate values due to lacking data, affecting wind speed and direction calculation.

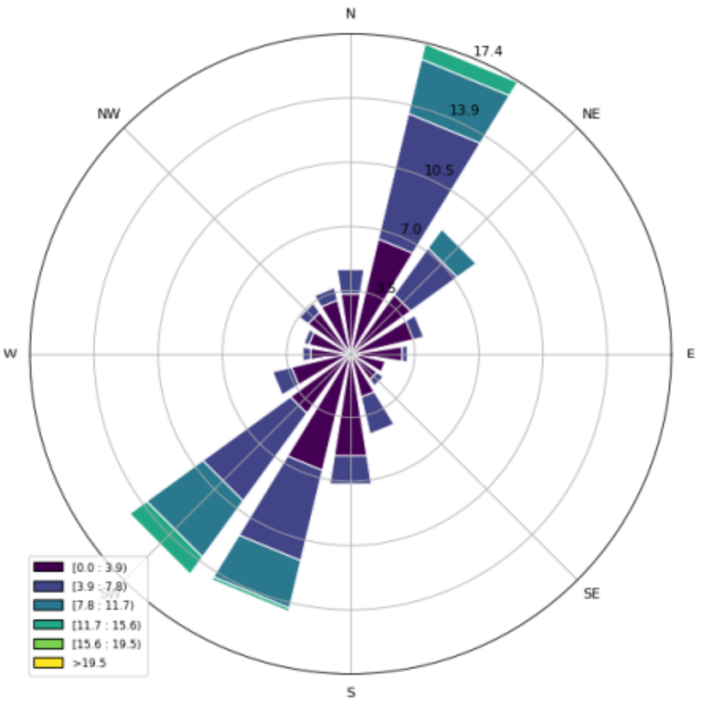

Figure 32: Wind rose from LiDAR.

Figure 33 shows the wind rose from turbine 9 for the period 10 February to 27 March. This turbine is the closest to the location of the new measurement mast. And is likely affected by the same wind conditions when the wind comes from it most dominant direction.

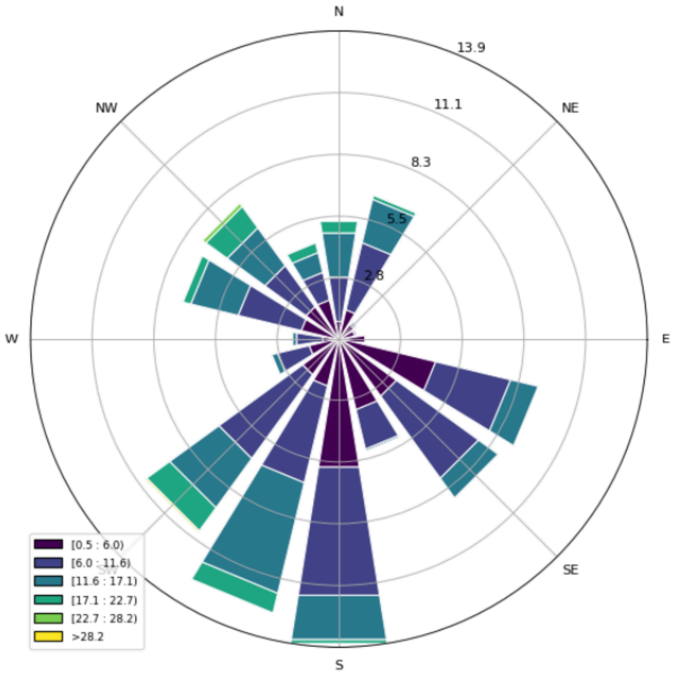

Figure 33: Wind rose from turbine 9 from 10. Feb to 27. Mar 2023

Since the wind roses are not from the same place, its not expected that the wind roses are completely similar but to have some similarities. The comparison is only to get an idea of how LiDAR performs, even though it’s not accurate. Both wind roses exhibit similarities; they both indicate a predominant wind direction from the south. However, there are notable differences between them. The wind rose from the turbine displays higher wind speeds, while the wind rose from the LiDAR shows a high occurrence of wind from the north.

The presence of numerous non-values in the LiDAR data poses a challenge when trying to obtain a comprehensive understanding of wind patterns. The data obtained from the LiDAR contained a lot of non-values, where these non-values likely result from the LiDARs inability to detect the wind at that range, it could be due to a clear day with few particles in the air or potential obstructions interfering with its measurement. The absence of continuous data points throughout the period this work focused on hampers the accuracy of the wind assessment, making it difficult to capture fluctuations and variations in wind speed and direction.

In contrast, a measurement mast installed at the site offers consistent and reliable measurements by continuously collecting data. This reliability enables more precise evaluation of wind conditions. While LiDAR can provide some initial indication of wind conditions and assist in preliminary assessments, it falls short in terms of delivering reliable and continuous wind data, its limitations and high costs make it less viable option for long term monitoring and analysis.

To improve the reliability and effectiveness of LiDAR measurements, further research is necessary, this entails a deeper understanding of the LiDAR technology, learning from knowledge gained, identifying and addressing potential sources of interference or blockage, and enhancing data processing techniques.

LiDAR can be used as a supplementary tool for initial evaluations and site suitability assessments, but relying only on its measurement can lead to uncertainties and inaccuracies.

5 Conclusion

This study examined wind conditions in a specific area and evaluated the accuracy of two different models in estimating the wind conditions and energy production at Fakken 1. It aimed to determine the most reliable model simulation. Further it investigated the potential energy production of the wind parks new expansion and possible enhancement of the proposed turbine positions.

Initially, the WRF Fakken 1 simulation showed the closest approximation of energy production, with only a deviation of 9% on average. However, when considering the production losses throughout the year and reducing the models estimates by 5%, the WAsP Fakken 1, using data from 2017, appeared to provide the best estimate of production.

The WRF model's resolution was found to be insufficient in accurately estimating the actual observations, and likely causing the model to underestimate the wind speed. With a resolution of 1 km, it was found that the model missed some of the key terrain features that influence the wind conditions over the area. With improved resolution, the WRF models could potentially yield better estimates by capturing these terrain features that influence the wind conditions.

Compared to the WRF model the WAsP model was better at capturing the variations in production trends at the turbines. The WRF model estimated a more even production at the turbines, but the observed production showed more variations in production. The WAsP model demonstrated a better sensitivity to production differences among turbines and aligned more closely with the variations shown in the observed data.

Regarding the new expansion Fakken 2, the WAsP model projected it would have a production of approximately 173 GWh, while the WRF model estimated a production of approximately 155 GWh. It was found that the expansion would have a small effect on Fakken 1, the production on Fakken 1 will experience a small decrease in production.

The study found that the proposed turbine placement yielded high energy production but could be improved. The new turbine positions yielded an increase in production of 7 GWh yearly, the same amount as adding a new turbine to Fakken 1.

The WAsP model offers several tools and features, including the WAsP Climate Analyst and the resource grid feature, which enhance its suitability for wind resource assessment and siting. In contrast, the WRF models lengthy computational time and the requirement to rerun the model after any alterations in turbine positions make it impractical for siting purposes. Moreover, the WAsP model outperforms the WRF model in terms of computational speed, delivering results within minutes instead of several hours.

The LiDAR gave good results, but not good enough to replace measurement mast. The idea of the LiDAR being a good first step at evaluating the conditions, gives some indication, but due to the missing data, not good enough. LiDAR can be used in the preliminary steps as a supplementary tool for the initial assessments but relying only on its measurement can lead to uncertainties and inaccuracies.

Overall, the study concluded that the WAsP model outperformed the WRF model in wind resource assessment and siting due to its accuracy, efficiency, and ability to capture variations in production within a wind park.

5.1 Future work

Based on the conclusions of this study, the suggestion for future research is as follows. With the aim of obtaining more accuracy in the WRF model, running with higher resolution is the next step. With higher resolution the aim is to capture more of the terrain and its effect on the wind flow, and therefore obtaining more accurate values. Furthermore, for obtaining a better result from the WAsP model, and as a way of making wind resource assessment easier, the WAsP model can use WRF output as input. It has been shown to give good preliminary results (Carvalho et al., 2013).

Another suggestion is using the results from the LiDAR data as input in the WAsP model. However, before this can be done the LiDAR measurement needs to be improved. The reliability and effectiveness of the LiDAR data needs improvement, and further research and a deeper understanding if the LiDAR technology is necessary, as well as identifying and addressing potential sources of interference or blockage. In addition, for using the LiDAR data in WAsP a longer time series of wind data is advantageous.

Furthermore, to get a more comprehensive view of the models and its performance in wind resource assessment the same evaluation should be done over several years, to validate their performance.

References

A.J. Bowen, N. G. M. (1996). *Exploring the limits of WAsP the wind atlas analysis and application program* 1996 European Wind Energy Conference and Exhibition, Gøtebord, Sweden.

Ahrens, C. D., & Henson, R. (2019). *Meteorology today: an introduction to weather, climate, and the environment*. Cengage.

Andrews, J., & Jelley, N. (2017). Wind power. In *Energy Science* (Third edition ed., pp. 237-270). Oxford University Press.

Asdrubali, F., Baldinelli, G., D'Alessandro, F., & Scrucca, F. (2015). Life cycle assessment of electricity production from renewable energies: Review and results harmonization. *Renewable and Sustainable Energy Reviews*, *42*, 1113-1122.

Awan, N. K., Truhetz, H., & Gobiet, A. (2011). Parameterization-induced error characteristics of MM5 and WRF operated in climate mode over the Alpine region: an ensemble-based analysis. *Journal of Climate*, *24*(12), 3107-3123.

Barthelmie, R. J., & Jensen, L. E. (2010). Evaluation of wind farm efficiency and wind turbine wakes at the Nysted offshore wind farm. *Wind Energy*, *13*(6), 573-586. https://doi.org/10.1002/we.408

Bechmann, A. (2017). *Data requirements for WAsP, CDF & WRF* (DTU Wind Energy), Issue. D. W. Energy.

Bilal, M. (2016). Wind Energy at Nygårdsfjellet–Norway. Wind field characterization and modelling.

Bilal, M., Solbakken, K., & Birkelund, Y. (2016). Wind speed and direction predictions by WRF and WindSim coupling over Nygårdsfjell. *Journal of Physics: Conference Series*, *753*(8), 082018. https://doi.org/10.1088/1742-6596/753/8/082018

Byrkjedal, Ø., & Åkervik, E. (2009). Vindkart for norge. *NVE Oppdragsrapport A*, *9*, 1-38.

Capacity Factor of Wind Turbine: What Influences Electricity Generation & What You Should Know About It. (n.d.). Retrieved 04.04.23 from https://www.luvside.de/en/capacity-factor-wind-turbine/

Carvalho, D., Rocha, A., & Gómez-Gesteira, M. (2012). Ocean surface wind simulation forced by different reanalyses: Comparison with observed data along the Iberian Peninsula coast. *Ocean Modelling*, *56*, 31-42.

Carvalho, D., Rocha, A., Gómez-Gesteira, M., & Santos, C. (2012). A sensitivity study of the WRF model in wind simulation for an area of high wind energy. *Environmental Modelling & Software*, *33*, 23-34.

Carvalho, D., Rocha, A., Gómez-Gesteira, M., & Santos, C. S. (2014). WRF wind simulation and wind energy production estimates forced by different reanalyses: Comparison with observed data for Portugal. *Applied Energy*, *117*, 116-126.

Carvalho, D., Rocha, A., Santos, C. S., & Pereira, R. (2013). Wind resource modelling in complex terrain using different mesoscale–microscale coupling techniques. *Applied Energy*, *108*, 493-504.

Chavan, D. S., Saahil, V., Singh, A., Himanshu, Parashar, D., Gaikwad, S., Sankpal, J., & Karandikar, P. B. (2017, 20-21 April 2017). Application of wind rose for wind turbine installation. 2017 International Conference on Circuit ,Power and Computing Technologies (ICCPCT),

Chen, F., Kusaka, H., Bornstein, R., Ching, J., Grimmond, C. S. B., Grossman-Clarke, S., Loridan, T., Manning, K. W., Martilli, A., Miao, S., Sailor, D., Salamanca, F. P., Taha, H., Tewari, M., Wang, X., Wyszogrodzki, A. A., & Zhang, C. (2011). The integrated WRF/urban modelling system: development, evaluation, and applications to urban environmental problems. *International Journal of Climatology*, *31*(2), 273-288. https://doi.org/10.1002/joc.2158

Draxl, C., Hahmann, A. N., Peña, A., & Giebel, G. (2014). Evaluating winds and vertical wind shear from Weather Research and Forecasting model forecasts using seven planetary boundary layer schemes. *Wind Energy*, *17*(1), 39-55.

El-Samra, R., Bou-Zeid, E., & El-Fadel, M. (2018). What model resolution is required in climatological downscaling over complex terrain? *Atmospheric Research*, *203*, 68-82.

Fakken vindkraftverk. (20.05.23). Troms Kraft. https://www.tromskraft.no/produksjon/kraftverk/fakken-vindkraftverk

Fernández-González, S., Martín, M. L., García-Ortega, E., Merino, A., Lorenzana, J., Sánchez, J. L., Valero, F., & Rodrigo, J. S. (2018). Sensitivity analysis of the WRF model: Wind-resource assessment for complex terrain. *Journal of Applied Meteorology and Climatology*, *57*(3), 733-753.

Fitch, A. C., Olson, J. B., Lundquist, J. K., Dudhia, J., Gupta, A. K., Michalakes, J., & Barstad, I. (2012). Local and mesoscale impacts of wind farms as parameterized in a mesoscale NWP model. *Monthly Weather Review*, *140*(9), 3017-3038.

Gasch, R., & Twele, J. (2012). *Wind power plants: Fundamentals, design, construction and operation, second edition*. https://doi.org/10.1007/978-3-642-22938-1

Giannaros, T. M., Melas, D., & Ziomas, I. (2017). Performance evaluation of the Weather Research and Forecasting (WRF) model for assessing wind resource in Greece. *Renewable Energy*, *102*, 190-198.

Global Wind Atlas. (2019). Retrieved 13.04-23 from https://globalwindatlas.info/en/about/introduction

González-Longatt, F., Wall, P., & Terzija, V. (2012). Wake effect in wind farm performance: Steady-state and dynamic behavior. *Renewable Energy*, *39*(1), 329-338. https://doi.org/10.1016/j.renene.2011.08.053

Guezuraga, B., Zauner, R., & Pölz, W. (2012). Life cycle assessment of two different 2 MW class wind turbines. *Renewable Energy*, *37*(1), 37-44.

Heatfield, D. N., C.A. Tenwolde, N.G. Mortensen and H.E. Jørgensen (2007). *WAsP Climate Analyst 3 Help Facility* (WAsP Climate Analyst 1 Help Facility, Issue.

Heathfield, D. N., Nielsen, M., Mortensen, N. G., & Rathmann, O. (2014). Wind Atlas Analysis and Application Program: WAsP 11 Help Facility.

Hersbach, H., Bell, B., Berrisford, P., Hirahara, S., Horányi, A., Muñoz-Sabater, J., Nicolas, J., Peubey, C., Radu, R., Schepers, D., Simmons, A., Soci, C., Abdalla, S., Abellan, X., Balsamo, G., Bechtold, P., Biavati, G., Bidlot, J., Bonavita, M., . . . Thépaut, J.-N. (2020). The ERA5 global reanalysis. *Quarterly Journal of the Royal Meteorological Society*, *146*(730), 1999-2049. https://doi.org/10.1002/qj.3803

Hochart, C., Fortin, G., Perron, J., & Ilinca, A. (2008). Wind turbine performance under icing conditions. *Wind Energy*, *11*(4), 319-333. https://doi.org/10.1002/we.258

Huleihil, M., & Mazor, G. (2012). Wind turbine power: The Betz limit and beyond. In *Advances in wind power*. IntechOpen.

Jackson, P. L., Mayr, G., & Vosper, S. (2013). Dynamically-driven winds. *Mountain weather research and forecasting: Recent progress and current challenges*, 121-218.

Jackson, P. L., & Steyn, D. G. (1994). Gap winds in a fjord. Part I: Observations and numerical simulation. *Monthly Weather Review*, *122*(12), 2645-2665.

Janjić, Z. I. (1994). The Step-Mountain Eta Coordinate Model: Further Developments of the Convection, Viscous Sublayer, and Turbulence Closure Schemes. *Monthly Weather Review*, *122*(5), 927–945. https://doi.org/10.1175/1520-0493(1994)122<0927:TSMECM>2.0.CO;2

Jeffreys, H. (1926). On the dynamics of geostrophic winds. *Quart. J. Roy. Meteor. Soc*, *52*(217), 85-104.

Jiménez, P. A., & Dudhia, J. (2013). On the ability of the WRF model to reproduce the surface wind direction over complex terrain. *Journal of Applied Meteorology and Climatology*, *52*(7), 1610-1617.

Jiménez, P. A., Dudhia, J., González-Rouco, J. F., Navarro, J., Montávez, J. P., & García-Bustamante, E. (2012). A Revised Scheme for the WRF Surface Layer Formulation. *Monthly Weather Review*, *140*(3), 898–918. https://doi.org/10.1175/MWR-D-11-00056.1

Khair, U., Fahmi, H., Al Hakim, S., & Rahim, R. (2017). Forecasting error calculation with mean absolute deviation and mean absolute percentage error. Journal of Physics: Conference Series,

Letcher, T. M. (2017). *Wind Energy Engineering. A handbook for onshore and offshore wind turbines*. Academic Press. https://doi.org/10.1016/B978-0-12-809451-8.00033-3

Markowski, P., & Richardson, Y. (2011). *Mesoscale meteorology in midlatitudes*. John Wiley & Sons.

Markowski, P., Richardson, Y. (2010). Blocking of the Wind by Terrain. In *Mesoscale Meteorology in Midlatitudes* (pp. 343-366). https://doi.org/10.1002/9780470682104.ch13

Methodology. (2019). Retrieved 13.04.23 from https://globalwindatlas.info/en/about/method

Mlawer, E. J., Taubman, S. J., Brown, P. D., Iacono, M. J., & Clough, S. A. (1997). Radiative transfer for inhomogeneous atmospheres: RRTM, a validated correlated-k model for the longwave. *Journal of Geophysical Research: Atmospheres*, *102*(D14), 16663-16682. https://doi.org/10.1029/97JD00237

Mortensen, N. G., Heathfield, D. N., Rathmann, O. S., & Nielsen, M. (2021). Wind Atlas Analysis and Application Program: WAsP 12 Help Facility.

Mortensen, N. G., & Petersen, E. L. (1997). Influence of topographical input data on the accuracy of wind flow modelling in complex terrain. EWEC-CONFERENCE-,

Mortensen, N. G. B., A.J. ; Antoniou, I. (2006). *Improving WAsP predictions in (too) complex terrain* 2006 European Wind Energy Conference and Exhibition, Athens, Greece.

Nakanishi, M., & Niino, H. (2009). Development of an Improved Turbulence Closure Model for the Atmospheric Boundary Layer. *Journal of the Meteorological Society of Japan. Ser. II*, *87*(5), 895-912. https://doi.org/10.2151/jmsj.87.895

Olson, J. B. K., Jaymes S.;Angevine, Wayne. A.;Brown, John M.;Pagowski, Mariusz;Sušelj, Kay;. (2019). A Description of the MYNN-EDMF Scheme and the Coupling to Other Components in WRF–ARW. https://doi.org/10.25923/n9wm-be49

Pereira, R., Guedes, R., & Silva Santos, C. (2010). Comparing WAsP and CFD wind resource estimates for the "regular" user.

Persson, A. (1998). How Do We Understand the Coriolis Force? [Research Article]. *Bulletin of the American Meteorological Society*, *79*(7), 1373-1386. https://doi.org/10.1175/1520-0477(1998)079<1373:HDWUTC>2.0.CO;2

Ramos, D. A., Guedes, V. G., Pereira, R. R., Valentim, T. A., & Netto, W. A. (2017). Further considerations on WAsP, OpenWind and WindSim comparison study: Atmospheric flow modelling over complex terrain and energy production estimate. Proceedings of the Windpower 2017 Conference and Exhibition, Rio De Janeiro, Brazil,

Ritchie, H., Roser, M., & Rosado, P. (2020). CO_2 and greenhouse gas emissions. *Our world in data*.

Samuelsen, E. M. (2007). *Et dynamisk studium av stormen Narve-et kaldluftsutbrudd i Finnmark-ved hjelp av observasjoner og numeriske simuleringer* [The University of Bergen].

Schneemann, J., Trabucchi, D., Trujillo, J. J., & Kühn, M. (2014). Comparing measurements of the horizontal wind speed of a 2D Multi-Lidar and a cup anemometer. Journal of Physics: Conference Series,

Scorer, R. (1952). Mountain ‐ gap winds; a study of surface wind at Gibraltar. *Quarterly Journal of the Royal Meteorological Society*, *78*(335), 53-61.

Solbakken, K., & Birkelund, Y. (2018). Evaluation of the Weather Research and Forecasting (WRF) model with respect to wind in complex terrain. *Journal of Physics: Conference Series*, *1102*(1), 012011. https://doi.org/10.1088/1742-6596/1102/1/012011

Solbakken, K., Birkelund, Y., & Samuelsen, E. M. (2021). Evaluation of surface wind using WRF in complex terrain: Atmospheric input data and grid spacing. *Environmental Modelling & Software*, *145*, 105182. https://doi.org/https://doi.org/10.1016/j.envsoft.2021.105182

SSB. (2023). *Elektrisitet*. SSB. Retrieved 19.05.23 from https://www.ssb.no/energi-og-industri/energi/statistikk/elektrisitet

Statkraft. (16.05.23). *Wind power*. Statkraft. Retrieved 16.05.23 from https://www.statkraft.com/what-we-do/wind-power/

Statnett. (2022). *Økende forbruk gir kraftunderskudd fra 2027*. Statnett. Retrieved 16.05.23 from https://www.statnett.no/om-statnett/nyheter-og-pressemeldinger/nyhetsarkiv-2022/kortsiktig-markedsanalyse-okende-forbruk-gir-kraftunderskudd-fra-2027/

Svendsen, H., & Skjoldal, H. R. (1995). Physical oceanography of coupled fjord-coast systems in northern Norway with special focus on frontal dynamics and tides. In *Ecology of Fjords and Coastal Waters* (pp. 149-164). Elsevier Publishing Company.

Tewari, M., Chen, F., Wang, W., Dudhia, J., Lemone, M. A., Mitchell, K. E., Ek, M., Gayno, G., Wegiel, J. W., & Cuenca, R. (2004). Implementation and verification of the unified Noah land-surface model in the WRF model *20th Conference on Weather Analysis and Forecasting/16th Conference on Numerical Weather Prediction*. http://n2t.net/ark:/85065/d7fb523p

Thompson, G., Field, P. R., Rasmussen, R. M., & Hall, W. D. (2008). Explicit Forecasts of Winter Precipitation Using an Improved Bulk Microphysics Scheme. Part II: Implementation of a New Snow Parameterization. *Monthly Weather Review*, *136*(12), 5095–5115. https://doi.org/10.1175/2008MWR2387.1

Tiedtke, M. (1989). A Comprehensive Mass Flux Scheme for Cumulus Parameterization in Large-Scale Models. *Montly Weather Review*, *117*(8), 1779–1800. https://doi.org/10.1175/1520-0493(1989)117<1779:ACMFSF>2.0.CO;2

Users Guide v4.3, Chapter 3. (25.04.23). Mesoscale & Microscale Meteorology Labratory. https://www2.mmm.ucar.edu/wrf/users/docs/user_guide_v4/v4.3/users_guide_chap3.html

Users Guide v4.3, Chapter 5. (20.04.23). Mesoscale & Microscale Meteorology Labratory. Retrieved 20.04.23 from https://www2.mmm.ucar.edu/wrf/users/docs/user_guide_v4/v4.3/users_guide_chap5.html

Valkonen, T., Stoll, P., Batrak, Y., Køltzow, M., Schneider, T. M., Stigter, E. E., Aashamar, O. B., Støylen, E., & Jonassen, M. O. (2020). Evaluation of a sub-kilometre NWP system in an Arctic fjord-valley system in winter. *Tellus A: Dynamic Meteorology and Oceanography*, *72*(1), 1-21.

Varma, S. A. K., Srimurali, M., & Varma, S. V. K. (2013). Evolution of wind Rose diagrams for RTPP, Kadapa, AP, India. *International Journal of Innovative Research and Development*, *2*(13), 2278.

Vestas. (26.05.23). *V90-3.0 MW An efficient way to more power*. Retrieved 26.05.23 from https://www.nhsec.nh.gov/projects/2008-04/documents/app_appendix_7.pdf

Wallace, J. M., & Hobbs, P. V. (2006a). 3 - Atmospheric Thermodynamics. In J. M. Wallace & P. V. Hobbs (Eds.), *Atmospheric Science (Second Edition)* (pp. 63-111). Academic Press. https://doi.org/https://doi.org/10.1016/B978-0-12-732951-2.50008-9

Wallace, J. M., & Hobbs, P. V. (2006b). 7 - Atmospheric Dynamics. In J. M. Wallace & P. V. Hobbs (Eds.), *Atmospheric Science (Second Edition)* (pp. 271-311). Academic Press. https://doi.org/https://doi.org/10.1016/B978-0-12-732951-2.50012-0

Wind Resource Mapping - WAsP. (28.04.23). Retrieved 28.04.23 from https://www.wasp.dk/wasp/wind-resource-mapping

Zhang, C., Wang, Y., & Hamilton, K. (2011). Improved Representation of Boundary Layer Clouds over the Southeast Pacific in ARW-WRF Using a Modified Tiedtke Cumulus Parameterization Scheme. *Montly Weather Review*, *139*(11), 3489–3513. https://doi.org/10.1175/MWR-D-10-05091.1

Appendix A

New turbine positions for Fakken 2, coordinates given in UTM zone 34.

Turbine	North	East
A	7777194	462657.8
B	7777549	462958.8
C	7777495	463574.1
D	7777923	463654.2
E	7777368	462042.2
F	7777943	462497.0
G	7778204	464082.3
H	7777807	461852.2
I	7778351	462169.3
J	7778586	462524.0
K	7778251	462858.4

Appendix B

A WAsP project report for Fakken 1 and Fakken 2 with data from 2017.

'Fakken 1&2' WAsP project report

Produced on 26.04.2023 at 17:21:00 by licenced user: Martine Bjugg using WAsP Version: 12.07.0068

Report Contents

1. Project Parameters

WAsP project parameters

All of the WAsP project parameters have default values.

2. Generalised wind climate 'Fakken'

back to top

Reference conditions

Number of roughness lengths	5
Number of heights	5
Number of sectors	12
Roughness lengths	0,000 m; 0,030 m; 0,100 m; 0,400 m; 1,500 m
Heights a.g.l	10 m; 25 m; 50 m; 100 m; 200 m

Climate context

The generalised wind climate is located at 70,10°N 20,09°E

The Met. station is located at co-ordinates (465527,7777205) in a map called 'Elevation & Roughness Fakken'.

Barometric reference information

Mean temperature	2,89 °
Ref. altitude for temperature a.s.l	156,3 m
Mean pressure	98 930 Pa
Ref. altitude for pressure a.s.l	154,3 m
Relative humidity	78,16628 %

GWC profile model for 'Fakken'

Using geostrophic wind shear model, with:

- Magnitude of geostrophic shear vector (dG/dz): 0,01
- Direction of geostrophic shear vector (beta): 176,01

Using the classic WAsP profile model, with:

- Rms heat flux over land: 100,00 (the default)
- Rms heat flux over water: 30,00 (the default)
- Offset heat flux over land (classic): -40,00 (the default)

- Offset heat flux over water (classic): -8,00 (the default)
- Factor in height of boundary layer over land: 1,00 (the default)
- Factor in height of boundary layer over water: 1,00 (the default)
- Power law in decay of the stability induced perturbation of wind profile: 1,50 (the default)

Generalised wind climate summary

		Roughness length 0,000 m	Roughness length 0,030 m	Roughness length 0,100 m	Roughness length 0,400 m	Roughness length 1,500 m
Height 10,0 m	Weibull A [m/s]	6,59	4,92	4,38	3,52	2,41
	Weibull k	1,35	1,23	1,22	1,20	1,13
	Mean speed U [m/s]	6,05	4,60	4,09	3,32	2,30
Height 25,0 m	Weibull A [m/s]	7,22	5,87	5,38	4,62	3,64
	Weibull k	1,37	1,28	1,26	1,23	1,16
	Mean speed U [m/s]	6,60	5,44	5,00	4,32	3,45
Height 50,0 m	Weibull A [m/s]	7,76	6,74	6,26	5,55	4,64
	Weibull k	1,40	1,35	1,32	1,27	1,19
	Mean speed U [m/s]	7,07	6,18	5,76	5,15	4,38
Height 100,0 m	Weibull A [m/s]	8,37	7,83	7,32	6,61	5,76
	Weibull k	1,43	1,43	1,38	1,31	1,22
	Mean speed U [m/s]	7,60	7,11	6,69	6,10	5,40
Height 200,0 m	Weibull A [m/s]	9,07	9,26	8,68	7,92	7,09
	Weibull k	1,44	1,51	1,45	1,37	1,26
	Mean speed U [m/s]	8,24	8,36	7,87	7,25	6,58

Detailed descriptions

Roughness length 0,000 m

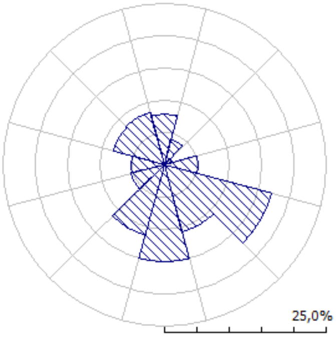

		Sec. 1 0°	Sec. 2 30°	Sec. 3 60°	Sec. 4 90°	Sec. 5 120°	Sec. 6 150°	Sec. 7 180°	Sec. 8 210°	Sec. 9 240°	Sec. 10 270°	Sec. 11 300°	Sec. 12 330°
Height 10,0 m	A [m/s]	3,9	4,5	3,7	8,2	9,4	5,2	5,5	6,1	8,9	9,4	7,9	5,1
	k	1,37	1,41	1,09	1,49	1,81	1,60	1,69	1,77	1,34	1,40	1,49	1,38
	U [m/s]	3,60	4,11	3,61	7,43	8,39	4,63	4,91	5,39	8,21	8,56	7,15	4,69

Height 25,0 m	A [m/s] k U [m/s]	4,4 1,44 3,97	5,0 1,46 4,50	4,1 1,11 3,94	9,0 1,51 8,08	10,3 1,83 9,13	5,6 1,63 5,05	6,0 1,74 5,38	6,7 1,85 5,94	9,7 1,35 8,93	10,2 1,41 9,30	8,6 1,51 7,79	5,7 1,44 5,15
Height 50,0 m	A [m/s] k U [m/s]	4,8 1,47 4,32	5,4 1,51 4,85	4,4 1,14 4,21	9,6 1,53 8,61	10,9 1,86 9,72	6,0 1,66 5,39	6,5 1,81 5,77	7,3 1,98 6,45	10,4 1,36 9,49	10,9 1,43 9,88	9,2 1,54 8,30	6,1 1,47 5,56
Height 100,0 m	A [m/s] k U [m/s]	5,2 1,41 4,76	5,8 1,46 5,27	4,7 1,15 4,52	10,2 1,59 9,18	11,7 1,91 10,35	6,5 1,74 5,77	7,0 1,90 6,25	8,0 1,97 7,09	11,0 1,38 10,08	11,6 1,44 10,50	9,9 1,54 8,87	6,7 1,43 6,06
Height 200,0 m	A [m/s] k U [m/s]	5,8 1,35 5,34	6,4 1,41 5,80	5,1 1,12 4,89	10,9 1,57 9,83	12,5 1,95 11,07	7,0 1,74 6,21	7,7 1,84 6,84	8,9 1,89 7,91	11,7 1,36 10,73	12,3 1,42 11,17	10,5 1,50 9,52	7,3 1,37 6,70
Freq. [%]		7,8	4,1	1,4	5,2	17,2	10,7	14,9	11,4	5,5	5,1	8,3	8,5

Roughness length 0,030 m

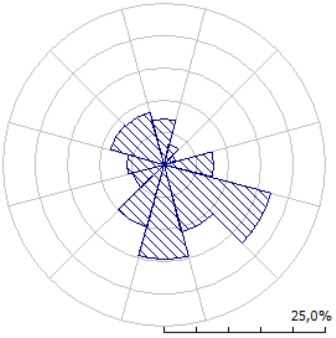

		Sec. 1 0°	Sec. 2 30°	Sec. 3 60°	Sec. 4 90°	Sec. 5 120°	Sec. 6 150°	Sec. 7 180°	Sec. 8 210°	Sec. 9 240°	Sec. 10 270°	Sec. 11 300°	Sec. 12 330°
Height 10,0 m	A [m/s] k U [m/s]	2,7 1,31 2,50	3,4 1,34 3,11	4,0 1,17 3,83	7,8 1,58 7,03	7,9 1,63 7,03	3,8 1,57 3,45	3,9 1,43 3,50	4,2 1,31 3,90	6,5 1,35 5,95	6,0 1,33 5,51	4,9 1,37 4,51	3,1 1,28 2,85
Height 25,0 m	A [m/s] k U [m/s]	3,4 1,51 3,07	4,1 1,45 3,72	4,8 1,21 4,49	9,1 1,61 8,19	9,2 1,66 8,19	4,5 1,62 4,05	4,7 1,54 4,19	5,2 1,44 4,71	7,6 1,38 6,95	7,1 1,37 6,45	5,9 1,44 5,33	3,9 1,49 3,53
Height 50,0 m	A [m/s] k U [m/s]	4,1 1,59 3,66	4,8 1,59 4,29	5,5 1,28 5,06	10,2 1,65 9,12	10,2 1,70 9,12	5,1 1,70 4,57	5,4 1,73 4,85	6,2 1,67 5,51	8,5 1,42 7,76	8,0 1,43 7,23	6,7 1,56 6,06	4,7 1,58 4,25
Height 100,0 m	A [m/s] k U [m/s]	5,0 1,52 4,55	5,6 1,54 5,06	6,3 1,35 5,74	11,4 1,72 10,14	11,4 1,77 10,15	5,8 1,87 5,18	6,5 1,99 5,76	7,5 1,72 6,64	9,6 1,49 8,69	9,0 1,47 8,13	7,7 1,53 6,98	5,9 1,50 5,34

Height 200,0 m	A [m/s] k U [m/s]	6,5 1,44 5,87	6,8 1,47 6,16	7,2 1,31 6,61	12,8 1,85 11,34	12,8 1,90 11,34	6,8 2,03 5,98	8,0 1,90 7,06	9,3 1,65 8,30	10,8 1,46 9,81	10,2 1,43 9,25	9,1 1,47 8,22	7,7 1,43 6,96
Freq. [%]		7,1	3,3	1,9	7,7	17,1	10,8	14,5	9,9	4,9	5,7	8,7	8,4

Roughness length 0,100 m

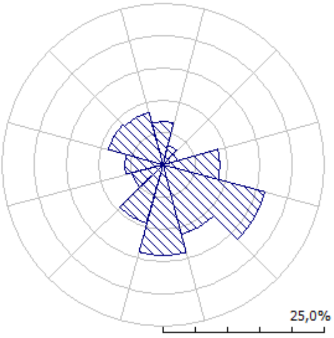

		Sec. 1 0°	Sec. 2 30°	Sec. 3 60°	Sec. 4 90°	Sec. 5 120°	Sec. 6 150°	Sec. 7 180°	Sec. 8 210°	Sec. 9 240°	Sec. 10 270°	Sec. 11 300°	Sec. 12 330°
Height 10,0 m	A [m/s] k U [m/s]	2,4 1,34 2,18	3,0 1,36 2,74	4,1 1,27 3,80	7,6 1,70 6,81	7,0 1,62 6,31	3,4 1,54 3,10	3,3 1,45 3,04	3,7 1,28 3,43	5,5 1,35 5,02	5,0 1,35 4,57	4,0 1,35 3,70	2,6 1,29 2,38
Height 25,0 m	A [m/s] k U [m/s]	3,1 1,53 2,75	3,7 1,46 3,37	5,0 1,30 4,61	9,2 1,72 8,20	8,5 1,64 7,60	4,2 1,58 3,76	4,2 1,56 3,76	4,6 1,38 4,25	6,6 1,38 6,07	6,1 1,38 5,54	5,0 1,42 4,53	3,4 1,50 3,03
Height 50,0 m	A [m/s] k U [m/s]	3,7 1,58 3,33	4,4 1,57 3,94	5,8 1,36 5,27	10,4 1,75 9,29	9,6 1,67 8,61	4,8 1,65 4,31	5,0 1,74 4,43	5,5 1,54 4,99	7,6 1,43 6,91	7,0 1,45 6,34	5,8 1,53 5,25	4,1 1,54 3,71
Height 100,0 m	A [m/s] k U [m/s]	4,6 1,50 4,14	5,2 1,52 4,67	6,6 1,43 6,02	11,8 1,81 10,45	10,9 1,72 9,69	5,6 1,79 4,95	6,0 1,93 5,31	6,7 1,58 5,97	8,7 1,48 7,85	8,0 1,47 7,24	6,8 1,49 6,14	5,2 1,46 4,70
Height 200,0 m	A [m/s] k U [m/s]	5,9 1,42 5,33	6,3 1,46 5,66	7,6 1,39 6,93	13,2 1,91 11,73	12,3 1,82 10,89	6,5 1,93 5,75	7,4 1,85 6,55	8,1 1,51 7,34	9,9 1,45 8,96	9,2 1,42 8,34	8,0 1,43 7,31	6,8 1,38 6,18
Freq. [%]		6,7	3,1	2,3	8,9	16,3	11,2	14,0	9,3	5,0	6,0	8,7	8,4

Roughness length 0,400 m

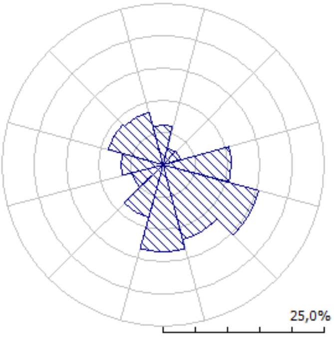

		Sec. 1 0°	Sec. 2 30°	Sec. 3 60°	Sec. 4 90°	Sec. 5 120°	Sec. 6 150°	Sec. 7 180°	Sec. 8 210°	Sec. 9 240°	Sec. 10 270°	Sec. 11 300°	Sec. 12 330°
Height 10,0 m	A [m/s] k U [m/s]	1,9 1,39 1,73	2,4 1,39 2,19	3,8 1,37 3,44	7,0 1,87 6,26	5,5 1,55 4,96	2,7 1,55 2,47	2,6 1,51 2,37	2,9 1,24 2,71	4,1 1,37 3,77	3,7 1,36 3,36	2,9 1,33 2,67	1,9 1,31 1,75
Height 25,0 m	A [m/s] k U [m/s]	2,6 1,57 2,32	3,2 1,47 2,87	4,9 1,40 4,45	9,1 1,88 8,06	7,1 1,57 6,39	3,6 1,59 3,21	3,5 1,62 3,14	3,9 1,31 3,56	5,4 1,40 4,89	4,8 1,40 4,37	3,8 1,40 3,51	2,7 1,53 2,39
Height 50,0 m	A [m/s] k U [m/s]	3,2 1,56 2,88	3,8 1,55 3,46	5,8 1,44 5,25	10,6 1,90 9,45	8,4 1,59 7,50	4,3 1,66 3,82	4,3 1,81 3,84	4,7 1,42 4,28	6,4 1,44 5,77	5,7 1,47 5,18	4,7 1,47 4,22	3,3 1,48 3,03
Height 100,0 m	A [m/s] k U [m/s]	4,0 1,49 3,63	4,6 1,50 4,16	6,8 1,51 6,12	12,3 1,94 10,88	9,7 1,62 8,65	5,0 1,79 4,49	5,3 1,89 4,71	5,7 1,43 5,16	7,4 1,47 6,74	6,7 1,46 6,10	5,6 1,43 5,06	4,3 1,40 3,92
Height 200,0 m	A [m/s] k U [m/s]	5,1 1,40 4,69	5,6 1,44 5,06	7,9 1,47 7,12	14,0 2,01 12,40	11,1 1,69 9,89	6,0 1,87 5,30	6,6 1,80 5,91	6,9 1,37 6,29	8,6 1,44 7,84	7,9 1,41 7,19	6,7 1,37 6,16	5,7 1,31 5,23
Freq. [%]		6,1	2,7	2,9	10,6	15,3	11,8	13,4	8,5	5,0	6,4	8,8	8,4

Roughness length 1,500 m

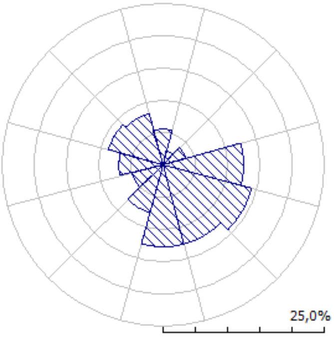

		Sec. 1 0°	Sec. 2 30°	Sec. 3 60°	Sec. 4 90°	Sec. 5 120°	Sec. 6 150°	Sec. 7 180°	Sec. 8 210°	Sec. 9 240°	Sec. 10 270°	Sec. 11 300°	Sec. 12 330°
Height 10,0 m	A [m/s] k U [m/s]	1,3 1,47 1,17	1,6 1,41 1,47	2,9 1,49 2,64	5,7 2,06 5,07	3,4 1,43 3,08	1,8 1,57 1,61	1,7 1,60 1,56	1,9 1,24 1,82	2,6 1,38 2,39	2,3 1,38 2,08	1,8 1,32 1,62	1,2 1,36 1,08
Height 25,0 m	A [m/s] k U [m/s]	2,0 1,60 1,80	2,5 1,48 2,23	4,4 1,51 3,94	8,5 2,07 7,52	5,0 1,44 4,58	2,7 1,62 2,42	2,7 1,74 2,39	3,0 1,30 2,74	3,9 1,41 3,57	3,4 1,43 3,13	2,7 1,41 2,45	1,9 1,46 1,71
Height 50,0 m	A [m/s] k U [m/s]	2,6 1,54 2,37	3,1 1,51 2,84	5,5 1,54 4,95	10,6 2,08 9,40	6,3 1,45 5,73	3,4 1,69 3,06	3,5 1,92 3,12	3,8 1,38 3,49	5,0 1,46 4,50	4,4 1,48 3,97	3,5 1,41 3,15	2,5 1,38 2,32
Height 100,0 m	A [m/s] k U [m/s]	3,4 1,45 3,09	3,9 1,46 3,54	6,7 1,59 6,00	12,8 2,11 11,30	7,6 1,48 6,91	4,2 1,83 3,77	4,5 1,84 4,01	4,7 1,34 4,34	6,1 1,45 5,49	5,4 1,44 4,90	4,3 1,36 3,98	3,4 1,29 3,14
Height 200,0 m	A [m/s] k U [m/s]	4,4 1,35 4,06	4,8 1,39 4,40	8,0 1,56 7,15	15,0 2,15 13,26	9,0 1,53 8,13	5,2 1,80 4,60	5,8 1,74 5,19	5,8 1,29 5,36	7,3 1,41 6,61	6,6 1,39 5,98	5,4 1,29 5,01	4,6 1,20 4,31
Freq. [%]		5,5	2,3	3,6	12,5	14,1	12,6	12,6	7,6	5,0	6,9	8,8	8,3

3. Resource grids

back to top

3.1 Resource grid: 'Resource grid Fakken 1'

Grid Setup

Column count	60
Row count	44
Calculation sites	2640

Resolution	50 m
Boundary extent	(462819, 7775864) to (465819, 7778064)
Nodes extent	(462844, 7775889) to (465794, 7778039)
Height a.g.l.	80m

Results

Mean Speed [m/s]

Maximum Value	8,54 m/s at (463744, 7777039)
Minimum Value	5,88 m/s at (464694, 7777889)
Mean Value	7,12 m/s

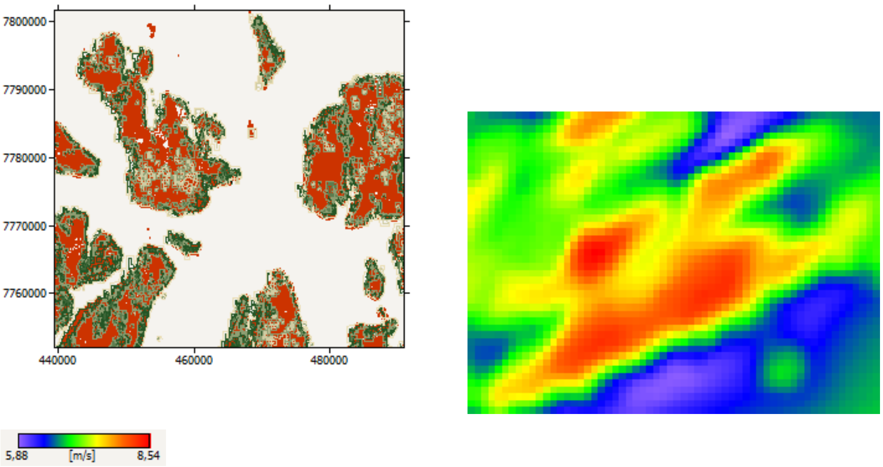

Power Density [W/m²]

Maximum Value	1038 W/m² at (463744, 7777039)
Minimum Value	346 W/m² at (464694, 7777889)
Mean Value	621 W/m²

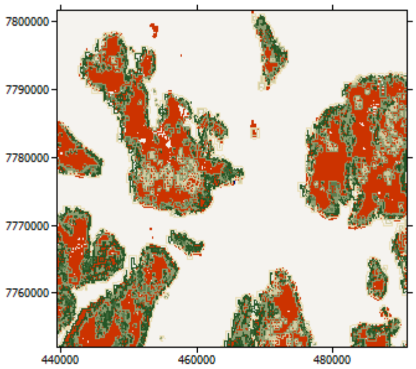

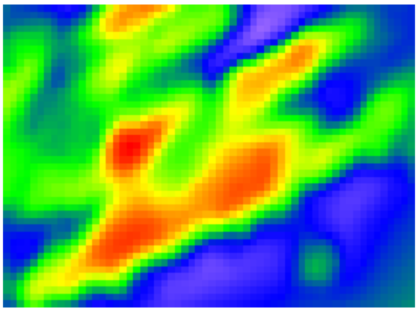

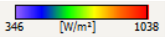

AEP [GWh]

Maximum Value	9,924 GWh at (463744, 7777039)
Minimum Value	5,622 GWh at (464694, 7777889)
Mean Value	7,806 GWh

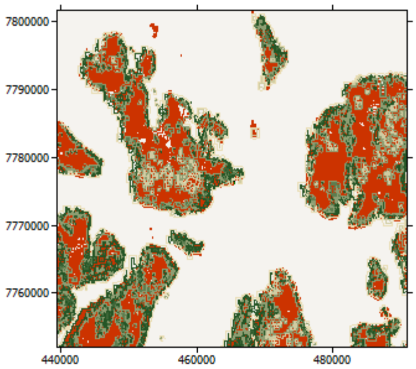

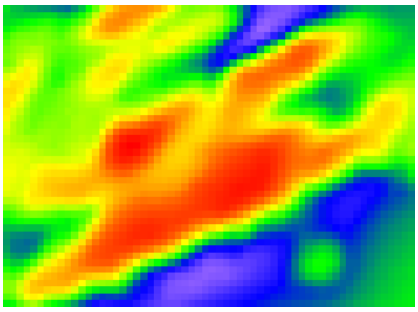

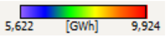

RIX [%]

Maximum Value	8,8% at (462894, 7776389)
Minimum Value	0,3% at (465794, 7778039)
Mean Value	4,1%

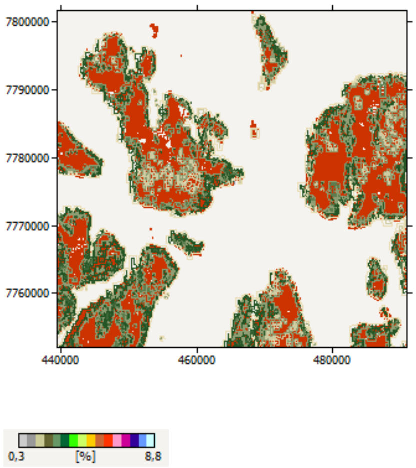

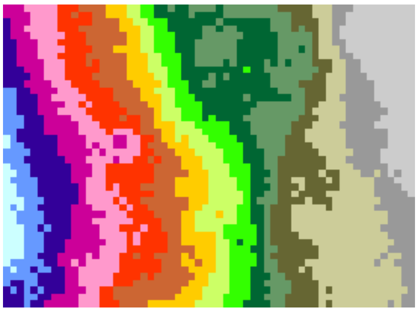

3.2 Resource grid: 'Resource grid Fakken 2'

back to '3. Resource grids'

Grid Setup

Column count	53
Row count	40
Calculation sites	2120
Resolution	50 m
Boundary extent	(461570, 7777120) to (464220, 7779120)
Nodes extent	(461595, 7777145) to (464195, 7779095)
Height a.g.l.	112m

Results

Mean Speed [m/s]

Maximum Value	8,46 m/s at (463845, 7777145)
Minimum Value	6,63 m/s at (462445, 7779095)
Mean Value	7,50 m/s

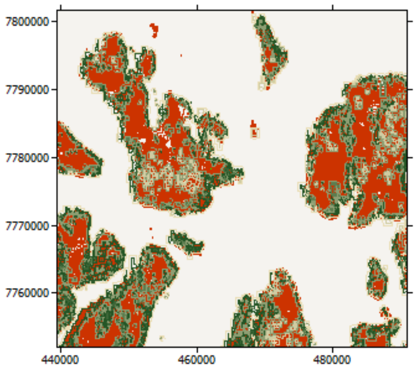

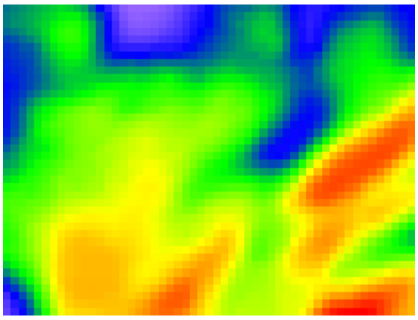

Power Density [W/m²]

Maximum Value	981 W/m² at (463845, 7777145)
Minimum Value	495 W/m² at (461595, 7777145)
Mean Value	712 W/m²

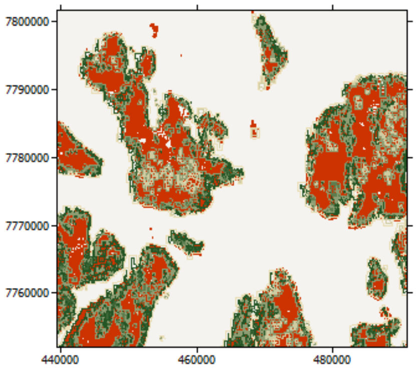

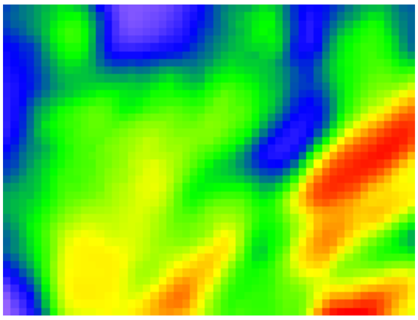

AEP [GWh]

Maximum Value	19,868 GWh at (463895, 7777145)
Minimum Value	13,935 GWh at (462495, 7779095)
Mean Value	16,841 GWh

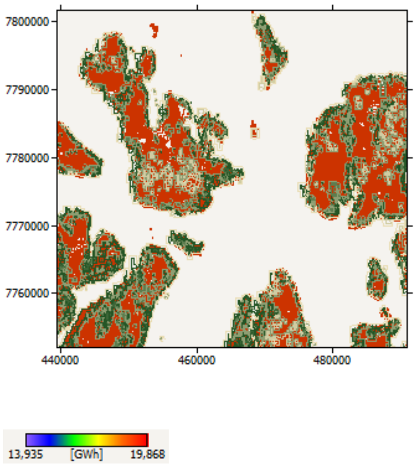

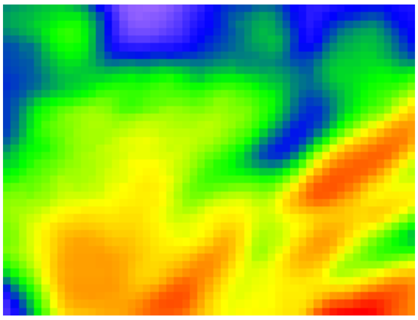

RIX [%]

Maximum Value	15,0% at (461595, 7777395)
Minimum Value	1,5% at (464195, 7779095)
Mean Value	7,3%

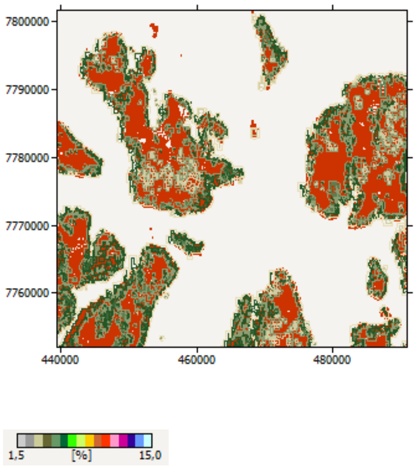

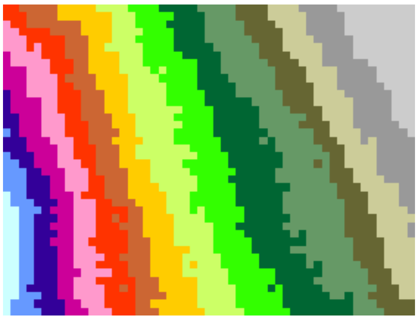

4. Wind farms

back to top

4.1 Wind farm: 'Fakken 1'

Site information

Site count	18

Uniform hub height a.g.l	80 m

The Wind farm lies in a map called 'Elevation & Roughness Fakken'.

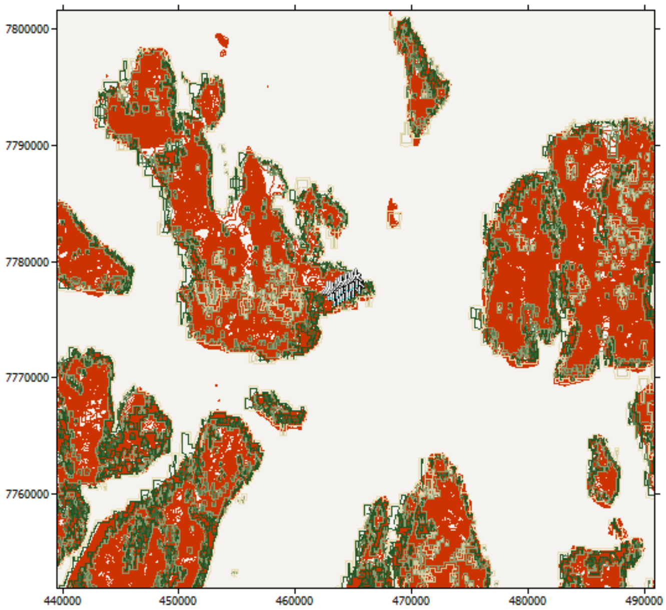

Summary results

Parameter	Total	Average	Minimum	Maximum
Net AEP [GWh]	147,822	8,212	7,190	8,974
Gross AEP [GWh]	159,293	8,850	7,605	9,853
Wake loss [%]	7,20	-	-	-

Site results

Site	Location [m]	Turbine	Elevation [m] a.s.l.	Height [m] a.g.l.	Air density [kg/m³]	Net AEP [GWh]	Wake loss [%]
Turbine 1	(463525,4, 7776391,0)	V90-3.0 MW VCS 50 Hz	162,2	80,0	1,235	8,547	4,29
Turbine 2	(463774,7, 7776491,0)	V90-3.0 MW VCS 50 Hz	180,0	80,0	1,232	8,894	5,33
Turbine 3	(464032,7, 7776627,0)	V90-3.0 MW VCS 50 Hz	166,8	80,0	1,234	8,596	5,61
Turbine 4	(464286,7, 7776777,0)	V90-3.0 MW VCS 50 Hz	168,1	80,0	1,234	8,740	5,62
Turbine 5	(464521,9, 7776926,0)	V90-3.0 MW VCS	167,0	80,0	1,234	8,793	6,72

		50 Hz					
Turbine 6	(464795,5, 7776972,0)	V90-3.0 MW VCS 50 Hz	150,0	80,0	1,236	8,974	5,78
Turbine 7	(465105,3, 7777044,0)	V90-3.0 MW VCS 50 Hz	96,8	80,0	1,243	8,300	4,74
Turbine 8	(465619,9, 7777416,0)	V90-3.0 MW VCS 50 Hz	52,5	80,0	1,248	7,770	4,01
Turbine 9	(462935,4, 7776849,0)	V90-3.0 MW VCS 50 Hz	166,7	80,0	1,234	7,626	6,05
Turbine 10	(463228,4, 7776925,0)	V90-3.0 MW VCS 50 Hz	163,0	80,0	1,234	7,249	10,42
Turbine 11	(463425,8, 7776724,0)	V90-3.0 MW VCS 50 Hz	171,5	80,0	1,233	7,638	11,13
Turbine 12	(463708,5, 7777012,0)	V90-3.0 MW VCS 50 Hz	217,8	80,0	1,227	8,919	9,47
Turbine 13	(463923,8, 7777187,0)	V90-3.0 MW VCS 50 Hz	188,6	80,0	1,231	8,364	10,32
Turbine 14	(464165,7, 7777354,0)	V90-3.0 MW VCS 50 Hz	150,0	80,0	1,236	7,616	10,63
Turbine 15	(464588,8, 7777533,0)	V90-3.0 MW VCS 50 Hz	130,7	80,0	1,238	8,171	9,12
Turbine 16	(464870,8, 7777590,0)	V90-3.0 MW VCS 50 Hz	106,1	80,0	1,242	8,371	7,58
Turbine 17	(465146,4, 7777714,0)	V90-3.0 MW VCS 50 Hz	72,1	80,0	1,246	8,064	7,14
Turbine 18	(465391, 7777941)	V90-3.0 MW VCS 50 Hz	28,8	80,0	1,251	7,190	5,46

Site wind climates

Site	Location [m]	H [m]	A [m/s]	k	U [m/s]	E [W/m²]	RIX [%]	dRIX [%]
Turbine 1	(463525,4, 7776391,0)	80,0	8,7	1,48	7,87	835	6,8	5,9
Turbine 2	(463774,7, 7776491,0)	80,0	9,0	1,49	8,17	921	6,0	5,1
Turbine 3	(464032,7, 7776627,0)	80,0	8,8	1,53	7,88	795	5,3	4,4
Turbine 4	(464286,7, 7776777,0)	80,0	8,8	1,54	7,96	813	4,7	3,8
Turbine 5	(464521,9, 7776926,0)	80,0	9,0	1,53	8,09	859	3,8	2,9
Turbine 6	(464795,5, 7776972,0)	80,0	9,0	1,53	8,14	879	2,6	1,7
Turbine 7	(465105,3, 7777044,0)	80,0	8,4	1,57	7,55	683	1,9	1,0
Turbine 8	(465619,9, 7777416,0)	80,0	8,0	1,52	7,24	629	0,8	-0,1
Turbine 9	(462935,4, 7776849,0)	80,0	8,1	1,53	7,27	629	8,1	7,2
Turbine 10	(463228,4, 7776925,0)	80,0	8,0	1,54	7,24	612	7,4	6,5
Turbine 11	(463425,8, 7776724,0)	80,0	8,4	1,54	7,55	695	6,8	5,9

Turbine 12	(463708,5, 7777012,0)	80,0	9,4	1,50	8,49	1025	6,7	5,8
Turbine 13	(463923,8, 7777187,0)	80,0	9,0	1,51	8,09	880	5,2	4,3
Turbine 14	(464165,7, 7777354,0)	80,0	8,4	1,51	7,54	713	3,9	3,0
Turbine 15	(464588,8, 7777533,0)	80,0	8,7	1,51	7,84	805	3,4	2,5
Turbine 16	(464870,8, 7777590,0)	80,0	8,7	1,49	7,90	841	2,9	2,0
Turbine 17	(465146,4, 7777714,0)	80,0	8,4	1,52	7,60	731	1,9	1,0
Turbine 18	(465391, 7777941)	80,0	7,7	1,47	7,00	601	0,7	-0,2

4.2 Wind farm: 'Fakken 2'

back to '4. Wind farms'

Site information

Site count	11
Uniform hub height a.g.l	112 m

The Wind farm lies in a map called 'Elevation & Roughness Fakken'.

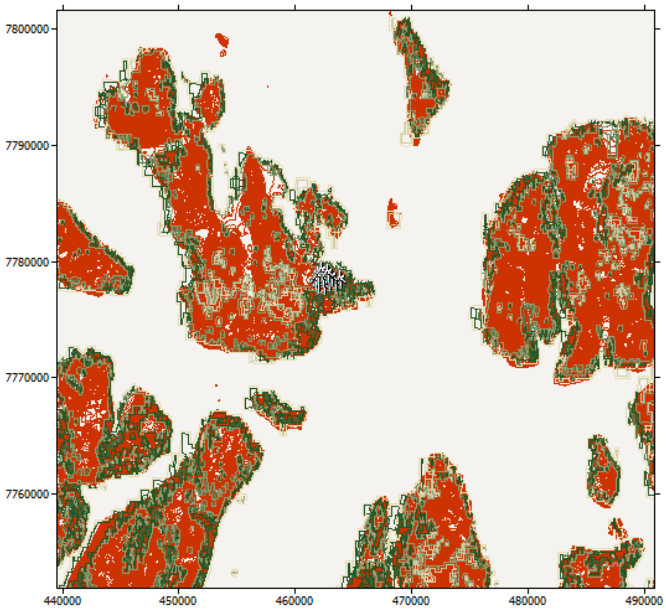

Summary results

Parameter	Total	Average	Minimum	Maximum
Net AEP [GWh]	173,877	15,807	13,829	17,890
Gross AEP [GWh]	191,799	17,436	15,695	18,859
Wake loss [%]	9,34	-	-	-

Site results

Site	Location [m]	Turbine	Elevation [m] a.s.l.	Height [m] a.g.l.	Air density [kg/m³]	Net AEP [GWh]	Wake loss [%]
Turbine A	(462683, 7777267)	Vestas V150 6MW	199,2	112,0	1,226	17,890	5,14
Turbine B	(463036,3, 7777574,0)	Vestas V150 6MW	170,2	112,0	1,229	16,669	7,58
Turbine C	(463580,9, 7777635,0)	Vestas V150 6MW	155,2	112,0	1,231	17,112	5,35
Turbine D	(463995,9, 7777865,0)	Vestas V150 6MW	121,2	112,0	1,236	16,892	4,06
Turbine E	(462142,6, 7777470,0)	Vestas V150 6MW	190,0	112,0	1,227	16,855	7,58
Turbine F	(462542,7, 7777914,0)	Vestas V150 6MW	163,1	112,0	1,230	15,344	12,75
Turbine G	(463279,7, 7778088,0)	Vestas V150 6MW	93,6	112,0	1,239	13,829	11,89
Turbine H	(461852,2, 7777807,0)	Vestas V150 6MW	168,3	112,0	1,230	15,839	8,18
Turbine I	(462110,4, 7778170,0)	Vestas V150 6MW	150,9	112,0	1,232	14,709	13,62
Turbine J	(462452,4, 7778625,0)	Vestas V150 6MW	102,9	112,0	1,238	14,001	14,20
Turbine K	(462920,6, 7778391,0)	Vestas V150 6MW	113,4	112,0	1,237	14,736	13,84

Site wind climates

Site	Location [m]	H [m]	A [m/s]	k	U [m/s]	E [W/m²]	RIX [%]	dRIX [%]
Turbine A	(462683, 7777267)	112,0	9,0	1,53	8,11	868	8,8	7,9
Turbine B	(463036,3, 7777574,0)	112,0	8,7	1,52	7,84	788	7,2	6,2
Turbine C	(463580,9, 7777635,0)	112,0	8,8	1,49	7,91	834	5,5	4,6
Turbine D	(463995,9, 7777865,0)	112,0	8,6	1,48	7,78	810	3,6	2,7
Turbine E	(462142,6, 7777470,0)	112,0	8,8	1,53	7,89	794	11,0	10,1
Turbine F	(462542,7, 7777914,0)	112,0	8,6	1,50	7,74	776	8,4	7,5
Turbine G	(463279,7, 7778088,0)	112,0	7,9	1,52	7,11	594	5,9	5,0
Turbine H	(461852,2, 7777807,0)	112,0	8,4	1,54	7,57	700	12,8	11,9
Turbine I	(462110,4, 7778170,0)	112,0	8,4	1,51	7,54	715	10,2	9,3
Turbine J	(462452,4, 7778625,0)	112,0	8,1	1,50	7,32	663	7,7	6,8
Turbine K	(462920,6, 7778391,0)	112,0	8,4	1,49	7,57	735	6,5	5,6

Appendix C

The namelist.wps from the WRF model

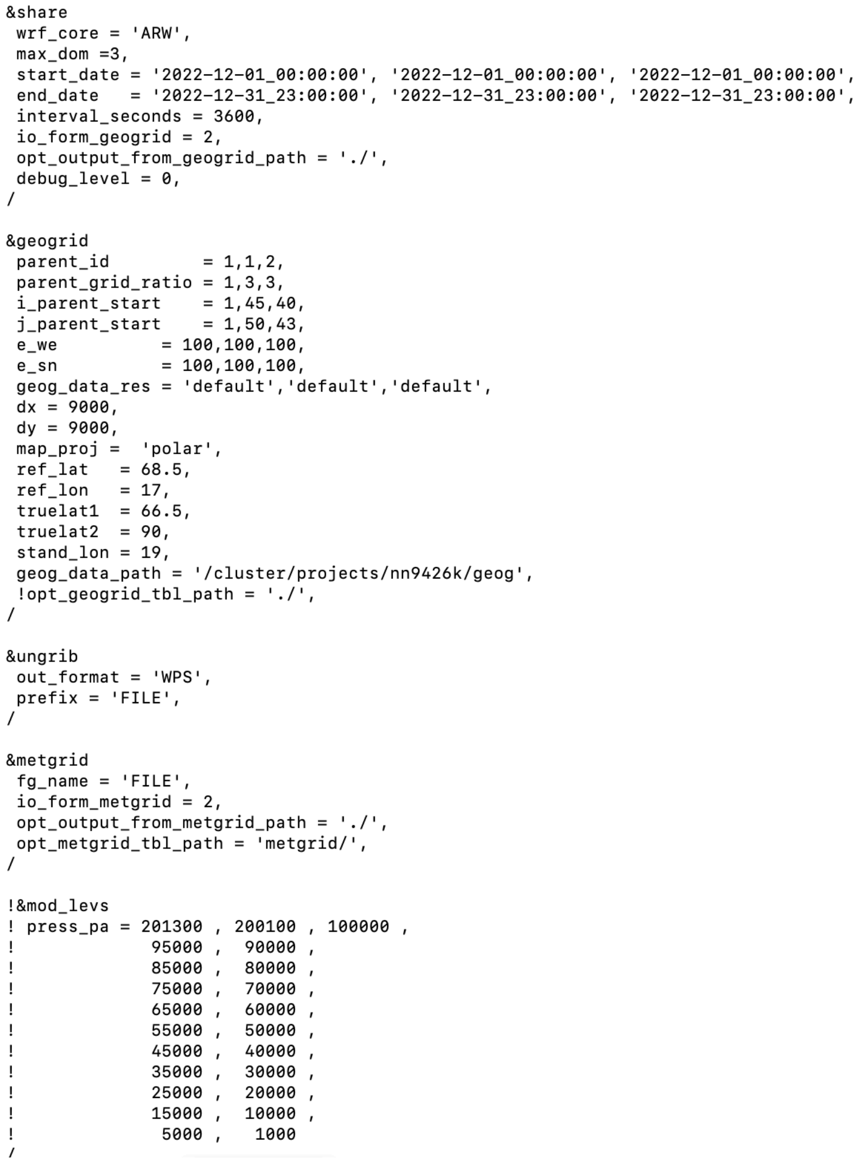

```
&share
 wrf_core = 'ARW',
 max_dom =3,
 start_date = '2022-12-01_00:00:00', '2022-12-01_00:00:00', '2022-12-01_00:00:00',
 end_date   = '2022-12-31_23:00:00', '2022-12-31_23:00:00', '2022-12-31_23:00:00',
 interval_seconds = 3600,
 io_form_geogrid = 2,
 opt_output_from_geogrid_path = './',
 debug_level = 0,
/

&geogrid
 parent_id         = 1,1,2,
 parent_grid_ratio = 1,3,3,
 i_parent_start    = 1,45,40,
 j_parent_start    = 1,50,43,
 e_we          = 100,100,100,
 e_sn          = 100,100,100,
 geog_data_res = 'default','default','default',
 dx = 9000,
 dy = 9000,
 map_proj =  'polar',
 ref_lat   = 68.5,
 ref_lon   = 17,
 truelat1  = 66.5,
 truelat2  = 90,
 stand_lon = 19,
 geog_data_path = '/cluster/projects/nn9426k/geog',
 !opt_geogrid_tbl_path = './',
/

&ungrib
 out_format = 'WPS',
 prefix = 'FILE',
/

&metgrid
 fg_name = 'FILE',
 io_form_metgrid = 2,
 opt_output_from_metgrid_path = './',
 opt_metgrid_tbl_path = 'metgrid/',
/

!&mod_levs
! press_pa = 201300 , 200100 , 100000 ,
!             95000 ,  90000 ,
!             85000 ,  80000 ,
!             75000 ,  70000 ,
!             65000 ,  60000 ,
!             55000 ,  50000 ,
!             45000 ,  40000 ,
!             35000 ,  30000 ,
!             25000 ,  20000 ,
!             15000 ,  10000 ,
!              5000 ,   1000
/
```

Appendix D

The namelist.input file from the WRF model.

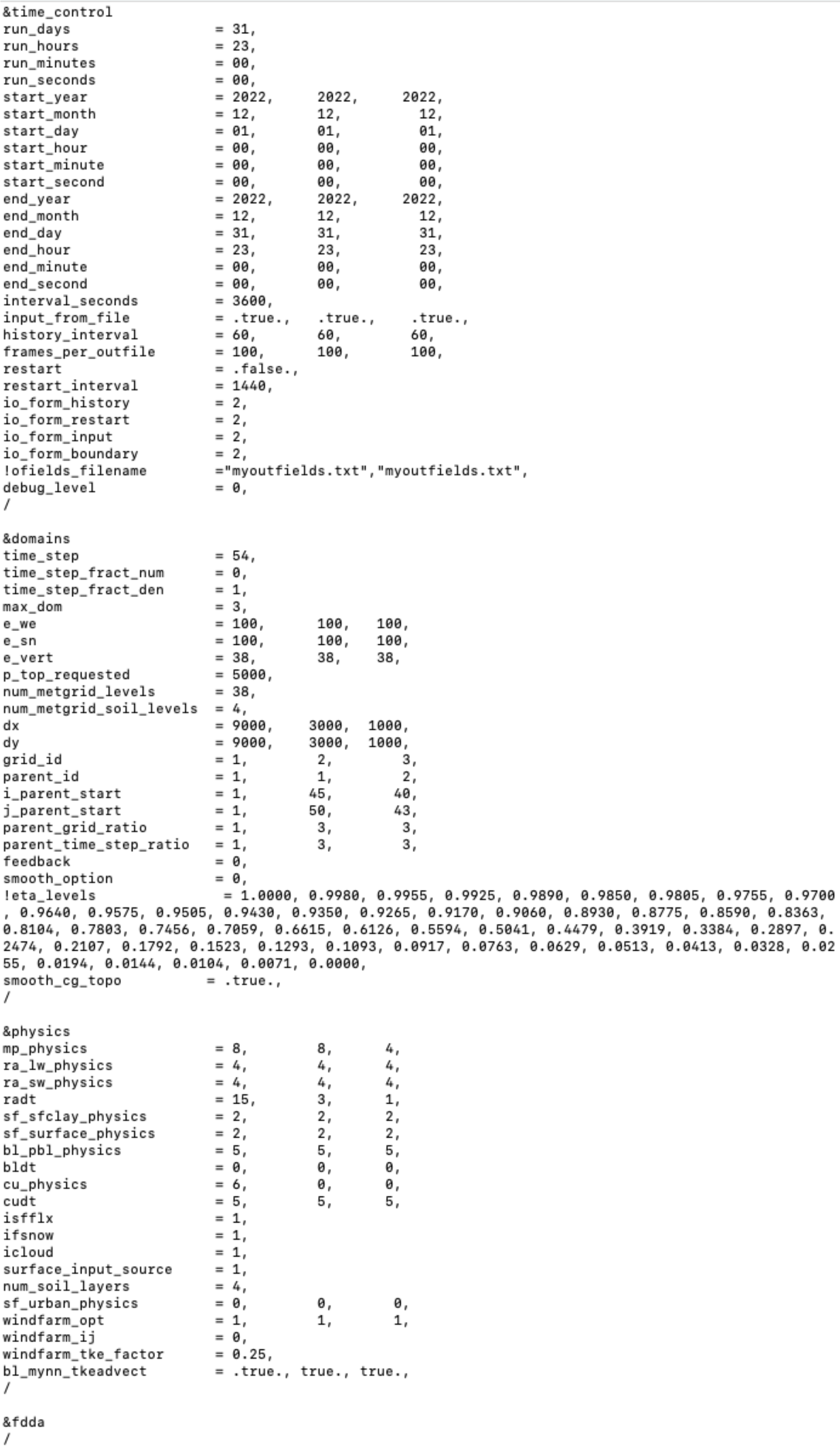

```
&time_control
run_days                 = 31,
run_hours                = 23,
run_minutes              = 00,
run_seconds              = 00,
start_year               = 2022,     2022,     2022,
start_month              = 12,       12,         12,
start_day                = 01,       01,         01,
start_hour               = 00,       00,         00,
start_minute             = 00,       00,         00,
start_second             = 00,       00,         00,
end_year                 = 2022,     2022,     2022,
end_month                = 12,       12,         12,
end_day                  = 31,       31,         31,
end_hour                 = 23,       23,         23,
end_minute               = 00,       00,         00,
end_second               = 00,       00,         00,
interval_seconds         = 3600,
input_from_file          = .true.,   .true.,    .true.,
history_interval         = 60,       60,        60,
frames_per_outfile       = 100,      100,       100,
restart                  = .false.,
restart_interval         = 1440,
io_form_history          = 2,
io_form_restart          = 2,
io_form_input            = 2,
io_form_boundary         = 2,
!ofields_filename        ="myoutfields.txt","myoutfields.txt",
debug_level              = 0,
/

&domains
time_step                = 54,
time_step_fract_num      = 0,
time_step_fract_den      = 1,
max_dom                  = 3,
e_we                     = 100,      100,   100,
e_sn                     = 100,      100,   100,
e_vert                   = 38,       38,    38,
p_top_requested          = 5000,
num_metgrid_levels       = 38,
num_metgrid_soil_levels  = 4,
dx                       = 9000,    3000,  1000,
dy                       = 9000,    3000,  1000,
grid_id                  = 1,        2,        3,
parent_id                = 1,        1,        2,
i_parent_start           = 1,       45,       40,
j_parent_start           = 1,       50,       43,
parent_grid_ratio        = 1,        3,        3,
parent_time_step_ratio   = 1,        3,        3,
feedback                 = 0,
smooth_option            = 0,
!eta_levels               = 1.0000, 0.9980, 0.9955, 0.9925, 0.9890, 0.9850, 0.9805, 0.9755, 0.9700
, 0.9640, 0.9575, 0.9505, 0.9430, 0.9350, 0.9265, 0.9170, 0.9060, 0.8930, 0.8775, 0.8590, 0.8363,
0.8104, 0.7803, 0.7456, 0.7059, 0.6615, 0.6126, 0.5594, 0.5041, 0.4479, 0.3919, 0.3384, 0.2897, 0.
2474, 0.2107, 0.1792, 0.1523, 0.1293, 0.1093, 0.0917, 0.0763, 0.0629, 0.0513, 0.0413, 0.0328, 0.02
55, 0.0194, 0.0144, 0.0104, 0.0071, 0.0000,
smooth_cg_topo          = .true.,
/

&physics
mp_physics               = 8,        8,       4,
ra_lw_physics            = 4,        4,       4,
ra_sw_physics            = 4,        4,       4,
radt                     = 15,       3,       1,
sf_sfclay_physics        = 2,        2,       2,
sf_surface_physics       = 2,        2,       2,
bl_pbl_physics           = 5,        5,       5,
bldt                     = 0,        0,       0,
cu_physics               = 6,        0,       0,
cudt                     = 5,        5,       5,
isfflx                   = 1,
ifsnow                   = 1,
icloud                   = 1,
surface_input_source     = 1,
num_soil_layers          = 4,
sf_urban_physics         = 0,        0,        0,
windfarm_opt             = 1,        1,        1,
windfarm_ij              = 0,
windfarm_tke_factor      = 0.25,
bl_mynn_tkeadvect        = .true., true., true.,
/

&fdda
/
```

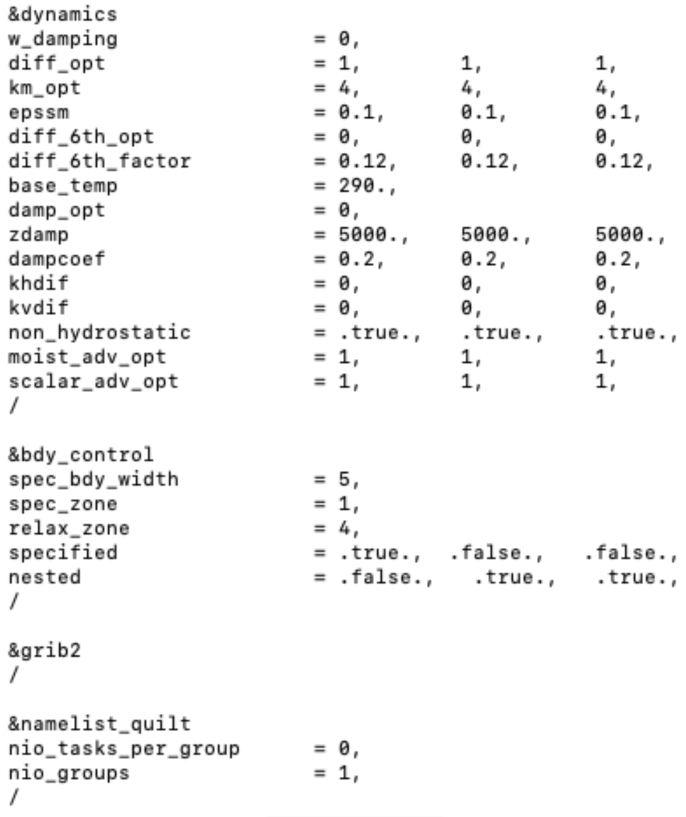

```
&dynamics
w_damping                = 0,
diff_opt                 = 1,         1,          1,
km_opt                   = 4,         4,          4,
epssm                    = 0.1,       0.1,        0.1,
diff_6th_opt             = 0,         0,          0,
diff_6th_factor          = 0.12,      0.12,       0.12,
base_temp                = 290.,
damp_opt                 = 0,
zdamp                    = 5000.,     5000.,      5000.,
dampcoef                 = 0.2,       0.2,        0.2,
khdif                    = 0,         0,          0,
kvdif                    = 0,         0,          0,
non_hydrostatic          = .true.,    .true.,     .true.,
moist_adv_opt            = 1,         1,          1,
scalar_adv_opt           = 1,         1,          1,
/

&bdy_control
spec_bdy_width           = 5,
spec_zone                = 1,
relax_zone               = 4,
specified                = .true.,  .false.,   .false.,
nested                   = .false.,   .true.,    .true.,
/

&grib2
/

&namelist_quilt
nio_tasks_per_group      = 0,
nio_groups               = 1,
/
```

Appendix E

The windturbines.txt file from the WRF model

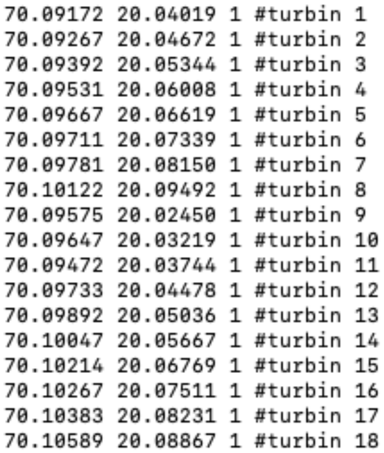

```
70.09172 20.04019 1 #turbin 1
70.09267 20.04672 1 #turbin 2
70.09392 20.05344 1 #turbin 3
70.09531 20.06008 1 #turbin 4
70.09667 20.06619 1 #turbin 5
70.09711 20.07339 1 #turbin 6
70.09781 20.08150 1 #turbin 7
70.10122 20.09492 1 #turbin 8
70.09575 20.02450 1 #turbin 9
70.09647 20.03219 1 #turbin 10
70.09472 20.03744 1 #turbin 11
70.09733 20.04478 1 #turbin 12
70.09892 20.05036 1 #turbin 13
70.10047 20.05667 1 #turbin 14
70.10214 20.06769 1 #turbin 15
70.10267 20.07511 1 #turbin 16
70.10383 20.08231 1 #turbin 17
70.10589 20.08867 1 #turbin 18
```

Appendix F

The wind-turbine-1.tbl file from the WRF model

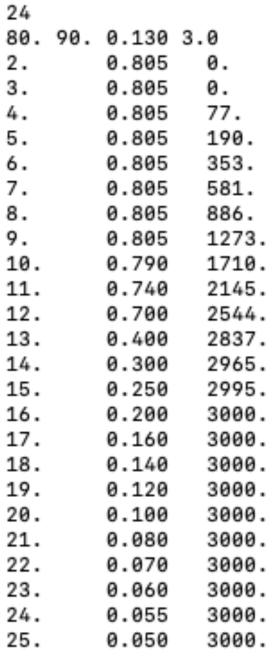

```
24
80. 90. 0.130 3.0
2.      0.805   0.
3.      0.805   0.
4.      0.805   77.
5.      0.805   190.
6.      0.805   353.
7.      0.805   581.
8.      0.805   886.
9.      0.805   1273.
10.     0.790   1710.
11.     0.740   2145.
12.     0.700   2544.
13.     0.400   2837.
14.     0.300   2965.
15.     0.250   2995.
16.     0.200   3000.
17.     0.160   3000.
18.     0.140   3000.
19.     0.120   3000.
20.     0.100   3000.
21.     0.080   3000.
22.     0.070   3000.
23.     0.060   3000.
24.     0.055   3000.
25.     0.050   3000.
```